

CSI 2264: Accretion process in classical T Tauri stars in the young cluster NGC 2264

A. P. Sousa¹, S. H. P. Alencar¹, J. Bouvier^{2,3}, J. Stauffer⁴, L. Venuti^{2,3}, L. Hillenbrand⁵, A.M. Cody⁶, P. S. Teixeira⁷, M. M. Guimarães⁸, P. T. McGinnis¹, L. Rebull⁴, E. Flaccomio⁹, G. Fürész¹⁰, G. Micela⁹, and J. F. Gameiro¹¹

¹ Departamento de Física-Icex-UFMG Antônio Carlos, 6627, 31270-90. Belo Horizonte, MG, Brazil
e-mail: a.lana@fisica.ufmg.br

² Univ. Grenoble Alpes, IPAG, F-38000 Grenoble, France

³ CNRS, IPAG, F-38000 Grenoble, France

⁴ Spitzer Science Center, California Institute of Technology, 1200 East California Boulevard, Pasadena, CA 91125, USA

⁵ Astronomy Department, California Institute of Technology, Pasadena, CA 91125, USA

⁶ NASA Ames Research Center, Kepler Science Office, Mountain View, CA 94035, USA

⁷ Universität Wien, Institut für Astrophysik, Türkenschanzstrasse 17, 1180 Vienna, Austria

⁸ Departamento de Física, Universidade Federal de Sergipe, Aracaju, SE, Brazil

⁹ INAF-Osservatorio Astronomico di Palermo, Piazza del Parlamento 1, I-90134 Palermo, Italy

¹⁰ MIT Kavli Institute for Astrophysics and Space Research, 77 Mass Ave 37-582f, Cambridge, MA 02139, USA

¹¹ Instituto de Astrofísica e Ciências Espaciais and Faculdade de Ciências Universidade do Porto, CAUP, Rua da Estrelas, PT4150-762 Porto, Portugal

Received May 26, 2015; accepted September 04, 2015

ABSTRACT

Context. NGC 2264 is a young stellar cluster (~ 3 Myr) with hundreds of low-mass accreting stars that allow a detailed analysis of the accretion process taking place in the pre-main sequence.

Aims. Our goal is to relate the photometric and spectroscopic variability of classical T Tauri stars to the physical processes acting in the stellar and circumstellar environment, within a few stellar radii from the star.

Methods. NGC 2264 was the target of a multiwavelength observational campaign with CoRoT, MOST, *Spitzer*, and Chandra satellites and photometric and spectroscopic observations from the ground. We classified the CoRoT light curves of accreting systems according to their morphology and compared our classification to several accretion diagnostics and disk parameters.

Results. The morphology of the CoRoT light curve reflects the evolution of the accretion process and of the inner disk region. Accretion burst stars present high mass-accretion rates and optically thick inner disks. AA Tau-like systems, whose light curves are dominated by circumstellar dust obscuration, show intermediate mass-accretion rates and are located in the transition of thick to anemic disks. Classical T Tauri stars with spot-like light curves correspond mostly to systems with a low mass-accretion rate and low mid-IR excess. About 30% of the classical T Tauri stars observed in the 2008 and 2011 CoRoT runs changed their light-curve morphology. Transitions from AA Tau-like and spot-like to aperiodic light curves and vice versa were common. The analysis of the H α emission line variability of 58 accreting stars showed that 8 presented a periodicity that in a few cases was coincident with the photometric period. The blue and red wings of the H α line profiles often do not correlate with each other, indicating that they are strongly influenced by different physical processes. Classical T Tauri stars have a dynamic stellar and circumstellar environment that can be explained by magnetospheric accretion and outflow models, including variations from stable to unstable accretion regimes on timescales of a few years.

Key words. Stars:Formation - Stars:Variables:T Tauri - Accretion:Accretion disks - Open cluster:Individual:NGC 2264

1. Introduction

Classical T Tauri stars (CTTSs) are young, low-mass stars ($M_* \leq 2 M_\odot$), with spectral types from F to M. They are surrounded by a circumstellar disk from which they are still accreting material. They present strong and broad emission lines in their spectra and show emission excess with respect to the stellar photosphere that goes from the radio to the ultraviolet (Bouvier et al. 2007b). CTTSs have strong magnetic fields (Johns-Krull et al. 1999; Johnstone et al. 2014) that disrupt the accretion disk at a few stellar radii from the star and channel the accreting material, forming accretion columns. The accreting gas hits the stellar surface and creates hot spots. CTTSs also present cold spots at the stellar surface; these are caused by magnetic activity (Bouvier

et al. 1995). Part of the gas in the inner disk region is ejected as a wind from the star-disk system along open magnetic field lines that may form collimated jets (e.g., Ferreira et al. 2006). In a few million years, before reaching the main sequence, CTTSs lose their disks and become weak-lined T Tauri stars (WTTs), which no longer show detectable signs of accretion (e.g., Meyer 2009).

A characteristic of CTTSs is the photometric and spectroscopic variability at various wavelengths. The photometric variability occurs from X-ray to infrared on a timescale from a few minutes to several years and is usually irregular (e.g., Appenzeller & Mundt 1989). Some stars, however, show periodic behavior, which may be due to the presence of stable cold and hot spots on the stellar surface or to circumstellar dust extinc-

tion, as observed in the classical T Tauri star AA Tau (Bouvier et al. 2007a; Alencar et al. 2010). The analysis of the photometric variability of CTTSs allows the determination of cold or hot spot characteristics and the typical timescale of the physical processes that cause each type of variability (dynamo, accretion, star-disk interaction). We can also estimate the line-of-sight dust distribution in the inner disk in favorable star-disk inclinations, when the inner disk occults the star as the system rotates. Spectroscopic variations are also present, and emission lines can vary in shape and intensity on a timescale of hours to days (e.g., Johns & Basri 1995a; Muzerolle et al. 1998; Costigan et al. 2014). The study of the spectroscopic variability of CTTSs can be related to the predictions of magnetospheric accretion models and magnetohydrodynamical simulations, which may include the accretion and the wind components, as well as the star-disk interaction.

CTTS also show infrared excess emission that indicates the presence of a circumstellar disk (e.g., Teixeira et al. 2012). This emission can be used to estimate the amount of dust in the system and relate disk and accretion evolution. The more evolved the star-disk system, the smaller the amount of circumstellar material available, and consequently, the lower the emission excess in the infrared.

Magnetospheric accretion is the standard model to describe the accretion process in CTTS (Shu et al. 1994; Hartmann et al. 1994). Magnetohydrodynamic simulations predict that magnetospheric accretion can occur in stable and unstable regimes (Kurosawa et al. 2008; Kulkarni & Romanova 2008, 2009; Kurosawa & Romanova 2013). In the stable regime, accretion occurs through two main accretion funnels (one in each hemisphere), and periodic spectroscopic and photometric variations are expected (Kurosawa & Romanova 2013), since there is a global organization of the accretion geometry. In the unstable regime, several accretion streams are formed that appear at random locations, creating multiple hot spots on the surface of the star. This accretion regime can be maintained by the Rayleigh-Taylor instability, which acts at the magnetosphere-disk interface (Kurosawa & Romanova 2013) and causes stochastic photometric and spectroscopic variability. If the Rayleigh-Taylor instability is weak, both the unstable and stable accretion regimes may coexist. Accretion will then occur mainly through two accretion funnels, but random accretion funnels can also appear in the magnetosphere (Kulkarni & Romanova 2008). These predictions can be checked with photometric and spectroscopic observations of CTTSs that span different timescales, from days to years, as the ones discussed in this work.

We analyze young stars belonging to NGC 2264, a young stellar cluster ($\lesssim 3$ Myr) located at a distance of ~ 760 pc from the Sun (Sung et al. 1997). This cluster shows evidence of ongoing star formation, such as the presence of molecular outflows and Herbig-Haro objects. In the pioneering work of Herbig (1954), 84 pre-main sequence stars were found in NGC 2264 with $H\alpha$ emission and were classified as T Tauri stars. Since then, and because of its proximity and low extinction in our line of sight, NGC 2264 has been the subject of many observational campaigns, from the radio to X-rays (e.g., Rebull et al. 2002; Lamm et al. 2004; Dahm & Simon 2005; Dahm 2008; Teixeira et al. 2012). About 1000 pre-main sequence stars have already been confirmed as members of NGC 2264 (Sung et al. 2009).

NGC 2264 was observed with the Convection Rotation and planetary Transits (CoRoT) satellite during 23 consecutive days in 2008 (from March 7 to 30), and photometric data with high cadence and high signal-to-noise ratio were obtained for ~ 300 known cluster members. The analysis of these data yielded studies in different research areas such as astroseismology (Zwintz

et al. 2013), stellar rotation (Affer et al. 2013), binary systems (Gillen et al. 2014), and accretion (Alencar et al. 2010). In the latter, it was shown that the light curve exhibited by the classical T Tauri star AA Tau, which is due to obscuration of the photosphere by circumstellar material in the inner disk region, is common among the cluster members. This opens the possibility of studying the inner disk evolution with photometric variability at different wavelengths. It was also shown that the CoRoT light curve morphology is related to the inner disk evolution and consequently to the accretion process.

A second observational campaign of NGC 2264 was organized in 2011 (Cody et al. 2013), including optical, infrared (IR), and X-ray simultaneous observations of the accreting and non-accreting members of the cluster. We present this in the next section. Using this new data set, we discuss the observed photometric and spectroscopic variability and its relation to magnetospheric accretion model predictions. We classify the CoRoT light curves of accreting systems according to their morphology and compare this classification with accretion diagnostics such as $H\alpha$ and HeI 6678 Å emission from FLAMES at the Very Large Telescope (VLT), UV excess from MegaCam at the Canada-France-Hawaii Telescope (CFHT), and disk parameters such as IR excess. A set of non-accreting members of NGC 2264 is used as a control sample to define the role of accretion in the observed correlations. Results from previous observations of NGC 2264 with the CoRoT satellite in 2008 are compared with the 2011 campaign to analyze the dynamical nature of accretion and the inner disk evolution. We analyze the variability in light-curve morphology between the two CoRoT campaigns and relate it to the proposed stable and unstable accretion scenarios in the literature. Cody et al. (2014) presented a detailed description of the photometric data sets and morphological classification of the various types of CTTS light curves observed with CoRoT and Spitzer in the 2011 campaign.

The paper is organized as follows. In Sect. 2, we present the 2011 observational data of NGC 2264 and the reduction procedures. The CTTS sample selection criteria are presented in Sect. 3. In Sect. 4 we discuss the morphological classification of the CoRoT light curves, following the classification scheme proposed by Alencar et al. (2010). In Sect. 5 we compare the CoRoT light-curve classification to the CFHT photometric analysis undertaken by Venuti et al. (2014). In Sect. 6 we analyze the accretion rate obtained directly from the $H\alpha$ line flux. In Sect. 7 we morphologically classify the $H\alpha$ line, as proposed by Reipurth et al. (1996). In Sects. 8 and 9 we obtain the periodicities of the $H\alpha$ and HeI 6678 Å lines. We discuss the presence of unstable and stable accretion regimes in Sect. 10, and we analyze the correlation between the different $H\alpha$ line structures (emissions and absorptions) in Sect. 11. In Sect. 12 we discuss some interesting objects to be analyzed individually in a future work. Section 13 presents our conclusions.

2. Data and reduction

NGC 2264 was observed with the CoRoT satellite during 40 days, from December 2, 2011 to January 10, 2012, providing exquisite photometry for ~ 500 probable cluster members. Simultaneously with the 2011 CoRoT run, the cluster was observed with the *Spitzer* satellite at 3.6 and 4.5 μm for 30 days and for 3.5 days with the Chandra satellite. This campaign was called *Coordinated Synoptic Investigation of NGC 2264* (CSI 2264)¹,

¹ All of the CoRoT and *Spitzer* light curves can be viewed and downloaded from <http://irsa.ipac.caltech.edu/data/SPITZER/CSI2264/>

and details about the data acquisition and reduction can be found in Cody et al. (2014). We also obtained u - and r -band observations of the cluster with MegaCam/CFHT from February 14 to 28, 2012. They were combined with observations of a first MegaCam campaign in 2010 to yield photometry in the $ugri$ bands for a large sample of stars in the NGC 2264 region. A detailed description of the CFHT observations is given in Venuti et al. (2014).

As a complement to the CSI 2264 campaign, we obtained FLAMES spectra at VLT/ESO of 58 CTTSs and 34 WTTSs. These stars were selected based on the CoRoT light-curve classification of 2008 (Alencar et al. 2010), to include most of the AA Tau and spot-like systems. FLAMES is a high- and medium-resolution multi-object spectrograph, covering a field of view of 25' in diameter. We obtained 20 to 22 spectra of each target in two different fields, distributed in 20 days from December 2011 to February 2012, part of them simultaneously with the CoRoT observations. We used the HR15N setup for the FLAMES/GIRAFFE spectrograph, centered at 6650 Å and covering the $6470 \text{ \AA} < \lambda < 6790 \text{ \AA}$ spectral region with a resolution of $R = 17,000$. This spectral region includes $H\alpha$, and the HeI6678 Å spectral lines that are analyzed in detail in the next sections. The observed spectra were reduced using the GASGANO reduction package from ESO. We performed the standard procedure of bias subtraction, flat-field correction, wavelength calibration, and barycentric velocity correction for all spectra and later normalized their continuum. In Table 1, we summarize the observations of the CSI 2264 campaign that are discussed in the following sections.

NGC 2264 is located in front of an emission nebula that is seen spectroscopically as a series of emission lines, such as [NII], [SII], and $H\alpha$, superposed on the stellar spectra. The $H\alpha$ nebular contribution is very narrow and in general much smaller than the accretion contribution to the $H\alpha$ emission of most CTTSs, presenting a mean equivalent width of the $H\alpha$ nebular contribution of $10.1 \pm 0.5 \text{ \AA}$, averaged over all the sky fibers. However, in a few spectra, the nebular emission is completely blended with the emission from the star, making it impossible to identify whether a component is of nebular or accretion origin. This sometimes makes removing the nebular emission from the total spectrum challenging. In general, this is a difficult task when using fiber spectrographs, as is the case of FLAMES. The nebular contribution is quite variable across the sky, and the sky fiber closest to the stellar fiber does not always present the same nebular contribution as the stellar fiber. Another difficulty is that some targets are very weak and present a spectrum comparable in intensity to the sky contribution.

To remove the nebular contribution from the stellar spectra, we subtracted the sky spectrum of the nearest sky fiber from the stellar spectrum of each star (see Fig. 1). The subtraction of the nebular emission is sometimes faulty, and a residual nebular line often remains. Even when the sky subtraction leaves residuals in the stellar spectrum, the contamination from the nebula is normally distinguishable from the stellar emission because the sky emission is narrower and weaker than the emission of most CTTSs.

3. CTTS and WTTS samples

We selected the CTTSs in NGC 2264 from the known cluster members according to photometric and spectroscopic criteria. We measured the $H\alpha$ equivalent width ($EW_{H\alpha}$) and $H\alpha$ width at 10% of maximum intensity ($W10\%_{H\alpha}$) in the FLAMES spec-

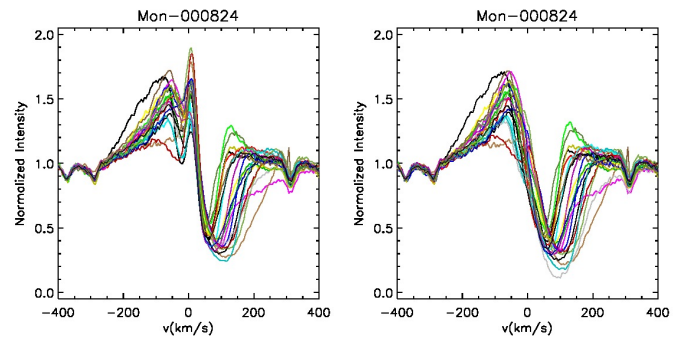


Fig. 1. $H\alpha$ emission lines of a CTTS before (left) and after (right) sky subtraction that show the removal of the nebular emission contribution. The nebular component is the very sharp, narrow emission seen near the line center in the left panel. Different colors correspond to different observing nights.

tra after removing the nebular contribution. We used published values of these parameters for the stars we did not observe spectroscopically, as shown in Table 2. To test the influence of the nebular emission on the measured values of $EW_{H\alpha}$, we calculated the $H\alpha$ equivalent width before and after subtracting the nebular part, from which we obtained a mean difference of about 10%. This difference does not affect our CTTS classification.

According to White & Basri (2003), CTTS have an $EW_{H\alpha}$ higher than a threshold that depends on the stellar spectral type. A young star is considered a CTTS if it presents an $EW_{H\alpha}$ higher than 3 Å for K0-K5, 10 Å for K7-M2.5, 20 Å for M3-M5.5, and 40 Å for M6-M7.5. Stars that show $W10\%_{H\alpha}$ higher than 270 km/s are also considered CTTSs, following White & Basri (2003). Fang et al. (2009) proposed more stringent limits to separate WTTSs from CTTSs that extend to late-M spectral type. Since we do not have stars in this spectral type region, we decided to use the criteria proposed by White & Basri (2003) to select CTTS. We selected 220 CTTSs in NGC 2264 that satisfy at least one of the above spectroscopic criteria.

Using UV excess obtained with MegaCam/CFHT, Venuti et al. (2014) found 66 new CTTS candidates in NGC 2264. These stars do not have FLAMES spectra and were not previously classified as CTTS in the literature or are unknown NGC 2264 members, but since they present considerable UV excess with respect to the WTTS locus, they were added to our CTTS list. This means that based on photometric and spectroscopic accretion criteria, 286 stars are thought to be CTTSs in NGC 2264.

Mon-000056 and Mon-000358 were initially not included in our CTTS list, but they show CoRoT light curves in 2008 and/or 2011 that resemble the AA Tau light curve (see Sect. 4). We would therefore expect them to be CTTSs, but they were not in the fields of our FLAMES observations and show little UV excess. These stars were nevertheless observed with FLAMES/GIRAFFE as part of the Gaia/ESO public spectroscopic survey (Randich et al. 2013; Gilmore et al. 2012). We downloaded the spectra from the ESO science archive and reduced them following the same steps as listed in Sect. 2. The Gaia/ESO spectra show that Mon-000056 presents $EW_{H\alpha} = 2.9 \text{ \AA}$ and $W10\%_{H\alpha} = 276 \text{ km/s}$, while Mon-000358 shows $EW_{H\alpha} = 32.8 \text{ \AA}$ and $W10\%_{H\alpha} = 395 \text{ km/s}$, which allows us to classify them as CTTSs. Our final CTTS list therefore contains 288 stars; it is shown in Table 2. Of these, 58 stars were observed by FLAMES and 159 were observed by CoRoT in the 2008 and/or 2011 campaign, including 12 CTTSs observed by

Table 1. Observations from the Coordinated Synoptic Investigation of NGC 2264

Telescope	Instrument	Dates	Bands
CoRoT	E2 CCD	2011-Dec-1 to 2012-Jan-3	3000 – 10000 Å
VLT	FLAMES/GIRAFFE	2011-Dec-4 to 2012-Feb-29	6470 – 6790 Å
CFHT	MegaCam	2012-Feb-14 to 2012-Feb-28	<i>u</i> and <i>r</i>

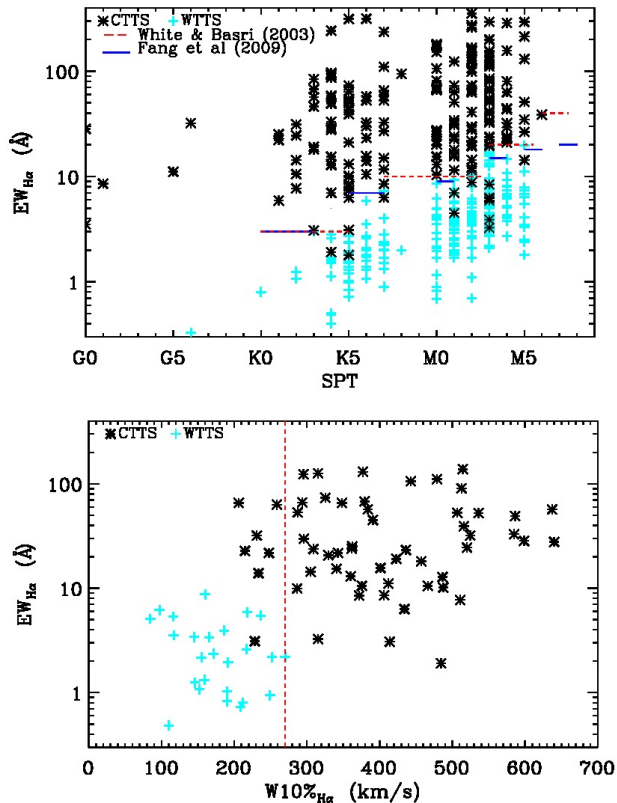


Fig. 2. Spectroscopic criteria used to select CTTSs and WTTSs in NGC 2264. CTTSs are shown as asterisks and WTTSs as plus signs. Top: $H\alpha$ equivalent width vs. spectral type for our sample of stars. Dashed horizontal lines represent the White & Basri (2003) classification threshold and solid horizontal lines the Fang et al. (2009) proposed criteria. Bottom: $H\alpha$ equivalent width vs. $H\alpha$ width at 10% of maximum intensity. The dashed vertical line is drawn at 270 km/s, the separation between CTTSs and WTTSs, according to White & Basri (2003). A few stars do not satisfy one spectroscopic CTTS criterion, but they were classified as CTTSs either based on the other spectroscopic criterion or on the UV excess.

CoRoT only in 2008, 63 only in 2011, and 84 CTTSs that were observed in both campaigns.

We also selected 431 WTTSs among the confirmed members of NGC 2264 that we used as a comparison sample to the accreting CTTS. We added 257 WTTSs to the list based on the $H\alpha$ equivalent width or $W10\%_{H\alpha}$ criteria of White & Basri (2003), previously discussed, and 174 WTTSs were selected based on the criteria discussed in Venuti et al. (2014). Information about the WTTS sample can be found in Table 3. Of the 431 WTTSs, 34 were observed by FLAMES and 308 stars were observed by CoRoT in the 2008 and/or 2011 campaign. We did not analyze the CoRoT data for WTTSs; that is beyond the scope of this paper.

In Fig. 2, we plot the spectroscopic criteria used to distinguish CTTSs from WTTSs, as proposed by White & Basri (2003) and Fang et al. (2009), together with the $H\alpha$ data for the 58 CTTS and 34 WTTS observed with FLAMES. The spectroscopic data of the stars that were not observed with FLAMES come from Dahm & Simon (2005). A few stars do not satisfy the $EW_{H\alpha}$ CTTS criteria, but they were classified as CTTSs based on $W10\%_{H\alpha}$ (Fig. 2, bottom panel) and/or UV excess.

4. Morphology of the CoRoT light curves

The 2008 CTTS light curves were previously classified morphologically as spot-like, AA Tau-like, or non-periodic by Alencar et al. (2010). The spot-like light curves display sinusoidal variations that are due to large, cold spots at the stellar surface, which are very stable on the timescale of the observations (about three weeks). The AA Tau-like light curves show a well-defined maximum interrupted by periodic minima that vary in width and depth from cycle to cycle, like AA Tau itself. They correspond to systems whose light-curve variability is caused by a periodic occultation of the stellar photosphere by circumstellar dust (see McGinnis et al. 2015; Alencar et al. 2010, for more information about AA Tau-like stars in NGC 2264 and Fonseca et al. (2015) for a specific AA Tau-like system, V354 Mon - Mon-000660). Non-periodic light curves may be due, for example, to accretion bursts (Stauffer et al. 2014) or random circumstellar dust obscuration. Some non-periodic light curves are difficult to assign to a major physical phenomenon, however, and are probably the result of different superposed variability processes, such as variable accretion, dust obscuration, and spot variations. We show below by comparing our light-curve classification with accretion diagnostics and inner disk parameters that the morphological classification of the CoRoT light curves is related to the evolution of the accretion process and of the inner disk region.

We morphologically classified the 147 CTTSs light curves observed in 2011 by CoRoT, and in Fig. 3 we show examples of these light curves. In Fig. 4, we present the periodic light curves of Fig. 3 folded in phase with the period obtained with the Scargle periodogram, as modified by Horne & Baliunas (1986). The stability of the spot-like light curve modulation is evident, which contrasts with the high variability of the typical AA Tau-like light curves. A detailed statistical and morphological analysis of the light curves of stars that present infrared excess observed in our campaign with CoRoT and *Spitzer* are discussed in Cody et al. (2014), where the light curves are separated into twelve different classes that represent diverse physical processes and geometric effects. We list in the last column of Table 2 the Q parameter defined by Cody et al. (2014) that can be used as a metric to distinguish periodic and quasi-periodic ($Q < 0.6$) from aperiodic ($Q > 0.6$) light curves.

Table 4 shows some morphological statistics of the CTTS light curves observed with CoRoT in 2008 and 2011. The number of periodic CTTSs did not vary considerably from one run to the other. However, the number of CTTSs observed with CoRoT increased in 2011, and more non-periodic stars were observed in 2011 than in 2008. This was expected, since most of the known

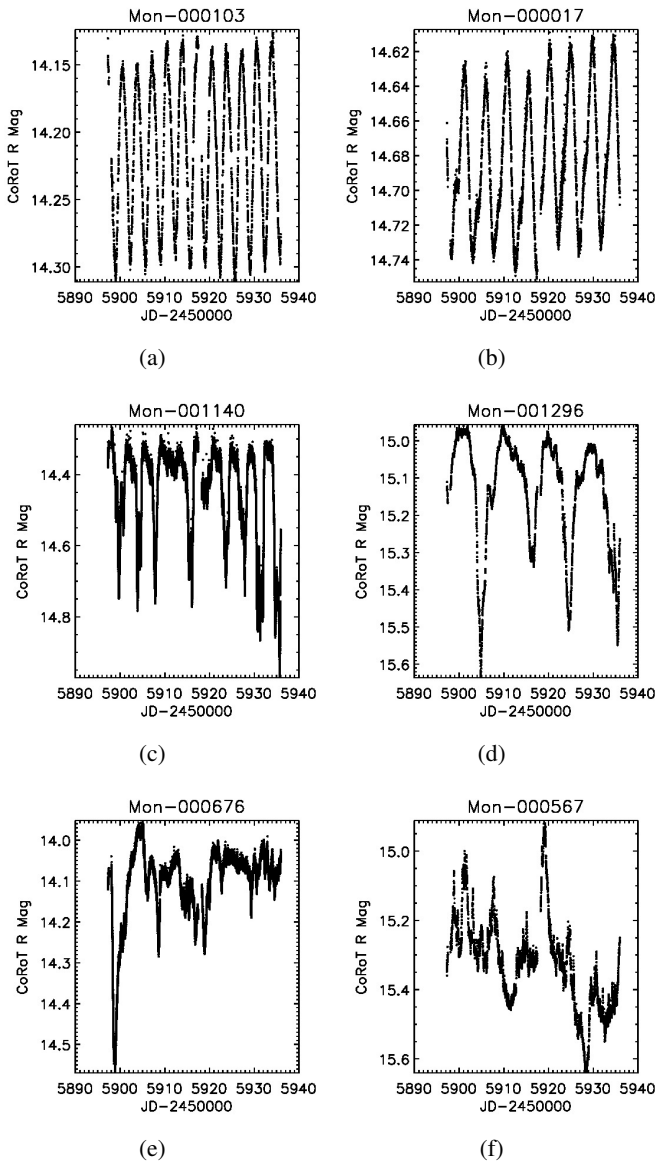


Fig. 3. CoRoT light curves of CTTSs from 2011 showing different photometric variabilities. Panels (a) and (b) correspond to spot-like light curves, (c) and (d) to AA Tau-like light curves, (e) is a non-periodic light curve caused by obscuration by circumstellar material, and (f) is a non-periodic light curve dominated by accretion bursts. The light-curve magnitude was calibrated using the R filter with a zero point of 26.74 mag, as described in Cody et al. (2014).

periodic variable systems were already included in the 2008 run. The number of AA Tau-like systems identified in 2008 differs from that of Alencar et al. (2010), since we were able here to use the simultaneous FLAMES spectroscopy to refine our classification. In addition, Stauffer et al. (2015) identified a new subclass of stars with variable extinction light curves that show periodic, shallow, and short-duration flux dips that are approximately Gaussian in shape. There is some overlap between this new class and the classical AA Tau systems, since a few AA Tau-like stars also present narrow dips superposed on the broad deep minima, as explained in their paper. Light curves labeled “unclassified” in Table 4 correspond to the light curves that we were unable to clearly associate with one major physical phenomenon.

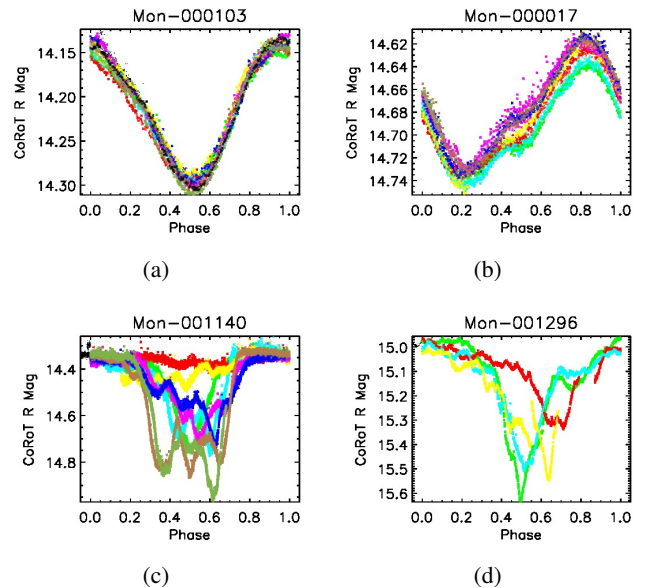


Fig. 4. Periodic CoRoT light curves from Fig. 3 folded in phase. The spot-like light curves present stable variations (top) that contrast with the high variability of the AA Tau-like light curves (bottom). Different colors represent different rotational cycles.

Table 4. Morphological classification of CTTS light curves observed with CoRoT in 2008 and 2011.

Light curve type	N ^o of stars-2008	N ^o of stars-2011
Periodic or quasi-periodic		
Spot	24	19
AA Tau	15	18
Eclipsing binary	2	2
Unclassified	0	4
Non-periodic		
Random extinction	13	13
Accretion bursts	12	20
Unclassified	30	71
Total	96	147

4.1. Morphological changes from 2008 to 2011

Several stars exhibited the same light-curve morphology in 2008 and 2011, but $\sim 30\%$ of the stars presented variations in the morphology of their light curves. We show in Table 5 the variation of morphological classification of the 84 CTTS light curves that were observed in both campaigns. The transition from AA Tau to non-periodic classification and vice versa is common, but we did not observe a transition from AA Tau to spot-like or from spot-like to AA Tau. A few spot-like systems became irregular, and the opposite also occurred. In Fig. 5 (a) and (b), we show the 2008 and 2011 light curves of the CTTS Mon-000928, whose light-curve classification changed between the two runs. In 2008, Mon-000928 was classified as an AA Tau-like system with a maximum brightness periodically interrupted by minima, while in 2011 it was clearly irregular with no detected periodicity. These variations show that the inner disk structure that is responsible for the stellar occultation can move from a well-organized geometry with a stable inner disk warp to a random dust distribution in just a few years. These results may also hint at the typical timescale of stability of the accretion regime, where the accretion geometry evolves from a main accretion fun-

nel in each hemisphere, the base of which may correspond to the stable inner disk warp to an unstable accretion scenario, where random accretion funnels are formed (Kurosawa & Romanova 2013; McGinnis et al. 2015).

In young low-mass stars, cold spots often occupy a substantial fraction of the stellar surface and may last for months to years (e.g., Herbst 1989; Vogt et al. 1999). If the spots indeed did not evolve significantly over a period of few years, then the light curves would also be substantially the same in our two epochs. However, in our sample, 9 of 21 spot-like light curves, observed in both epochs, changed their morphology from 2008 to 2011 and became aperiodic, as seen in Table 5. At the same time, 2 aperiodic light curves in 2008 became spot-like in 2011. In a study of the Orion nebula cluster (ONC), Rebull (2001) analyzed Cousins I_C light curves from young stars and showed that in a one-year interval, about half of the observed periodic spot-like light curves became aperiodic. They also compared their measured periods with the results of similar analyses of the ONC by other authors (Stassun et al. 1999; Herbst et al. 2000) and showed that only about 50% of the periodic systems are typically recovered between the different works. The results above show that cold spots in young stars can evolve substantially and that the observable characteristic features, such as light-curve periodicity, can disappear on a timescale of a few years. Cool spots are expected to be present in all young low-mass stars, but only some of the CTTSs present periodic spot-like light curves, since overlying accretion hot spots and circumstellar dust obscuration can effectively mask cool spot signatures. When CTTSs are observed to switch between variability categories, it is generally attributable to changes in accretion behavior on timescales of a few years or less. In Fig. 5 (c) and (d), we present the 2008 and 2011 light curves of the CTTS Mon-000765, whose light-curve classification changed from aperiodic to spot-like.

Figure 5 shows that flux variations can also be observed from 2008 to 2011 in the spot-like stars that presented a variable light-curve periodicity. During the periodic epoch, most spot-like systems were fainter than in the aperiodic cycles, as seen in Mon-000765 (Fig. 5, lower panels). The brighter phase during the irregular cycles could be due to accretion bursts, leading to the appearance of randomly distributed bright spots at the stellar surface, which would at the same time explain the irregular photometric variability. The AA Tau-like stars also show flux variability between the periodic and aperiodic phases, but in the opposite sense as compared to the spot-like systems: they are generally brighter when periodic, as seen in Mon-000928 (Fig. 5, top panels). These systems are observed at high inclinations with respect to our line of sight ($i > 60^\circ$, see McGinnis et al. 2015), and the aperiodic cycles may correspond to the unstable accretion regime described by Kurosawa et al. (2008) and Kurosawa & Romanova (2013), where multiple accretion streams are randomly formed and occult the star as the system rotates. In this scenario, the star can be partially occulted at all rotational phases, never exhibiting its maximum flux to the observer, and being therefore fainter than in the stable and ordered AA Tau phase. This is consistent with the fact that, in the aperiodic cycles, we generally do not observe a well-defined maximum in the light curves, while in the periodic AA Tau phase a clear maximum is seen, which should correspond to the unocculted photospheric brightness.

4.2. Period distribution

Table 2 shows that $\sim 43\%$ of the 96 CTTSs observed in 2008 and $\sim 29\%$ of the 147 CTTSs observed in 2011 were classified as periodic. We only classified as periodic the light curves that

Table 5. Variations of the morphological classification of the 84 CTTS light curves observed with CoRoT in 2008 and 2011.

Light curve 2008 \rightarrow Light curve 2011	N ^o of stars
Spot \rightarrow AA Tau	0
Spot \rightarrow non-periodic	9
AA Tau \rightarrow spot	0
AA Tau \rightarrow non-periodic	5
Non-periodic \rightarrow AA Tau	8
Non-periodic \rightarrow spot	2
Non-periodic \rightarrow periodic unclassified	1
AA Tau \rightarrow AA Tau	8
Spot \rightarrow spot	12
Non-periodic \rightarrow non-periodic	37
Binary \rightarrow binary	2

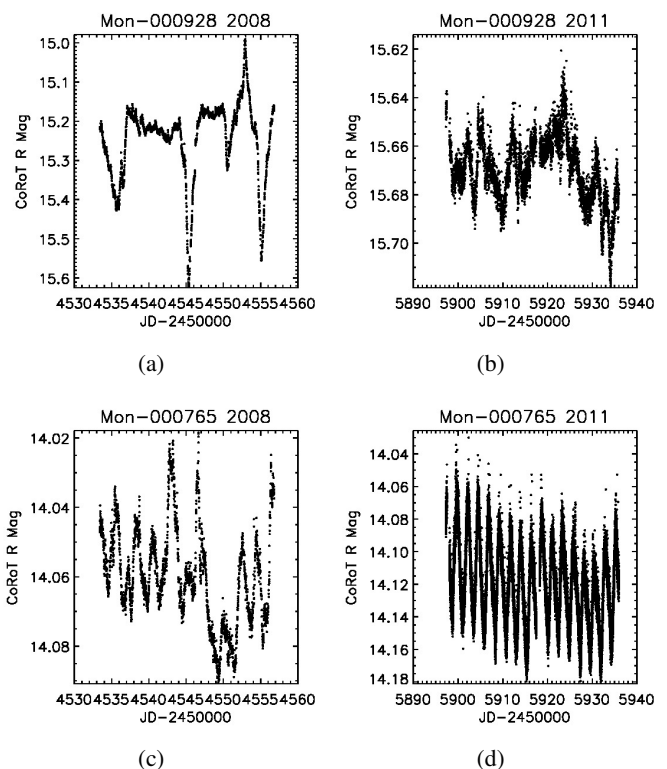


Fig. 5. Examples of CTTSs whose morphological classification of the light curve varied from 2008 to 2011. Mon-000928 displays an AA-Tau-like light curve in 2008 (a) with a period of $P = 4.96$ days, while in 2011 the light curve was aperiodic (b). Mon-000765 was aperiodic in 2008 (c), while in 2011 the light curve was spot-like with a period of $P = 2.41$ days (d).

presented a high-power, detached, and dominant peak in the periodogram analysis. We established a minimum power level of the periodogram for a reliable detection based on the periodogram analysis of the sinusoidal spot-like light curves, which are clearly periodic with a well-determined period within our dataset. We also inspected by eye each of the periodic light curves folded in phase at the measured period and verified that they presented phase coherence.

Many light curves that show some periodic signal, but with low power in the periodogram, were conservatively classified as non-periodic in the present work. Venuti et al. (in preparation) discuss the periodicity of all the stars observed by CoRoT in more detail and the number of periodic stars may be some-

what different from ours. We present in Fig. 6 the period distribution of AA Tau-like and spot-like systems observed in 2008 and 2011. Despite the observed morphological variations in the light curves from 2008 to 2011 (Table 5), the overall period distribution did not vary significantly from 2008 to 2011. As seen in Fig. 6, there are more AA Tau-like stars with long photometric periods in the new campaign. This is probably due to the difference in datasets between the two campaigns and to the longer observation time span in 2011 (40 days) than in 2008 (23 days), which makes it easier to confidently determine longer periods in the irregular, though periodic, AA Tau-like light curves. Despite the longer observational time span, we did not detect longer spot-like periods in 2011. In 2008 and 2011 the spot-like light curves were very regular and their periods were easily measured with our data. Therefore, the lack of periods longer than 14 days in 2008 and 10 days in 2011 is probably real among the observed CTTSs. The longer periods measured were different in both campaigns, and this is due to different samples, since the stars observed in each run were not exactly the same, and it is due to accretion variability, since some spot-like systems became aperiodic and the opposite also occurred between the two observational runs.

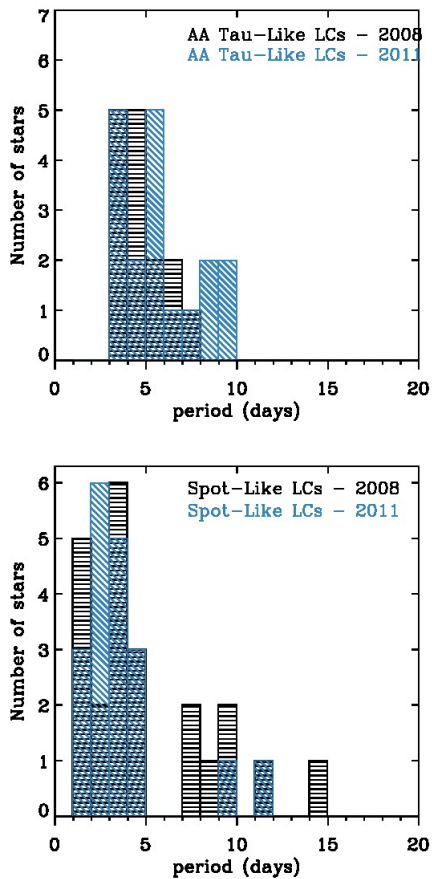


Fig. 6. Period distribution of the CTTSs observed in 2008 (black) and 2011 (blue). Top: AA Tau-like light curves. Bottom: Spot-like light curves. AA Tau-like stars clearly present periods within the range of spot-like systems.

The period of a spot-like light curve is the rotational period of the star, since spots are located on the stellar surface. In both epochs, the AA Tau-like stars presented periods within the range of periods measured in the spot-like light curves. Therefore, the material that obscures the AA Tau-like stars is probably not lo-

cated very far from the corotation radius of the star-disk system, as pointed out by Alencar et al. (2010). A more detailed analysis of the period distribution of CTTSs and WTTSs in NGC 2264 and the implication for angular momentum evolution will be presented in another paper (Venuti et al., in preparation).

5. UV excess and photometric mass-accretion rates

In this section, we compare the CoRoT light-curve morphology with accretion diagnostics and disk indicators to determine whether the optical light-curve morphology and accretion and inner dusty disk evolution are related.

Venuti et al. (2014) obtained the UV excess emission of CTTSs and WTTSs in NGC 2264 using u - and r -band measurements from CFHT data. They determined the locus of WTTSs in the r vs. $u-r$ color-magnitude diagram that was fitted with a polynomial function, which was used as a reference value to non-accreting systems. The UV excess of a CTTS was defined as $E(u) = (u-r)_{\text{obs}} - (u-r)_{\text{ref}}$, where $(u-r)_{\text{obs}}$ is the observed CTTS color, and $(u-r)_{\text{ref}}$ is the reference color at magnitude r_{obs} . The UV excess measurements have an average rms error of 0.16 mag to account for the distribution of WTTS around the reference sequence (Venuti et al. 2014). With the UV excess, Venuti et al. (2014) calculated mass-accretion rates (\dot{M}_{UV}) for the CTTSs in NGC 2264. We show in Fig. 7 the UV excess (top) and mass-accretion rate (bottom) vs. $H\alpha$ equivalent width for the stars in our sample. Stars presenting accretion burst light curves show some of the highest UV excesses (more negative on the scale of the plot) and consequently the highest mass-accretion rates among the observed systems, as noted by Stauffer et al. (2014). This is supported by a two-sided Kolmogorov-Smirnov test that shows that the mass-accretion rate distribution of accretion burst stars, when compared to spot-like and AA Tau-like systems, has only a 5.8×10^{-6} probability to be equivalent. AA Tau-like and spot-like stars are an intermediate population between the accretion bursts systems and WTTSs, which present low UV excess. The mean UV excess values of each light curve group corroborate with this analysis: -1.15 for the accretion bursts, -0.04 for the AA Tau systems, 0.05 for the spot-like systems, and 0.14 for the WTTSs. These results suggest that the CoRoT light curve morphology is related to the evolution of the accretion process.

Many of the stars observed by CoRoT have *Spitzer* observations from the literature (Teixeira et al. 2012), which allowed us to compute the α_{IRAC} index, as proposed by Lada et al. (2006). This index is the slope of the spectral energy distribution between $3.6 \mu\text{m}$ and $8 \mu\text{m}$, and it allows a classification of inner disk evolution. If $\alpha_{\text{IRAC}} < -2.56$, the disk is classified as a naked photosphere (no dust in the inner disk). For systems with $-2.56 < \alpha_{\text{IRAC}} < -1.80$, the inner disk is optically thin and called an anemic disk. For stars with $-1.80 < \alpha_{\text{IRAC}} < -0.5$, the inner disk is classified as optically thick. Stars with $-0.5 < \alpha_{\text{IRAC}} < 0.5$ are classified as flat spectrum sources, and $\alpha_{\text{IRAC}} > 0.5$ characterizes class I sources.

In Fig. 8, we show the α_{IRAC} index vs. the UV excess calculated by Venuti et al. (2014). Most of the CTTSs present dust in the inner disk. Spot-like systems are present in all the inner disk classes, but are mostly found among the anemic disks and naked photosphere populations. All AA Tau-like systems have dust in the inner disk, which is important, since we assumed their light-curve variability to be dominated by circumstellar dust extinction from that region. Most of the accretion burst systems present thick disks, which is consistent with an earlier disk evolution and accretion phase than the AA Tau-like stars. The mean α_{IRAC} values of each light-curve group corroborate this analysis: -1.42 for

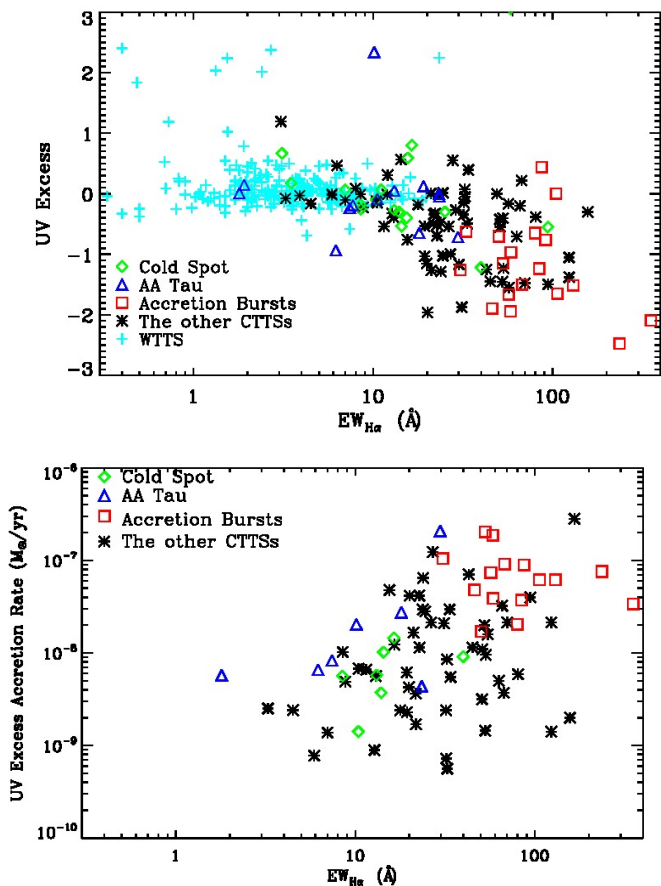


Fig. 7. Comparison between the CoRoT light-curve classification and UV excess (top) or mass-accretion rates (bottom) calculated by Venuti et al. (2014). In the top plot, more negative values indicate higher UV excess.

the accretion bursts, -1.71 for the AA Tau systems, -1.84 for the spot-like systems, and -2.76 , for the WTTs. These results show that the CoRoT light-curve morphology is related to the evolution of the inner disk. It also shows that accretion and disk evolution are related to each other, since the stars with highest UV excesses (more negative values) are the ones with the dustiest inner disks, while stars with little or no sign of accretion have almost no dust in their inner disks.

Figure 8 also shows some interesting objects that deserve further investigation, which beyond the scope of the present paper, however, such as the WTTs among the anemic and thick disk systems. These are non-accreting stars (based on spectra) that still show substantial dust in their inner disks. In spite of this, for some as yet unknown reason, accretion has been shut off or is at a very low level in these systems, at least at the time of spectroscopic observation. There is also a significant number of anemic disk candidates among the CTTSs, with various light-curve morphologies that would be interesting targets to investigate the inner disk dispersal in accreting systems.

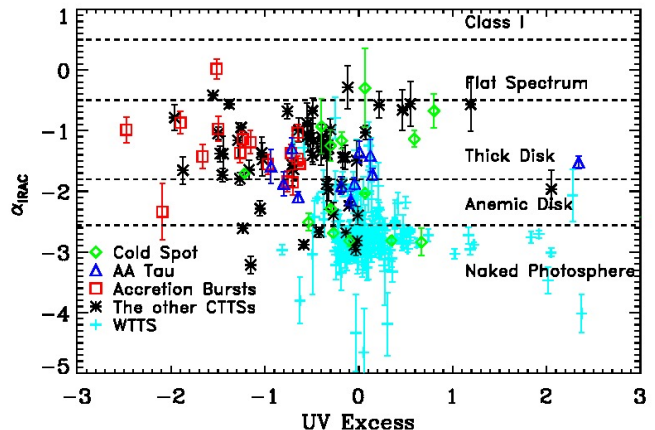


Fig. 8. Comparison between the CoRoT light-curve classification with the UV excess from Venuti et al. (2014) and the slope of the spectral energy distribution from $3.6 \mu\text{m}$ to $8 \mu\text{m}$ (α_{IRAC}). These results show that the CoRoT light-curve morphology is related to the accretion process and the evolution of dust in the inner disk.

6. Equivalent width and accretion rates from the $H\alpha$ line

The $H\alpha$ line of a CTTS is generally quite strong and wide and is often characterized by its equivalent width. Compared to the morphology of the CoRoT light curves, the accretion burst systems show the highest $EW_{H\alpha}$ in our sample, with an average value of $96 \pm 19 \text{ \AA}$, clearly distinguishable from the AA Tau and spot-like systems. AA Tau-like stars present an average $EW_{H\alpha}$ of $13.2 \pm 2.4 \text{ \AA}$, while CTTSs with spot-like light curves present a mean $EW_{H\alpha}$ value of $21.1 \pm 5.6 \text{ \AA}$. The uncertainties correspond to the standard deviations of the measured equivalent width values. The distribution of $EW_{H\alpha}$ among the three CTTS groups is shown in Fig. 9, where we included $EW_{H\alpha}$ measurements from Dahm & Simon (2005) for the stars that we did not observe. The same tendency is observed with the $H\alpha$ width at 10% of maximum line intensity.

Mass-accretion rates ($\dot{M}_{H\alpha}$) are frequently calculated from the $H\alpha$ line flux, using calibrations such as the ones proposed by Fang et al. (2009) and Gullbring et al. (1998). We compared the mass-accretion rates obtained from the UV excess by Venuti et al. (2014) with the values obtained with the $H\alpha$ flux, as described below.

We calculated the $H\alpha$ flux ($F_{H\alpha}$) from the $EW_{H\alpha}$,

$$F_{H\alpha} = EW_{H\alpha} F_c(H\alpha), \quad (1)$$

where $F_c(H\alpha)$ is the continuum flux in the $H\alpha$ region. Since the FLAMES spectra were not flux calibrated, we estimated $F_c(H\alpha)$ from the CoRoT flux using CoRoT observations obtained simultaneously with the FLAMES spectra. The CoRoT flux was converted into R magnitudes using the R -band photometry zero-point of 26.74, as determined by Cody et al. (2014). For the stars observed with FLAMES that were not observed with CoRoT in 2011, we used the continuum flux from the CFHT r band (Venuti et al. 2014) taken simultaneously with the FLAMES observations. The continuum flux was then corrected for extinction with A_V obtained from the CFHT data (Venuti et al. 2014).

The $H\alpha$ luminosity was then computed as $L_{H\alpha} = 4\pi d^2 F_{H\alpha}$, where we used $d = 760 \text{ pc}$ (Sung et al. 1997) as the distance

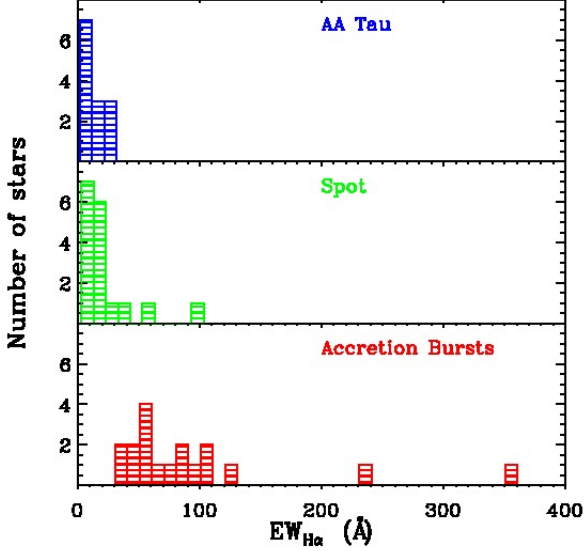


Fig. 9. Distribution of $H\alpha$ equivalent width of CTTs that present AA Tau-like (top), spot-like (middle), and accretion burst (bottom) light curves.

to the cluster. We used the fit proposed by Fang et al. (2009) to calculate the accretion luminosity (L_{acc}) from $L_{H\alpha}$:

$$\log\left(\frac{L_{\text{acc}}}{L_{\odot}}\right) = (2.27 \pm 0.23) + (1.25 \pm 0.07) \log\left(\frac{L_{H\alpha}}{L_{\odot}}\right). \quad (2)$$

With the accretion luminosity, we obtained the mass-accretion rate,

$$\dot{M}_{H\alpha} = \frac{L_{\text{acc}} R_*}{GM_* \left(1 - \frac{R_*}{R_{\text{in}}}\right)}, \quad (3)$$

where R_* and M_* are the radius and mass of the star, respectively, taken from Venuti et al. (2014), and G denotes the gravitational constant. The inner radius was set to $R_{\text{in}} = 5 R_*$, which is a standard value of the disk truncation radius of CTTs (Gullbring et al. 1998). The individual values of mass-accretion rates calculated from the $H\alpha$ line flux are presented in Table 6.

Figure 10 shows the mass-accretion rates obtained from the mean $H\alpha$ equivalent width of the four to six FLAMES and CoRoT simultaneous observations, and also those obtained from simultaneous CFHT observations. We plot the mean $\text{EW}_{H\alpha}$, and the error bar represents the night-to-night variability of $\text{EW}_{H\alpha}$ and $\dot{M}_{H\alpha}$. As observed with the \dot{M}_{UV} relation (Fig. 7), stars that present accretion burst light curves have higher $\dot{M}_{H\alpha}$. Since WTTSs are not actually accreting, their $H\alpha$ equivalent widths are probably of chromospheric origin, a contribution that is also present in the CTTs spectra. Therefore, the mass-accretion rate locus of WTTSs represents a lower limit to our ability to measure mass-accretion rates of CTTs from the $H\alpha$ equivalent width in our sample, as discussed by Ingleby et al. (2011) and Manara et al. (2013).

Figure 11 shows the relation of the mass-accretion rates calculated with the UV excess and $H\alpha$ equivalent width. The two methods show similar tendencies, but the individual value can sometimes be different. This difference may arise because the

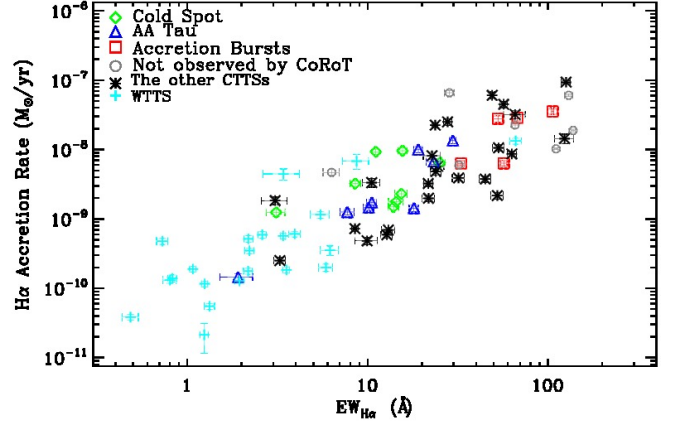


Fig. 10. Comparison between the CoRoT light-curve classification and mass-accretion rates obtained from $H\alpha$ flux as a function of $H\alpha$ equivalent width (FLAMES/VLT data). The error bars represent the night-to-night variability of the line flux.

$H\alpha$ line does not necessarily originate in the accretion columns alone, but can also have contributions from the disk wind and accretion shock, as absorptions superposed on the accretion profile. When we calculated the $H\alpha$ equivalent width, the absorptions decrease the measured $\text{EW}_{H\alpha}$ value, leading to lower values of mass-accretion rates. At the same time, the errors in A_V affect the UV excess accretion rates more than the $H\alpha$ ones and can lead to more uncertain values of mass-accretion rates calculated from UV excess. Although UV excess is clearly a more direct measurement of the mass-accretion rate, $H\alpha$ line fluxes are much easier to obtain and allow for a good estimate of mass-accretion rates for all accreting objects, even those that do not present a substantial UV excess, due, for example, to circumstellar dust obscuration of the hot spot.

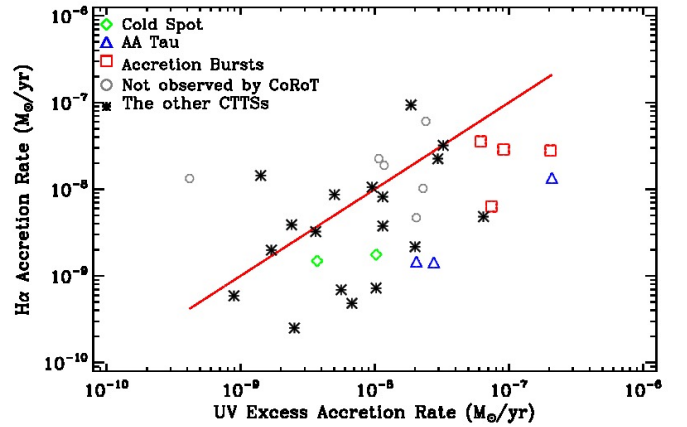


Fig. 11. Comparison between mass-accretion rates obtained from $H\alpha$ flux with the UV excess mass-accretion rates. The red line shows a slope equal to 1.

7. $H\alpha$ line variability

The CTTs in NGC 2264 present a variety of $H\alpha$ line profiles. In this section, we verify how common each $H\alpha$ profile type is and compare its occurrence with the CoRoT light-curve classification. We followed the $H\alpha$ profile classification proposed by

Reipurth et al. (1996), which is divided into seven profile types. A type I profile is symmetric and shows no absorption feature. A type II profile presents two peaks, and the less intense one exceeds half the intensity of the main peak. A type III profile also shows two peaks, and the less intense one is smaller than half the intensity of the main peak. A type IV profile shows a pronounced absorption feature on the blue or red side of the line where no emission is seen, like a P Cygni or inverse P Cygni profile. The letters B or R are attached to types II, III and IV, depending on the location (in the blue (B) or red (R) side of the line) of the secondary peak or absorption feature with respect to the main peak. We have 20 to 22 nights of observation of each target, and the $H\alpha$ line is quite variable both in intensity and shape from night to night. Therefore, we morphologically classified only the mean $H\alpha$ profile of each star and present this classification in Table 6 and Fig. 12. The top panel of Fig. 12 shows the profile distribution of all CTTs observed with FLAMES. Type I is the most common $H\alpha$ profile in our sample. This profile corresponds to a main emission feature without any prominent absorption and is attributed to magnetospheric accretion. The emission profiles of type I stars sometimes display some superposed absorption in one or a few observing nights, but the analyzed mean profile effectively does not present absorptions.

Figure 12 (bottom) shows the distribution of the $H\alpha$ profile types according to the CoRoT light-curve classification. Spot-like stars typically present type I $H\alpha$ profiles, generally showing no evidence of blueshifted absorption due to wind, or redshifted absorption due to hot spot photons absorbed by the accretion funnel. Moreover, AA Tau-like stars tend to present type IIR and IIR profiles, which are characterized by redshifted absorptions, compared to the most common type I profile seen among the CTTs in our sample.

Kurosawa et al. (2006) used disk-wind and magnetosphere radiative transfer models for CTTs to examine the $H\alpha$ classification proposed by Reipurth et al. (1996) and with a range of parameters reproduced all the $H\alpha$ profile types. In general, they found that the type I profile is the most common among CTTs, since it is produced from a range of system inclinations and is dominated by magnetospheric emission. Kurosawa et al. (2006) found that type IIB and IIR profiles were equally common, as also found by Reipurth et al. (1996) and by us, since they result from the same physical conditions, with the exception of the system inclination. Type IIB needs medium inclinations to be produced, while type IIR results from high inclinations. This is also consistent with our results, since most AA Tau-like stars, which are high-inclination systems (McGinnis et al. 2015), tend to present type IIR profiles (see Fig. 12, bottom).

Reipurth et al. (1996) instead found that the $H\alpha$ profile distribution in their sample was dominated by type IIB profiles (33% of their sample), while in our sample only $\sim 9\%$ of the observed CTTs present type IIB profiles. In the models of Kurosawa et al. (2006), only high mass-accretion rate stars presented type IIB profiles. The difference in profile distribution found by us and Reipurth et al. (1996) might therefore simply be due to a sample selection effect. The stars classified as type IIB by Reipurth et al. (1996) have spectral types between G0 and K7 and a very high $H\alpha$ equivalent width (average value of 64 \AA), which may indeed indicate that they are high mass-accretion rate systems. The type IIB CTTs in our sample present an average EW of 47 \AA and a mean mass-accretion rate of $\sim 2.5 \times 10^{-8} M_{\odot}/\text{yr}$, which is not particularly high, but does correspond to one of the highest mean mass-accretion rates of the various profile types.

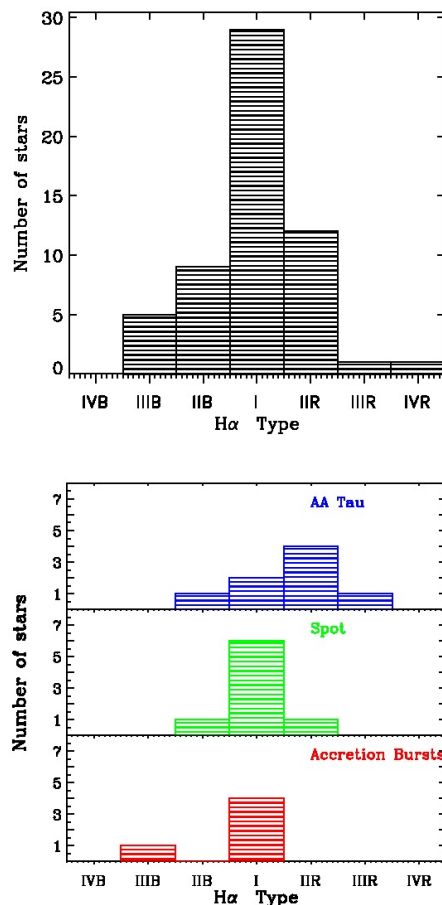


Fig. 12. Distribution of $H\alpha$ profile types according to the classification of Reipurth et al. (1996). Top: All the CTTs observed with FLAMES. Bottom: CTTs observed both with FLAMES and CoRoT. Light curves classified as spot-like, AA Tau-like, and accretion burst are shown as a function of profile type.

8. Periodograms of $H\alpha$ emission line

As the star-disk system rotates, the observed $H\alpha$ line of CTTs varies in intensity and shape. This is expected to occur, even in a stable accretion regime, if the stellar magnetic and rotation axis are not aligned. The misalignment between the axes breaks the axisymmetry of the accretion environment and creates individual accretion funnels in each hemisphere. The projection of the $H\alpha$ emission region in our line of sight will then be different at every rotational phase, which will cause line variability (see for example Alencar et al. 2012). If most of the $H\alpha$ line is formed in the accretion columns, we would expect to measure a periodic line variability when the star is in a stable accretion regime. However, the $H\alpha$ line may also form in different circumstellar regions, such as the chromosphere, disk wind, and jet, and each region may have a different periodicity. This would make a single period difficult to detect. With 20 to 22 nights of observation of each target with the FLAMES spectrograph, we can check whether the $H\alpha$ line variations were periodic, and compare these periods with the periodicities measured photometrically. This will allow us to infer if the $H\alpha$ line-forming region is directly related to the physical process causing the photometric variability.

We analyzed the line periodicity by calculating Scargle periodograms, as modified by Horne & Baliunas (1986), along the line profile. The Scargle periodograms fit the data with sinu-

soidal functions through a least-squares method. The code requires a range of periods to be tested, and the best fit corresponds to the highest power in the periodogram. To obtain the periodicity in the $H\alpha$ line, we divided each normalized $H\alpha$ line profile into small velocity intervals (0.5 km/s). For each velocity interval, Scargle periodograms were independently calculated. Each periodogram was grouped side by side in velocity, to form a diagram of period vs. velocity. The power of the periodogram is represented by colors, varying from zero (white) to the maximum power intensity (black). With this procedure, we can check how each period spreads across the $H\alpha$ line. Periodic signals only in a few velocity bins may not be significant, but periodic signals that are spread across several velocity channels indicate periodicity in an extended region of line formation. We can also verify if there are different periodicities in different line regions (like in emission and absorption).

Only eight CTTSs observed with the FLAMES spectrograph presented a periodic signal in the $H\alpha$ line (see Table 6), and their periodograms are shown in Figs. 13, 14, and 15. These figures are discussed individually in the following subsections, where we show that most of the periodicity in the $H\alpha$ line occurs in the red wing, which comes from gas moving away from the observer and probably is related to the accretion process. These periodic stars presented organized and stable accretion regions rotationally modulated by the stellar magnetic field.

Our spectroscopic target selection in 2011 was largely based on the CoRoT light-curve classification from 2008, and we included as many AA Tau-like and spot-like systems as possible in our two pointings to study periodic systems. We did not anticipate, however, that a large number of systems would change their light-curve variability from periodic to aperiodic between the two runs. Of the 58 stars observed with FLAMES, only 16 presented periodic CoRoT light curves in 2011, 8 of which were classified as AA Tau-like and the other 8 as spot-like systems. Probably because of our unfortunate selection, the $H\alpha$ line of most of the 58 observed CTTSs showed no periodicity in our data.

In the next subsections, we analyze the $H\alpha$ periodicity compared to the CoRoT light-curve morphology discussed in Sect. 4. Because of the large number of stars observed spectroscopically with FLAMES that presented a non-periodic CoRoT light curve in 2011, our main conclusion is that the stars that presented non-periodic CoRoT light curves are generally not periodic in $H\alpha$ either. We show in Sect. 10 that the lack of periodicity in $H\alpha$ and in the photometry may be caused by an unstable accretion regime, as proposed by Kurosawa & Romanova (2013).

8.1. $H\alpha$ periodicity in the AA Tau-like stars

AA Tau-like stars are expected to be in a stable accretion regime, where a major funnel flow is formed in each hemisphere, and the base is associated with an inner disk warp that periodically occults the star as the system rotates (Bouvier et al. 2007a; Kurosawa et al. 2008). The photometric period of AA Tau-like stars corresponds to the Keplerian period of the occulting circumstellar material, and it can be different from the stellar rotation period, unless the structure responsible for the occultation of the star is at the disk corotation radius. As shown in Sect. 4.2, at least in our sample, the photometric periods of AA Tau-like systems is not expected to differ substantially from the stellar rotation period, indicating that the inner disk warp is indeed located close to the disk corotation radius. Eight AA Tau-like stars were observed with the FLAMES spectrograph, but only three are periodic in $H\alpha$ (see Fig. 13). This is somewhat unexpected. If the

eight stars were in a stable accretion regime, it would naturally produce periodic variability in $H\alpha$ if the line were mostly formed in the accretion funnel. However, if the accretion flow is significantly time variable, it could mask the periodicity imposed by the stellar rotation. We will explore evidence for the time variability of accretion during funnel-flow accretion in a forthcoming paper (Stauffer et al., in preparation).

The star Mon-000660 (V354 Mon), Fig. 13abc, is an AA Tau-like analog that presents the same period in $H\alpha$ and the photometry. Assuming that $H\alpha$ is formed mainly in the accretion funnel and that the measured period corresponds to the stellar rotational period, it confirms that the occulting disk structure, which causes the photometric variability, is located at the corotation radius, as in AA Tau itself (Bouvier et al. 2007a). Another AA Tau-like star, Mon-000250, Fig. 13def, is also periodic in $H\alpha$ and presents the same period in the photometry. In the $H\alpha$ periodogram, this star shows two periodic signals in the red wing, the stronger power peak coincident with the photometric period (~ 8.9 days) and the weaker peak around ~ 7.5 days. This second period is also detected in the CoRoT light curve, but with a lower power than the main periodic signal, and is due to the periodicity of a small structure present inside the deepest dips of the light curve (see Fig. 13f).

On the other hand, star Mon-000811, Fig. 13ghi, which is also AA Tau-like, only shows a faint hint of periodicity in $H\alpha$ at the photometric period (~ 7.9 days), and presents a strong periodic detection at about 13 days in the $H\alpha$ blue wing. This star also presents two periodic signals in the HeI 6678 Å line, one at the photometric period and another at about 11 days, as shown in Sect. 9. The HeI line is expected to be formed near the hot spot, close to the stellar photosphere, so one of its periodicities is probably close to the stellar rotation period. If the approximately eight-day period of HeI corresponds to the stellar rotational period, the structure that occults the star could be located close to the corotation radius of the star-disk system. This is the only star that presents a periodicity only in the blue wing of the $H\alpha$ line. Mon-000811 can be compared to the CTTS SU Aur, which exhibited a blueshifted absorption in $H\alpha$ that is periodic (Johns & Basri 1994), and thought to be due to a wind (Giampapa et al. 1993). Its variability is explained as rotational modulation of the wind by the magnetic field of SU Aur. Mon-000811 shows no absorption in the blue wing of $H\alpha$ (as seen in Fig. 13h), and we cannot easily associate the observed periodicity in the blue wing with a wind. However, the blue-wing period is longer than the HeI period (which we associate with the rotation period), so the material responsible for the $H\alpha$ blue-wing periodicity is probably located outside the corotation radius and could indeed come from a disk wind.

As discussed above, three AA Tau-like stars present the same periodicity in the photometric and spectroscopic analysis. Since the spectroscopic periods most likely correspond to the stellar rotational periods, we can assume that, at least in these three cases, the inner disk warp is located at the corotation radius. Following Bessolaz et al. (2008), we computed the star-disk corotation radius and calculated the magnetic field strength needed to enforce disk truncation at the corotation radius. The results are presented in Table 7. At a few stellar radii from the star, the star-disk interaction is expected to occur mostly through the dipole component of the stellar magnetic field, and the calculated magnetic fields in Table 7 are within the range of values of the few dipole components measured in CTTSs ($B_{\text{dip}} = 0.02$ kG to 1.9 kG) (see Table 2 from Gregory et al. 2012).

Table 6. Periods of the classical T Tauri stars observed with the FLAMES spectrograph obtained with photometric and spectroscopic diagnostics.

Mon ID ^a	LC_2008 ^b	P _{CoRoT_2008} ^b (days)	LC_2011 ^b	P _{CoRoT_2011} ^b (days)	P _{Hα} ^c (days)	P _{HeI} ^d (days)	Regime ^e	H α Type ^f	M _{Hα} ^g (M _{\odot} /yr)
CSIMon-001099	1	3.31	1	3.38	NP	-	S	IIB	3.23e-09
CSIMon-000103	1	1.67	1	3.35	NP	-		I	9.61e-09
CSIMon-000177	1	3.01	1	3.01	NP	-		I	9.29e-09
CSIMon-000335	1	4.51	1	4.58	NP	-		I	2.31e-09
CSIMon-000965	1	9.38	1	9.68	NP	9.4	S	IIR	1.76e-09
CSIMon-000810	1	2.93	1	2.93	NP	-		I	1.24e-09
CSIMon-000964	1	3.34	1	3.32	NP	-		I	1.49e-09
CSIMon-000326	1	7.05	3		NP	NP		I	1.99e-09
CSIMon-000220	1	0.76	3		NP	-		I	2.50e-10
CSIMon-000804	1	3.23	3		NP	-		I	4.83e-10
CSIMon-001033	1	14.15	-		6.30	-	S	IIR	4.69e-09
CSIMon-000250	2	4.16	2	8.93	7.5/8.9	8.6	S	IIR	1.44e-09
CSIMon-000660	2	5.25	2	5.10	5.2	-	S	IIIR	1.45e-10
CSIMon-000498	2	4.23	2	4.28	NP	-		I	1.00e-08
CSIMon-001199	2	3.75	2	3.61	NP	-		IIB	1.46e-09
CSIMon-000297	2	3.16	3 (E)		NP	-		IIR	5.75e-09
CSIMon-000928	2	4.96	3		NP	10.3		I	6.91e-10
CSIMon-000654	2	4.66	3 (E)		NP	NP		I	4.82e-09
CSIMon-000441	2	4.06	3 (E)		NP	Noise		IIB	3.24e-09
CSIMon-000824	2	7.05	-		NP	-	U	IVR	3.28e-09
CSIMon-001144	3 (E)		3 (E)		NP	Noise		II	2.17e-09
CSIMon-001275	3		3		NP	-		IIIB	2.51e-08
CSIMon-000119	3		3		NP	NP		IIIB	3.34e-09
CSIMon-000558	3 (A)		3	11.70?	10.5	10.7		IIB	6.06e-08
CSIMon-000168	3 (E)		3 (E)		NP	Noise		II	3.77e-09
CSIMon-000926	3		3		NP	NP		I	8.66e-09
CSIMon-000681	3 (E)		3 (E)		NP	NP		IIB	4.49e-08
CSIMon-000280	3		3		NP	-		IIR	5.90e-10
CSIMon-000290	3		3		NP	8.3/11.4		I	2.25e-08
CSIMon-000328	3		3		NP	NP		I	3.90e-09
CSIMon-000448	3		3		NP	Noise		I	8.16e-09
CSIMon-000314	3 (E)		3 (E)		NP	Noise		I	1.06e-08
CSIMon-000951	3		3		NP	Noise		I	3.21e-08
CSIMon-000937	3		3		NP	-		I	7.24e-10
CSIMon-000667	3 (E)		3 (E)		5.9	-	S	IIB	1.84e-09
CSIMon-000945	3 (A)		3 (A)		NP	7.4		I	6.35e-09
CSIMon-001022	3 (A)		3 (A)		NP	8.9/12.5		IIIB	6.31e-09
CSIMon-000996	3 (A)		3 (A)		8.3	8.3		I	2.79e-08
CSIMon-000510	3 (A)		3 (A)		NP	NP		I	2.87e-08
CSIMon-000341	3 (A)		3 (A)		NP	NP		I	3.55e-08
CSIMon-000370	3		3	11.82?	NP	NP		I	2.55e-08
CSIMon-000765	3		1	2.41	NP	-		I	6.48e-09
CSIMon-000379	3 (E)		2	3.68	NP	-	S	IIR	1.26e-09
CSIMon-001054	3 (E)		2	4.08/8.17*	NP	8.1		I	1.35e-08
CSIMon-000296	3 (E)		2	3.91	NP	-	S	IIR	1.73e-09
CSIMon-000811	3 (E)		2	7.88	12.5	10.5	S	IIR	6.75e-09
CSIMon-000846	3		-		NP	NP		I	-
CSIMon-000795	3		-		NP	NP		IIB	6.59e-08
CSIMon-000457	3		-		NP	-		IIIB	6.01e-09
CSIMon-000260	3 (E)		-		NP	9.2		IIB	2.26e-08
CSIMon-000893	3		-		NP	NP		I	1.02e-08
CSIMon-000131	-		3		NP	9.1		IIR	-
CSIMon-000423	-		3		NP	Noise		I	1.44e-08
CSIMon-000632	-		-		NP	Noise		IIB	1.33e-08
CSIMon-001287	-		-		NP	Noise		IIR	9.38e-08
CSIMon-000603	-		-		NP	Noise		IIIB	6.07e-08
CSIMon-000239	-		-		5.6	-		?	-
CSIMon-001128	-		-		NP	Noise		I	1.88e-08

Notes. This table is ordered by the classification of the CoRoT light-curve morphology from the 2008 campaign.

^(a) CSIMon is an internal identification of the CSI 2264 campaign. ^(b) CoRoT light-curve morphology and photometric period obtained in this work: 1= spot-like, 2= AA Tau-like, 3= non-periodic light curves. Accretion bursts stars and aperiodic extinction light curves are identified by (A) and (E), respectively. ^(c) Period obtained with the H α line from FLAMES spectra. NP denotes a non-periodic line. ^(d) Period obtained with HeI line 6678Å from FLAMES spectra. Noise means that the HeI line is present on the spectrum but it is dominated by noise. ^(e) Accretion regime: S-stable and U-unstable, as discussed in Sect. 10. ^(f) Morphology of H α line by Reipurth et al. (1996) discussed in Sect. 7. ^(g) Mass-accretion rates calculated with H α equivalent width. ^(h) The photometric period was obtained using Scargle periodogram and auto-correlation function, as explained in Sect. 9.1.

8.2. H α periodicity in stars classified as non-periodic with the CoRoT photometry

The stars Mon-000667 (random occultation by circumstellar material), Mon-000996 (accretion burst), and Mon-000558 (irregu-

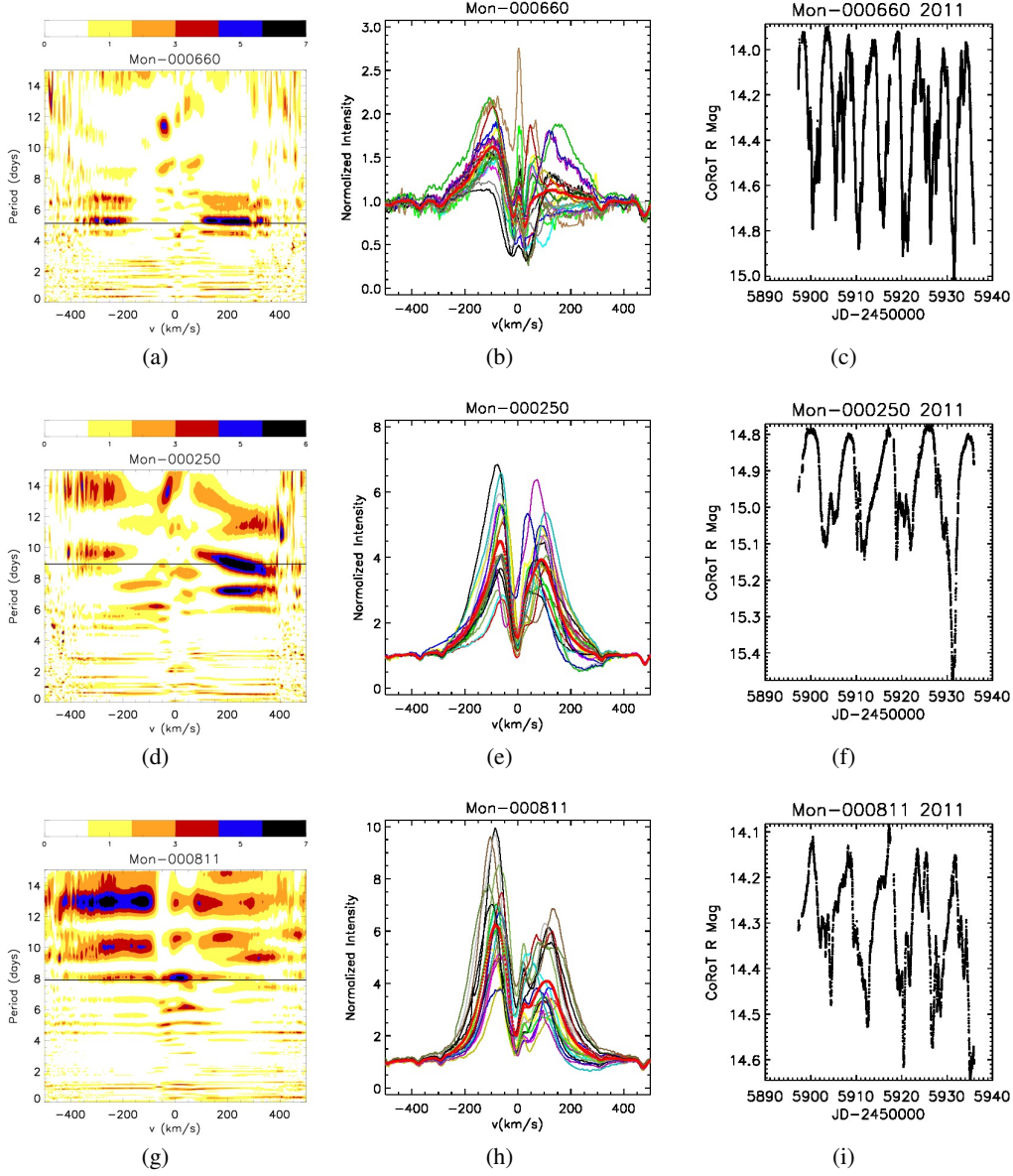


Fig. 13. AA Tau-like stars in 2011 that present a periodicity in the $H\alpha$ line. Left column: Bidimensional periodograms of the $H\alpha$ line. The color code represents the power of periodogram, varying from zero (white) to the maximum power intensity (black). The black horizontal lines correspond to the photometric period of the 2011 CoRoT light curves. Middle column: $H\alpha$ line profiles. Different colors correspond to different observation nights, and the thick red line is the average line profile. Right column: CoRoT light curves from 2011.

Table 7. Parameters used to calculate corotation radius (R_C) and magnetic field strength (B_*) of the three AA Tau-like stars that present observational evidence that the inner disk warp is located at the corotation radius.

Mon ID ^a	M_* ^b (M_\odot)	R_* ^c (R_\odot)	$\dot{M}_{H\alpha}$ ^d (M_\odot/yr)	P_{CoRoT_2011} ^e (days)	$P_{H\alpha}$ ^f (days)	R_C ^g (R_*)	B_* ^h (kG)
CSIMon-000250	1.63	1.35	1.44e-09	8.93	7.5/8.9	12.3	0.81
CSIMon-000660	1.86	1.4	1.45e-10	5.10	5.2	7.5	0.07
CSIMon-000811	0.91	1.97	6.75e-09	7.88	7.9/12.5*	8.2	0.44

Notes.

^(a) CSIMon is an internal identification of the CSI 2264 campaign. ^(b) Stellar mass obtained by Venuti et al. (2014). ^(c) Stellar radius obtained by Venuti et al. (2014). ^(d) Mass-accretion rates calculated with $H\alpha$ equivalent width. ^(e) Photometric period obtained from the 2011 CoRoT light curve. ^(f) Period obtained with the $H\alpha$ line from FLAMES spectra. ^(g) Calculated corotation radius. ^(h) Calculated stellar magnetic field. ^(*) This star shows only a faint hint of periodicity in $H\alpha$ at the photometric period (~ 7.9 days) that we used as the stellar rotational period.

lar variability, but not associated with a main physical process) showed no well-defined periodicity in their CoRoT light curves in 2008 and in 2011, as shown in Table 6. These stars are periodic in $H\alpha$, however, as seen in Figs. 14a, 14d, and 14g.

Mon-000667 has a period of 5.92 days measured by Lamm et al. (2004), which is very similar to our detected period (~ 5.9 days) and could indeed correspond to the stellar rotational period. In this case, the accreting gas is apparently organized, but the inner dust environment does not show a clear correlation with the gas structure.

We could not find any information about the rotational period of Mon-000996 in the literature, but it presents an $H\alpha$ period (~ 8.3 days) that is equal to the period found in the HeI 6678 Å line (see also Fig. 18o; we discuss this in Sect. 9). This is quite unexpected, since its light curve is dominated by random hot spot variability, which would suggest unstable accretion and not a globally organized accretion environment. This star also presents a similar periodicity (~ 8.1 days) in the *Spitzer* (IRAC) light curve at $3.6\ \mu\text{m}$ and $4.5\ \mu\text{m}$ (Cody et al. 2014). Recently, Blinova et al. (2015) divided the unstable accretion regime into two subclasses: ordered unstable (one or two unstable tongues) and chaotic unstable (several unstable tongues). A star in the ordered unstable accretion regime may retain some periodicity in its accretion bursts, as may be the case for Mon-000996, which presents only a low-power period detection in its light-curve periodogram at about 8.7 days.

Mon-000558 was classified by Cody et al. (2014), using the same CoRoT data, as quasi-periodic, since its light curve includes low-amplitude stochastic variability superposed on some slightly periodic signal. The possible photometric period is ~ 11.7 days. In the literature, it also presents a period of 0.88 days (Flaccomio et al. 2006), which is very different from the $H\alpha$ and the photometric period from our survey, however. We show in the next subsection that the $H\alpha$ period of ~ 10.5 days is also seen in the HeI line (see Table 6), which may indicate that it corresponds to the stellar rotation period. This star had an accretion burst CoRoT light curve in 2008, while in 2011 it has an irregular, possibly hot-spot light curve. This is another system that is a candidate to be in the ordered unstable regime described by Blinova et al. (2015).

8.3. $H\alpha$ periodicity in stars not observed by CoRoT in 2011

Two stars that show $H\alpha$ line periodicity were not observed by CoRoT in 2011. The star Mon-001033, Fig. 15a, although not observed by CoRoT in 2011, shows a possible period of 14 days measured in 2011 with the *Spitzer* (IRAC) light curve in the CSI2264 campaign (Cody et al. 2014). This star was observed by CoRoT in 2008, and its light curve was classified as spot-like, with a period of 14.15 days, which agrees with the IRAC period, but is more than twice that obtained with the $H\alpha$ line (~ 6.30 days). The periodic region in $H\alpha$ corresponds to a narrow velocity range, where a redshifted absorption is present in the spectrum.

The other star that presented a periodicity in $H\alpha$, but was not observed by CoRoT, is Mon-000239. This star does not have any period information in the literature and is not periodic with *Spitzer* photometry. The detected period in $H\alpha$ occurs in a very limited profile region associated with a small redshifted absorption feature, like the one observed in Mon-001033.

8.4. $H\alpha$ periodicity in spot-like stars

Eight CTTSs classified as spot-like with the 2011 CoRoT light curves were observed with FLAMES. However, despite being periodic in the photometry, none of them showed any periodicity in the $H\alpha$ line. Two examples are presented in Fig. 16. The pho-

tometric periodicity of spot-like stars is mostly due to cold spots on the photosphere, while the $H\alpha$ line is mainly formed in the accretion funnel. Results from spectropolarimetry have shown that the main hot and cold spots tend to coincide in accreting stars (Donati et al. 2010, 2011a,b), and we would therefore expect the cold spot and the main accretion funnel, which ends in the hot spot, to present the same periodicity. At the same time, the $H\alpha$ line profiles of spot-like systems tend to be weak and may therefore have a significant chromospheric contribution. In some spot-like systems, the lack of $H\alpha$ line periodicity could then be due to a rather uniform chromospheric emission contributing significantly to the profile, which would dilute the $H\alpha$ modulation from the accretion funnel.

9. Periodograms of the HeI 6678 Å emission line

The HeI 6678 Å singlet line is often found in emission in stars with a moderate to high accretion rate (Muzerolle et al. 1998; Beristain et al. 2001a; Luhman et al. 2003). Like the HeI 5876 Å triplet line, it may present a narrow (NC) and a broad (BC) component, with different kinematic characteristics. In the spectra of CTTSs, the NC is found to be slightly redshifted and circularly polarized and is interpreted to arise from gas in the post-shock region near the stellar surface (Beristain et al. 2001b; Edwards et al. 2003). The BC is more complex. It can be found to be redshifted, but is most commonly observed blueshifted in CTTSs. The current interpretation is that it may come from the accretion funnel or the base of a hot accretion-powered stellar wind (Beristain et al. 2001b; Edwards et al. 2006).

Depending on the star-disk inclination with respect to our line of sight, the hot spot may be hidden by the inner disk and remain invisible most of the time. In that case, we would not expect to see the HeI line in emission, even at high accretion rates. This is probably the case of the AA Tau-like system Mon-000660, which is seen at high inclination ($79^\circ \pm 11^\circ$, Fonseca et al. 2015) and does not present UV excess or HeI 6678 Å in emission, despite being actively accreting, as shown by its extended $H\alpha$ emission profile.

The HeI NC is formed close to the stellar surface, therefore its periodicity, whenever present, should correspond closely to the stellar rotation period. We expect to detect periodic variability if accretion is in a stable regime, which creates a main accretion funnel and consequently a main hot spot in each hemisphere.

We found that 24 of the 58 CTTSs observed with FLAMES clearly presented the HeI 6678 Å line in emission. Another set of 11 CTTSs also show HeI in emission, but the S/N is too low in the line to allow a reliable analysis of line profile variability. According to Beristain et al. (2001b), the HeI NC is characterized by line widths smaller than 50 km/s. In our sample, the width of the mean HeI 6678 Å line profile ranged from 29 to 47 km/s, depending on the target, with a mean value of 39.3 km/s. Therefore, in our sample, all of the stars that showed HeI 6678 Å in emission only presented an NC. Close to the HeI 6678 Å line, there is a photospheric absorption FeI line (at 6677 Å). We used residual spectra to calculate the HeI 6678 Å line equivalent widths because of this line. The FeI 6677 Å line was subtracted from these spectra, using as template the spectrum of a WTTS of the same spectral type of each star.

We calculated the HeI line periodograms as was done for the $H\alpha$ line (see Sect. 8). The periodograms of the HeI lines are shown in Figs. 17 and 18. Of the 24 CTTSs with clear HeI emission, 12 stars showed no periodicity in this line, and they were

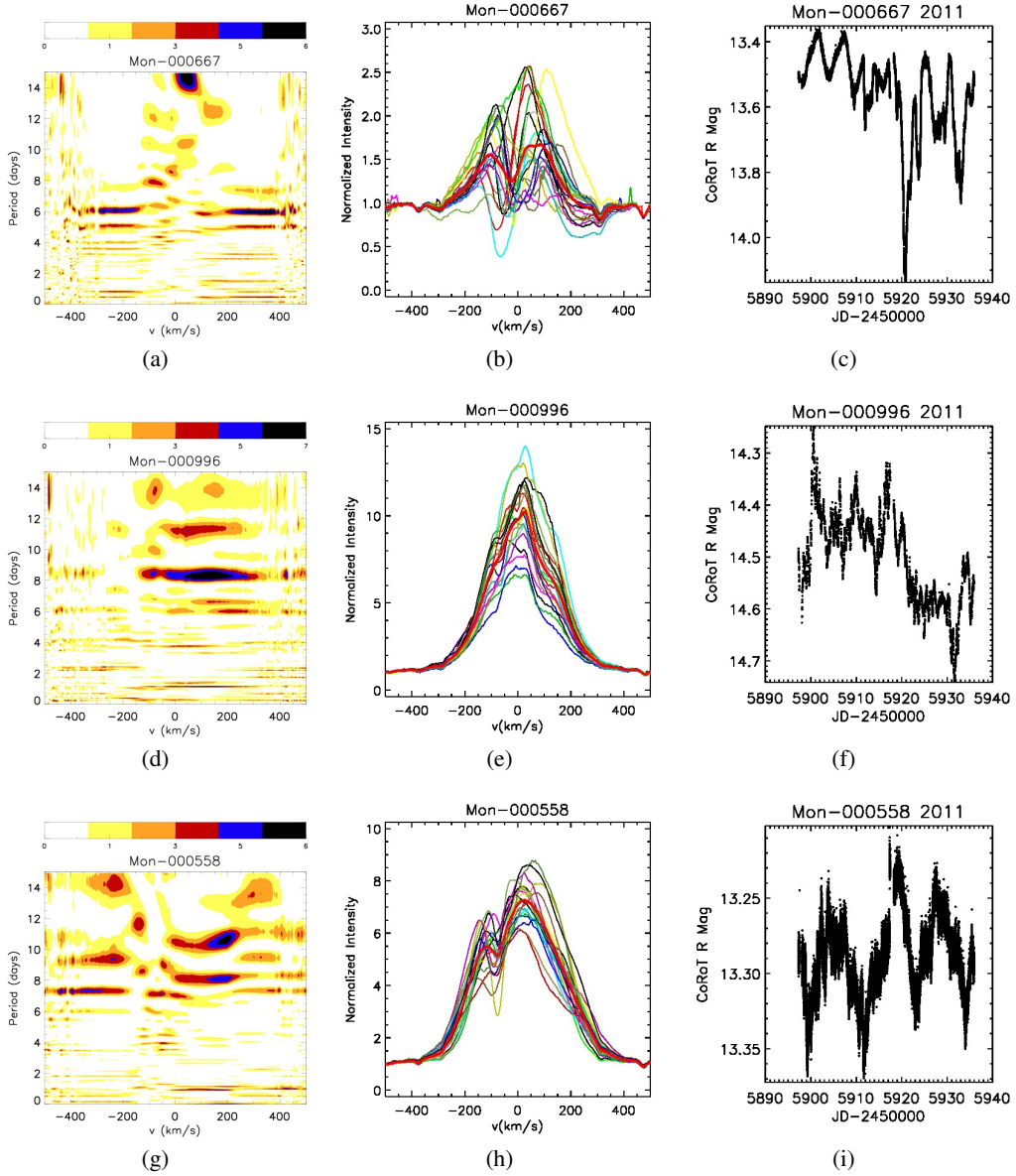


Fig. 14. Periodic stars in the $H\alpha$ line that are not periodic in the CoRoT photometry. Left column: Bidimensional periodograms of the $H\alpha$ line. The color code represents the power of periodogram, varying from zero (white) to the maximum power intensity (black). Middle column: $H\alpha$ line profiles. Different colors correspond to different nights of observation, and the thick red line is the average line profile. Right column: CoRoT light curves from the 2011 campaign.

also non-periodic in the CoRoT photometry. The non-periodicity of half of the HeI emission stars may indicate the intermittent formation of several short-lived hot spots near the stellar surface, instead of one well-organized hot spot in each hemisphere.

Of the 12 systems that showed a periodicity in the HeI line, two presented more than one period in this line (as seen in Table 6 and Figs. 18e and 18i), which may be because of the formation of several long-lived (compared to the time span of our observations) hot spots at different latitudes on the stellar surface, rather than a main hot spot on each hemisphere. In the next subsections, we present the analysis of the HeI line periodicity compared to the CoRoT light-curve morphology discussed in Sect. 4.

9.1. HeI line in AA Tau like stars

AA Tau-like stars are seen at high inclination with respect to our line of sight, and the inner disk is expected to hide part of the stellar photosphere as the system rotates. Depending on the system geometry, the hot spot, and consequently the region where the HeI NC forms, may also be hidden in these systems. Only three of eight AA Tau-like stars observed with FLAMES showed the HeI line in emission, and these three systems presented a periodicity in this line. The HeI line periodograms of Mon-000250, Mon-001054, and Mon-000811 are shown in Fig. 17 and the measured periods are presented in Table 6.

Mon-000250 shows the same periodicity in HeI and $H\alpha$ lines (Figs. 17a and 13d), and also presents the same period in the CoRoT light curve, which confirms that the structure responsi-

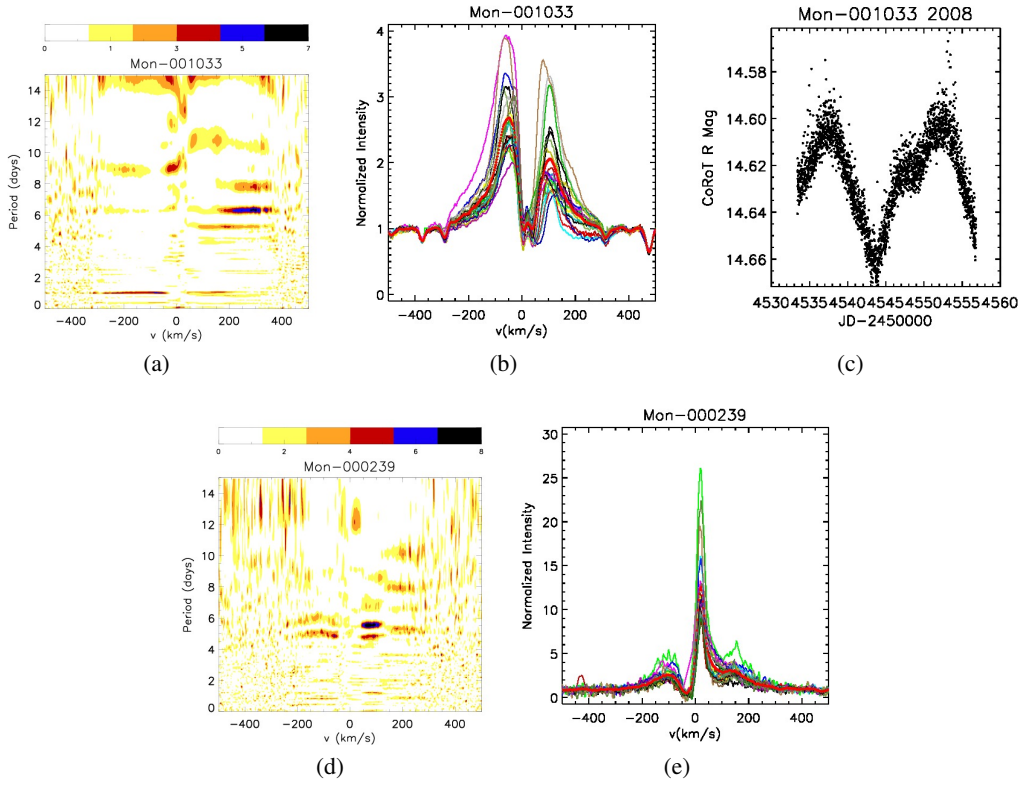


Fig. 15. Periodic stars in the $H\alpha$ line that were not observed by CoRoT in 2011. Left column: Bidimensional periodograms of the $H\alpha$ line. The color code represents the power of the periodogram, varying from zero (white) to the maximum power intensity (black). Middle column: $H\alpha$ line profiles. Different colors correspond to different nights of observation, and the thick red line is the average line profile. Right column: CoRoT light curve from 2008, when available.

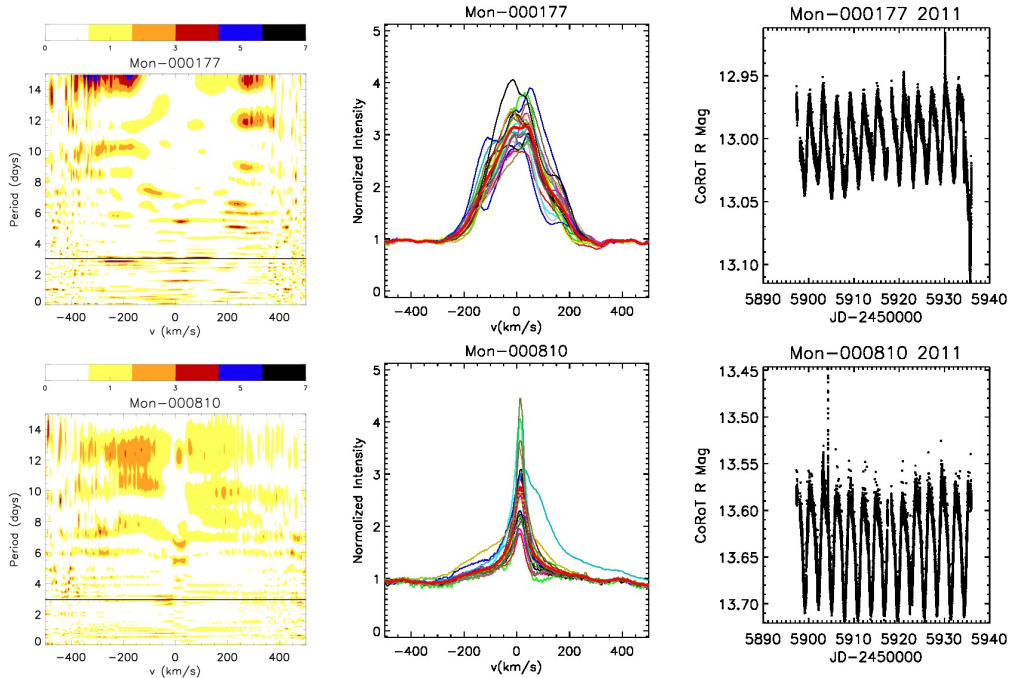


Fig. 16. Spectroscopic and photometric variability of spot-like systems. Left column: Bidimensional periodogram of the $H\alpha$ line of two spot-like systems. The color code represents the power of periodogram, varying from zero (white) to the maximum power intensity (black). Black lines correspond to the photometric period of the stellar light curve observed with CoRoT in 2011. Middle column: $H\alpha$ line profiles. Different colors correspond to different nights of observation, and the thick red line is the average line profile. Right column: CoRoT light curve from 2011. None of the spot-like systems observed with FLAMES showed any periodicity in the $H\alpha$ line.

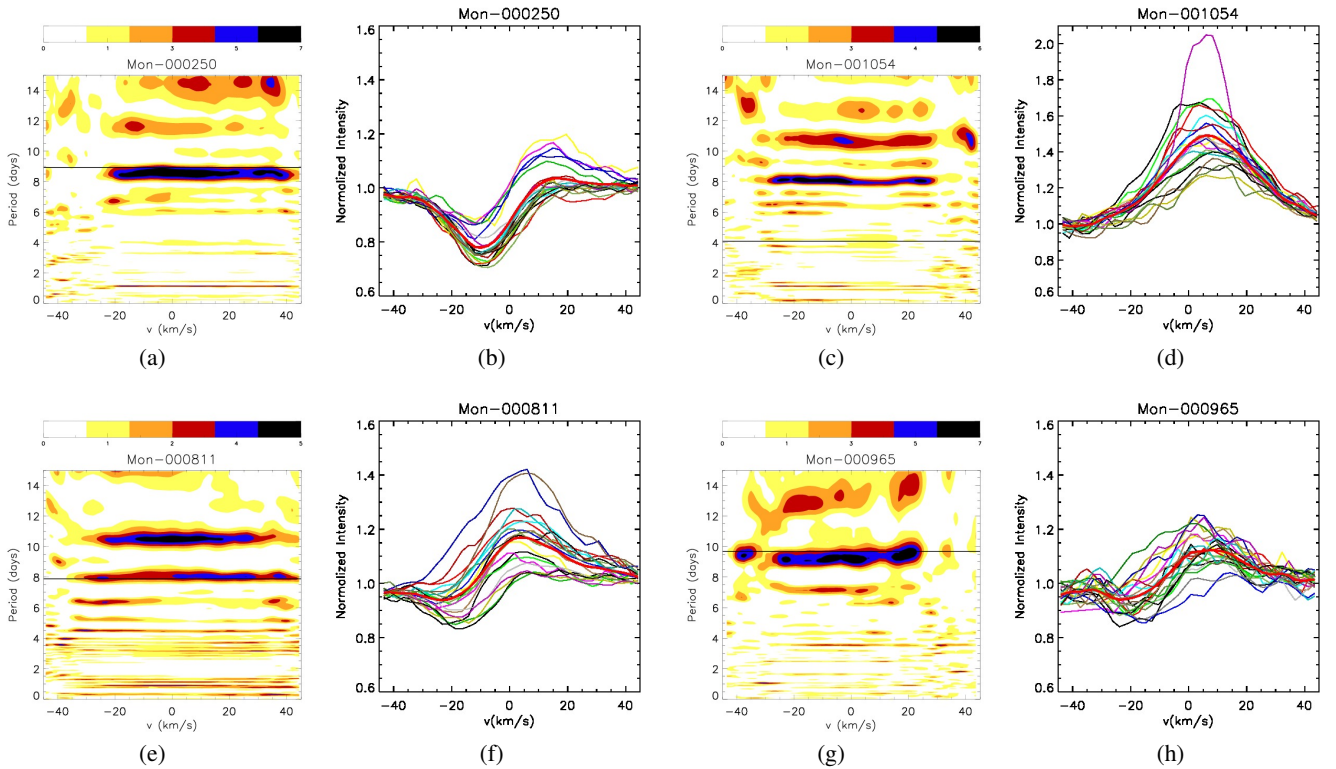


Fig. 17. Periodic stars in the HeI 6678 Å that also showed a periodicity in the CoRoT light curves. Bidimensional periodograms of the HeI line (first and third columns). The color code represents the power of the periodogram, varying from zero (white) to the maximum power intensity (black). The black horizontal lines correspond to the period of the 2011 CoRoT light curve. The second and fourth columns present the HeI 6678 Å lines used to calculate the periodograms. Different colors correspond to different nights of observation, and the thick red line is the average line profile.

ble for the stellar occultation is located close to the co-rotation radius of the star-disk system.

Mon-001054 (Fig. 17c) shows a HeI period of ~ 8.1 days, that is, twice the CoRoT photometric period from 2011. The photometric period, calculated with the modified Scargle periodogram, as explained in Sect. 4, presents a low detection power. Using a different period search method, such as the auto-correlation function (Cody et al. 2014; McQuillan et al. 2013), we find a ~ 8.2 day period in the CoRoT light curve, but the detection significance is again very low. From the literature, Mon-001054 has a photometric period of ~ 7.8 days (Lamm et al. 2004), which agrees with our HeI period and could correspond to the stellar rotation period.

Mon-000811 (Fig. 17e) is periodic in HeI (~ 10.5 , higher power and ~ 8 days lower power) and H α (~ 12.5 days) (Figs. 17e, 13g) and shows periodicity in the CoRoT light curve (~ 7.88 days). However, these periods are different from each other. As discussed above, this star is classified as AA Tau-like, and we would therefore expect accretion to occur in a stable regime, if the inner disk warp is associated with the base of the accretion column, and forming a major hot spot in each hemisphere at the top of the accretion column. One possible scenario to explain this complex system is that the HeI line eight-day period corresponds to the stellar rotation period, which is close to the photometric period, and therefore the inner disk warp that causes the photometric variability is located close to the co-rotation radius. The H α ~ 12.5 -day period is observed in the blue wing of the emission profiles and could then correspond to emission or absorption from a wind located outside the corotation radius.

9.2. HeI line periodicity in spot-like stars

Because of the high stability of the spot-like light curves on the timescale of our observations and the low mass-accretion rates of these systems, we initially assumed that large cold spots were the main cause of the observed photometric variability of spot-like systems. If, instead, hot spots were causing the photometric variability in the HeI line. We observed eight spot-like systems with FLAMES, and only one, Mon-000965, has the HeI line in emission, as seen in Table 6. The HeI periodogram of this star is shown in Fig. 17g, and it presents a clear periodicity that coincides with the period obtained with the CoRoT photometry. Mon-000965 is not clearly periodic in H α (Sect. 8.4), but a faint periodic signal (low power in the periodogram) is seen at the photometric period. The fact that this star has the HeI NC line in emission indicates that the hot spot is prominent, which suggests that its light-curve variability might be dominated by a stable hot spot instead of a cold spot, as initially assumed during our 2011 campaign.

9.3. Periodic stars in the HeI line that are not periodic in the CoRoT photometry or were not observed by CoRoT in 2011

Half of the 24 stars that showed HeI in emission presented periodicity in this line, but only 4 (Sect. 9.1 and 9.2) were also periodic in the CoRoT photometry, as seen in Fig. 17. The other 8 stars that showed a periodicity in the HeI line were not found to

be periodic in the CoRoT light curves of 2011 (6 stars) or were not observed with CoRoT in 2011 (2 stars), as seen in Fig. 18.

All of the accretion burst systems observed by FLAMES (five in total) are included in the stars that showed HeI in emission, which is reasonable, since they all presented high mass-accretion rates and had light curves dominated by hot spot variability (Stauffer et al. 2014). Three of these five stars (Mon-000996, Mon-001022 and Mon-000945) presented a periodicity in the HeI line, despite showing no periodic signal in the CoRoT photometry. Mon-000996 (18o) also presented similar periodicities in both the HeI and H α lines, as shown in 14d.

10. Stable and unstable accretion

CTTSs are photometrically variable on different timescales, from seconds to even decades (Rucinski et al. 2008), depending on the various physical phenomena that affect the stellar and circumstellar environment. Variable accretion is one of the main sources of variability in this evolutionary phase. As discussed by Kurosawa & Romanova (2013), accretion can occur in stable and unstable regimes. The unstable regime may be triggered by the Rayleigh-Taylor instability, which takes place in the inner disk region. This type of variability produces non-periodic light curves that are dominated by accretion bursts, as observed in some stars in NGC 2264 (see Stauffer et al. 2014). This variability also produces detectable spectral features in emission lines, such as H β , H γ , and Pa β (Kurosawa & Romanova 2013).

According to theoretical predictions, stars in a stable accretion regime will present redshifted absorption in just a few rotational phases, when the main hot spot is seen projected through the accretion funnel in our line of sight. In this situation, photons emitted by the hot spot will be absorbed by the high-velocity gas in the accretion funnel, causing the observed redshifted absorption components. In the unstable accretion regime, redshifted absorption may be seen at any rotational phase because of the large number of accretion funnels, and consequently, hot spots on the stellar surface. The accretion burst stars are all expected to be in the unstable accretion regime. Unfortunately, only five accretion burst systems were included in our sample of stars observed with FLAMES, and none of them showed redshifted absorption in H α . Their H α line profiles are dominated by emission due to accretion (Reipurth type I profile) that typically does not present redshifted absorption (see Fig. 12). To investigate the occurrence of redshifted absorption in the emission lines of accretion burst systems, we need to analyze higher order Balmer lines, as suggested by Kurosawa & Romanova (2013), or the HeI (10830 Å) line, which often shows both redshifted and blueshifted absorption in CTTS spectra, as discussed by Edwards et al. (2006) and Cauley & Johns-Krull (2014).

In the simulations by Kurosawa & Romanova (2013), the redshifted absorption components are not visible in the H α line either because its emission is very intense and hides the shallow absorption. Redshifted absorption is most commonly seen observationally in weaker Balmer emission lines such as H β and H γ . We do not have the higher Balmer lines in our spectra, but ten stars show a clear redshifted absorption component in the H α line (marked in Col. 8 of Table 6). Despite the small number of targets, we tried to verify how the redshifted absorption component varies with stellar rotational phase and compare our results with the prediction of stable and unstable accretion simulations.

Of our ten selected targets, only Mon-000824 is possibly in the unstable accretion regime, where the redshifted absorption is present in the line profile at all rotational phases. This star was classified as AA Tau-like in 2008, but was not observed by

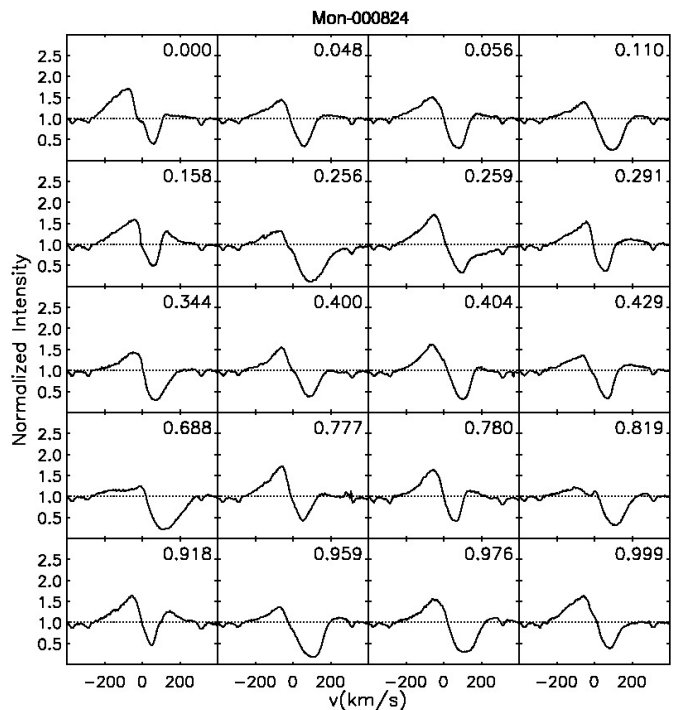


Fig. 19. H α line of Mon-000824 as a function of rotational phase, indicated in each plot. This star was not observed by CoRoT in 2011, and we used the photometric period (7.05 days) obtained in 2008, when the star presented an AA Tau-like light curve, to calculate the rotational phases. This star is a candidate to be in the unstable accretion regime in 2011.

CoRoT in 2011 (see Fig. 19), which means that in principle we would not know its photometric behavior when the spectroscopic data were obtained. As seen in Sect. 4, CTTSs are highly variable and in a few years may change the morphology of their light curve from AA Tau to non-periodic and vice versa. Although Mon-000824 was not observed with CoRoT in 2011, during the CSI campaign about 900 epochs of I-band photometry were obtained from November 2011 to March 2012 of the central region of NGC 2264, including Mon-000824, with the US Naval 40" telescope. As discussed by McGinnis et al. (2015), the simultaneous I-band and CoRoT photometry typically match very well. We therefore inspected the I-band light curve of Mon-000824 in 2011 and found that it was indeed not periodic, implying that this star probably changed from a stable to an unstable accretion regime from 2008 to 2011.

The other nine selected stars (two spot-like, five AA Tau-like, one aperiodic extinction variables and one not observed by CoRoT in 2011) are apparently in a stable accretion regime, showing redshifted absorptions in only a few rotational phases. In Fig. 20, we show the spectra of Mon-000296 as an example.

The predictions that stable and unstable accretion regimes present a different rotational phase distribution of redshifted absorption components are based on the theoretical line profiles computed by Kurosawa & Romanova (2013) for a system with an inclination of 60° with respect to the line of sight. However, in systems with lower inclinations, hot spots will always be in view (Kurosawa et al. 2008), hence, even in a stable accretion regime the redshifted absorption may be present in the line profile at all rotational phases. This is, however, not the case of Mon-000824 (Fig. 19), since its inclination with respect to our line of sight is $72^\circ \pm 5^\circ$ (McGinnis et al. 2015).

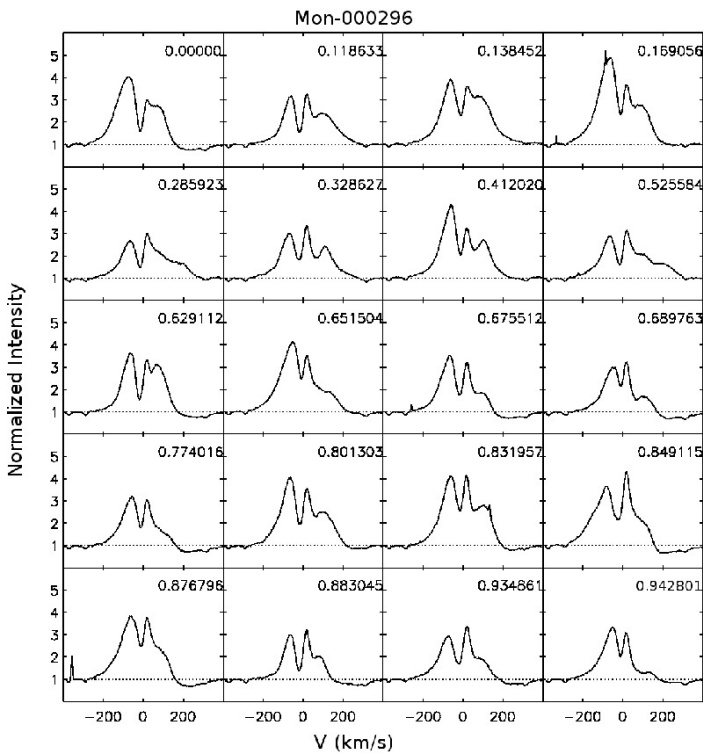


Fig. 20. $H\alpha$ line of Mon-000296 as a function of rotational phase, indicated in each plot. The central peak is the nebular line that was not entirely removed. This star presents an AA Tau-like light curve with a 3.91 day period and is a candidate to be in the stable accretion regime in 2011.

We would expect stars in a stable accretion regime to show periodic light curves and stars in an unstable accretion regime to show non-periodic light curves (Kurosawa & Romanova 2013; Kulkarni & Romanova 2008, 2009). This is because the stable accretion regime generates an organized circumstellar environment that shows periodicity as the star-disk system rotates. Of the nine stars we classified as being in a stable regime, using this criterion of redshifted absorption, only two did not present periodic light curves, as seen in Table 6. Instead their light curves were classified as aperiodic extinction variables. The stable accretion regime classification therefore agrees with the observation of periodicity in the CoRoT light curves for most stars with redshifted absorption in just a few rotational phases.

In the stable accretion regime, the variability of the redshifted absorption is expected to be periodic. Of the nine stars we classified as being in a stable regime, five are periodic in the $H\alpha$ line, agreeing with the theoretical predictions of Kurosawa & Romanova (2013). This means that only about half of the stars we classified as being in a stable accretion regime are periodic in the $H\alpha$ line. The only star in the unstable accretion regime (Fig. 19) is also not periodic in the $H\alpha$ line, as predicted by Kurosawa & Romanova (2013).

The classification of a stable accretion regime based on the presence of redshifted absorption at well-defined rotational phases agrees only sometimes with the type of observed variability in the CoRoT light curves. Neither is a star that shows redshifted absorption at all rotational phases necessarily accreting in the unstable regime. Other factors, such as the inclination of the system, may influence the presence of the redshifted absorption in the Balmer lines. Moreover, we must keep in mind that the $H\alpha$ line is not the best choice for this type of analysis,

since other lines, such as $H\beta$, $H\gamma$, and $Pa\beta$, are weaker, and the redshifted absorption is more commonly visible in the line profiles.

11. Correlation matrices

The $H\alpha$ emission line can be formed in several different regions, in the accretion funnel, the chromosphere, and/or the wind. The analysis of the correlation of different parts of the $H\alpha$ line profile can help us investigate if the line comes from different regions and if these regions are correlated.

One method of checking the correlation across a line profile is to calculate correlation matrices. We divided each $H\alpha$ profile into small velocity intervals of 1.5 km/s and calculated the linear correlation coefficient, $r(i, j)$, of the line intensity at each velocity interval i with each velocity interval j , as described by Johns & Basri (1995a). The correlation coefficient ranges from -1 to 1 , 1 corresponding to a perfect correlation, 0 to no correlation, and -1 to a perfect anticorrelation. When $i = j$, $r(i, j) = 1$, and for all values of i and j , $r(i, j) = r(j, i)$, implying that the matrix is symmetrical relative to the diagonal. We present the result as a color-map plot of the correlation coefficients, which is useful to visually identify regions of the profile that are correlated or anticorrelated. This has been used in the literature to analyze correlations across the $H\alpha$ line and other lines such as $H\beta$ (Johns & Basri 1995b; Oliveira et al. 2000; Alencar & Batalha 2002; Kurosawa et al. 2005).

All of the 58 CTTs that have FLAMES spectra present some correlation signal of the red wing with itself. Some stars show this correlation just in the redshifted absorption position and others just in the redshifted emission. We find that $\sim 74\%$ of the CTTs show a very good correlation across the entire $H\alpha$ red wing, which then varies coherently. Almost all the CTTs observed by FLAMES also exhibited some correlation of the blue wing with itself, $\sim 74\%$ presenting a substantial correlation. The blue wing of $H\alpha$ also varies coherently. This shows that the variability in each wing of the $H\alpha$ profile is coherent, which indicates that each line wing (red or blue) is formed in a region dominated by a given physical process.

We find that $\sim 34\%$ of the CTTs observed with FLAMES show no sign of correlation between the red and the blue wings, implying that they vary independently in those systems. At the same time, $\sim 66\%$ CTTs show some correlation of the red wing with the blue wing and among these, $\sim 55\%$ show substantial correlation across the entire wings, while $\sim 45\%$ show correlations that occur only in some specific velocity range.

Only 7 of the 58 CTTs observed with FLAMES present anticorrelated variations in the $H\alpha$ line profile. The anticorrelation seen in 4 of these 6 stars is associated with a blue- or redshifted absorption that varies in antiphase with the rest of the profile. The other three stars present an anticorrelation associated with a blueshifted emission and the other profile parts.

Overall, the $H\alpha$ line profiles present variations that cannot be explained by continuum variability alone that is due, for example, to hot spots. If excess continuum emission from hot spots were the main cause of emission line variability, the entire profile would be correlated, and the $H\alpha$ line would not vary in shape, but only in intensity. Other factors such as wind emission or absorption, accretion variability, and non-symmetrically distributed circumstellar material must influence the emission line variability, often simultaneously, since many stars do not present a very good correlation across the entire $H\alpha$ line profile. It is possible, however, that in some cases the $H\alpha$ line may be formed mainly in one specific region, like the wind or the accretion column. We

would then expect the line profile to be dominated by the same physical process and the variability of the entire line profile to be correlated.

Figures 21 and 22 show examples of correlation matrices for some CTTSs, together with their observed $H\alpha$ line profiles. These figures are representative of the different types of correlation matrices we obtained. In these plots, the correlation coefficients are represented by colors ranging from black ($r = -1$, maximum anticorrelation) to light blue ($r = 0$, no correlation) and to orange ($r = 1$, maximum correlation). The correlation matrices and $H\alpha$ line profiles of all the CTTSs in our sample observed with FLAMES are presented in the Appendix.

Figure 21a,b shows that for Mon-000457 the red wing of $H\alpha$ correlates well with itself in the velocity range of $50 \text{ km/s} < v < 350 \text{ km/s}$, and the blue wing shows a good correlation with itself at $-350 \text{ km/s} < v < -75 \text{ km/s}$. We can also see a region of correlated variability in the blue wing at $-100 \text{ km/s} < v < 0 \text{ km/s}$, which corresponds to the blueshifted absorption from a wind that varies quite independently of the rest of the profile. The blue wing is anticorrelated with the red wing for velocities in the range of ~ -100 to $\sim -350 \text{ km/s}$ and ~ 0 to $\sim 350 \text{ km/s}$. The line profiles show that these regions correspond to the blue and red emissions that vary in antiphase with each other. This indicates a strong influence of different physical processes in each $H\alpha$ profile wing, the red wing is probably dominated by accretion and the blue wing by the wind. The accretion process and the wind may contribute to the entire profile, but can have a stronger contribution in one particular velocity range, as seen for example in theoretical line profiles calculated by Kurosawa et al. (2006) and Lima et al. (2010), which include both the wind and accretion contributions. In the case of Mon-000457, if the blue wing is mostly influenced by the wind and accretion is probably the main process acting on the red wing, the anticorrelation between the two wings could be explained as being due to rotational modulation of a CTTS with an inclined magnetosphere, as also observed in SU Aur (Johns & Basri 1994). When the main accretion funnel faces the observer, accretion is strong and ejection is low, and half a rotation cycle later, the opposite occurs. In an ideal case, these variations should be periodic, but the $H\alpha$ line variability of this star does not show very clear signs of periodicity.

Figure 21c shows a strong correlation of the red wing with itself and with the blue wing of the $H\alpha$ profile at high velocities ($|v| > 200 \text{ km/s}$) for Mon-001022. At the same time, the strong blueshifted absorption ($-200 \text{ km/s} < v < 0 \text{ km/s}$) is anticorrelated with the blue and red emission regions of $H\alpha$. This feature is due to photons from the accretion columns and a hot spot absorbed by the outflowing disk wind material in our line of sight. Stars that present very strong blueshifted absorption in $H\alpha$ normally present emission profiles dominated by the wind, as can be seen in the theoretical profiles calculated by Kurosawa et al. (2006) and Lima et al. (2010). When the emission due to the wind increases, photons are even more strongly absorbed by the wind, increasing the depth of the blueshifted absorption. This causes the blueshifted absorption to become anticorrelated with the rest of the emission line.

Figure 22a shows the correlation matrix and the $H\alpha$ line profiles of Mon-001033. The blue and red wings of the $H\alpha$ profile correlate well with themselves, but show no correlation or anticorrelation with each other. The emission component is quite variable, not very intense, and suffers strong influence from absorption in the blue and red wings. Blueshifted absorption is associated with winds and redshifted absorption with the accretion funnel. The combination of faint emission and strong absorption

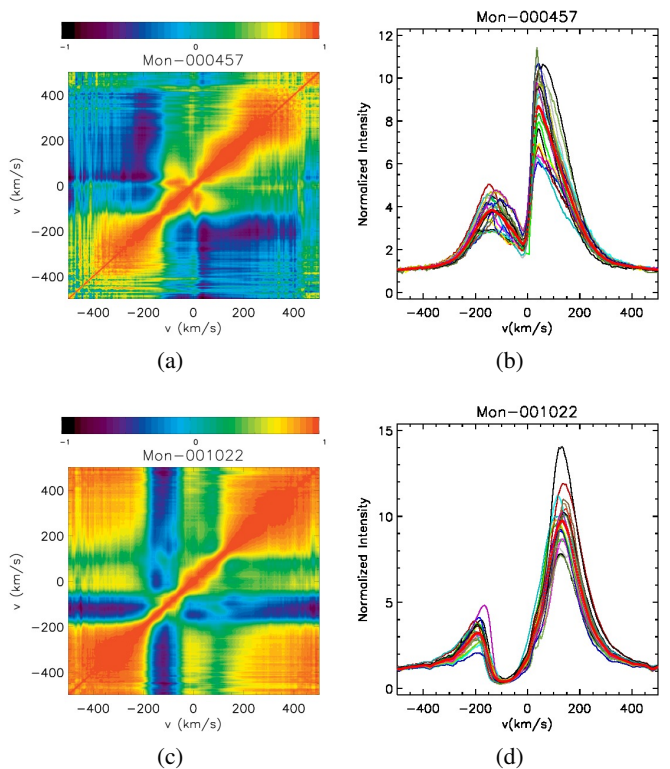


Fig. 21. Examples of correlation matrices (left) of the $H\alpha$ line of two CTTSs and the corresponding line profiles (right). In panels (a) and (c), the color range corresponds to the value of the linear correlation coefficient between the different velocity bins of the $H\alpha$ line profiles. Perfect anticorrelation corresponds to -1 (black), no correlation to 0 (light blue), and a perfect correlation to 1 (orange). In panels (b) and (d), different colors correspond to spectra observed in different nights, and the thick red line is the average line profile. The correlation matrices and $H\alpha$ line profiles of all the CTTSs in our sample observed with FLAMES are presented in the Appendix.

that probably comes from different physical processes created a variability pattern where the variations of one wing are not correlated with the other wing.

Theoretical correlation matrices are rare in the literature. In Alencar et al. (2012), $H\alpha$ correlation matrices were calculated from theoretical line profiles that included only the magnetospheric contribution. Their theoretical correlation matrices showed a good correlation of the entire $H\alpha$ line profile, but outflows were not taken into account. Our observed CTTSs include stars such as Mon-000945, whose $H\alpha$ emission line profiles show no hint of blueshifted absorption and should be dominated by accretion. Figure 22c,d shows the $H\alpha$ profiles of Mon-000945 and its corresponding correlation matrix, which indeed is well correlated across the entire profile, as predicted theoretically by magnetospheric accretion models. However, the $H\alpha$ profile of most CTTSs cannot be explained by magnetospheric accretion alone, and it would be very interesting to be able to compare the observed correlation matrices with theoretical matrices calculated from profiles that include both accretion and outflows.

Veiling variations would also produce a correlation across the entire line profile, as observed in the $H\alpha$ line of Mon-000945. However, the $H\alpha$ line profile presents changes in its morphology, not only in its intensity (see Fig. 22d), as would be expected for variations that are only due to the extra veiling continuum. The type of correlated variability and $H\alpha$ profile morphology ob-

served in Mon-000945 is also seen in the CTTSs T Tau (Johns & Basri 1995b) and TW Hya (Alencar & Batalha 2002), for which it has also been suggested that the $H\alpha$ line is mostly formed in the accretion columns.

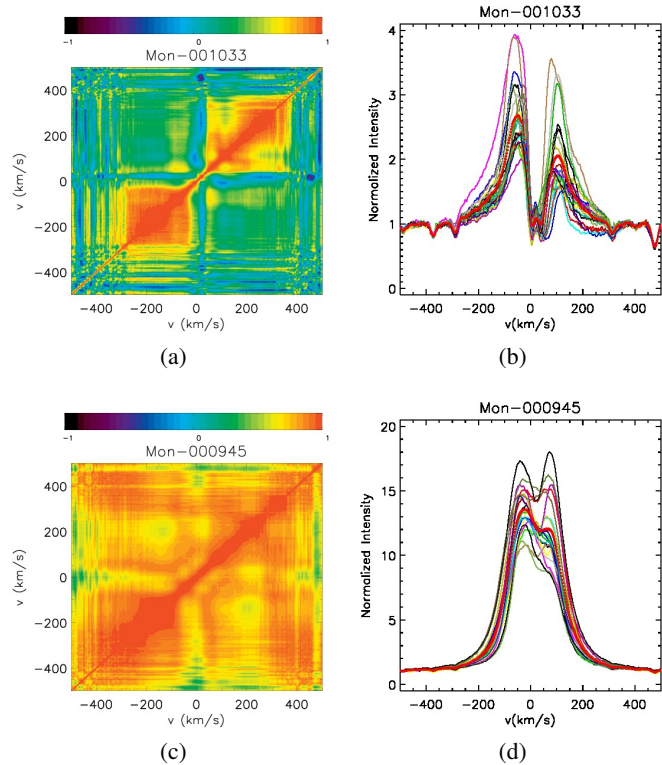


Fig. 22. Examples of correlation matrices (left) of the $H\alpha$ line of two CTTSs and the corresponding line profiles (right). The color code is the same as in Fig. 21.

The analysis of the correlation matrices shows that the $H\alpha$ line variability can be associated with different physical processes. The variability of the red wing often does not affect the variability of the blue wing. This is confirmed by the lack of correlation of the blue wing with the red wing, seen in $\sim 34\%$ of the $H\alpha$ correlation matrices. This lack of correlation disagrees with theoretical models that only include the magnetospheric accretion contribution to the emission line profile. It would be very interesting to compare observational correlation matrices to matrices calculated from hybrid magnetosphere and wind models, such as those of Kurosawa et al. (2006, 2011), and determine which circumstellar environment would be able to reproduce the observational matrices. At the same time, the red wing is almost always well correlated with itself, as is the blue wing with itself, indicating that the variability of each wing is dominated by the same physical phenomenon.

12. Interesting objects

Some objects are interesting enough to be analyzed individually in future work. We found three spectroscopic binaries with the FLAMES data. The CTTS Mon-000448 is a double-line spectroscopic binary, while the WTTS Mon-000497 and the CTTS Mon-000804 are single-line spectroscopic binaries. These stars do not present eclipses in the CoRoT light curves, however.

The AA Tau-like star Mon-00811 is a CTTS that has different periods in different accretion and circumstellar features. One

possible interpretation is that the different periods come from different regions of the star-disk system. It has a photometric period (~ 7.9 days) due to occultation of the star by the inner disk, a stellar rotation period (~ 8 days) obtained from the HeI line periodogram, a 10.5-day period from the HeI blueshifted emission, and a period of ~ 13 days in the $H\alpha$ line blue wing that we associate with a disk wind.

Some WTTSs have strong IR excesses, but do not show a clear sign of accretion (Mon-001157, Mon-000434, Mon-000279, Mon-000753, and Mon-000271). For some unknown reason, accretion has been shut off or is at a very low level, despite the available material in their inner disks. It would be interesting to reobserve these systems to verify whether accretion features reappear in the future, or if it has indeed come to an end.

13. Conclusions

We investigated accretion in a group of classical T Tauri stars that belong to the young cluster NGC 2264, using observational data obtained in the *Coordinated Synoptic Investigation of NGC 2264* campaign. The main results of this work are listed below.

1. The light curves observed by CoRoT were morphologically classified as spot-like, AA-Tau-like, or non-periodic. Of the non-periodic light curves, some are due to accretion bursts, others to circumstellar disk obscuration, but most non-periodic light curves are very complex and could not be associated with a major physical phenomenon. In the 2011 campaign, we found $\sim 13\%$ spot-like, $\sim 12\%$ AA Tau-like, and $\sim 71\%$ non-periodic systems. Of the non-periodic ones, $\sim 19\%$ were associated with accretion bursts, $\sim 13\%$ with occultation by circumstellar dust, and $\sim 68\%$ presented variability of unknown origin.
2. Of the CTTSs observed by CoRoT, $\sim 43\%$ and $\sim 29\%$ showed periodic photometric variability in 2008 and 2011, respectively. The number of periodic stars did not change significantly between the two runs, but a larger number of non-periodic stars were included in the 2011 campaign.
3. Of the 84 stars that were observed with the CoRoT in the two different epochs (2008 and 2011), $\sim 30\%$ showed substantial variability in their light-curve morphology, changing to a different category in our light-curve classification scheme. These changes show how dynamic the CTTS circumstellar environment is in only a few years.
4. When UV excesses are not available, mass-accretion rates can be obtained with good results from the $H\alpha$ flux using the currently available calibrations from the literature.
5. Most of the CTTSs we observed showed no periodicity in the $H\alpha$ line. Only eight stars in our sample of 58 CTTSs observed with FLAMES were periodic in $H\alpha$.
6. The HeI 6678 Å narrow component line variability can provide the rotation period of a CTTS when the star is in a stable accretion regime, since in that case a major hot spot is expected to form in each stellar hemisphere. We found that 24 of the 58 stars observed by FLAMES had this line in emission. Of these, 12 were periodic in the HeI line, and 4 were also periodic photometrically.
7. None of the photometrically periodic spot-like systems that were observed spectroscopically presented a periodicity in $H\alpha$, while spectropolarimetry results show that hot and cold spots tend to be coincident in CTTSs, and we might expect to observe the same periodicity in the cold spot and accretion funnel diagnostics. Spot-like systems tend to present low mass-accretion rates, and the lack of periodicity in the $H\alpha$

line variability of spot-like systems could be due to chromospheric emission contributing significantly to the emission profile in these systems, which would dilute the $H\alpha$ modulation from the spot.

8. We analyzed which CTTs were in stable or unstable accretion regimes. Kurosawa & Romanova (2013) suggested that CTTs in a stable accretion regime should present redshifted absorption components in emission line profiles only in a few rotational phases, when photons from the hot spot are seen in our line of sight projected against the main accretion column. Systems in unstable accretion will produce random accretion tongues and should present redshifted accretion components at any rotational phase. We analyzed the ten CTTs that showed redshifted absorption components in $H\alpha$ and for which we had some information about the rotational period. Of these, nine CTTs fulfilled the stable accretion criteria (five stars were AA Tau-like, two stars were spot-like, one was non-periodic, and one was not observed in 2011 by CoRoT), and in almost all the systems accretion in a stable regime agrees with the type of variability observed in the CoRoT light curves. Only one star of the ten selected CTTs was apparently in the unstable accretion regime, presenting redshifted absorption at all rotational phases and showing no periodicity in $H\alpha$, as expected.
9. The analysis of correlation matrices showed that the variability in the $H\alpha$ line can be associated with different physical processes, and the red and blue wings are sometimes formed in different regions, since the variability of one wing does not always correlate with the variability of the other. This is confirmed by the lack of correlation of the blue with the red wings, seen in $\sim 34\%$ of the CTTs. Each wing tends to be well correlated with itself, indicating that each wing is dominated by a single physical phenomenon.

Acknowledgements. APS and SHPA acknowledge support from CNPq, CAPES and Fapemig. JFG acknowledges support from FCT ref project UID/FIS/04434/2013.

References

- Affer, L., Micela, G., Favata, F., Flaccomio, E., & Bouvier, J. 2013, *MNRAS*, 430, 1433
- Alencar, S. H. P. & Batalha, C. 2002, *APJ*, 571, 378
- Alencar, S. H. P., Bouvier, J., Walter, F. M., et al. 2012, *A&A*, 541, A116
- Alencar, S. H. P., Teixeira, P. S., Guimarães, M. M., et al. 2010, *A&A*, 519, A88
- Appenzeller, I. & Mundt, R. 1989, *A&ARv*, 1, 291
- Beristain, G., Edwards, S., & Kwan, J. 2001a, *APJ*, 551, 1037
- Beristain, G., Edwards, S., & Kwan, J. 2001b, *APJ*, 551, 1037
- Bessolaz, N., Zanni, C., Ferreira, J., Keppens, R., & Bouvier, J. 2008, *A&A*, 478, 155
- Blinova, A. A., Romanova, M. M., & Lovelace, R. V. E. 2015, *ArXiv e-prints*
- Bouvier, J., Alencar, S. H. P., Bouvier, J., et al. 2007a, *A&A*, 463, 1017
- Bouvier, J., Alencar, S. H. P., Harries, T. J., Johns-Krull, C. M., & Romanova, M. M. 2007b, *Protostars and Planets V*, 479
- Bouvier, J., Covino, E., Kovo, O., et al. 1995, *A&A*, 299, 89
- Cauley, P. W. & Johns-Krull, C. M. 2014, *APJ*, 797, 112
- Cody, A. M., Stauffer, J., Baglin, A., et al. 2014, *AJ*, 147, 82
- Cody, A. M., Stauffer, J. R., Micela, G., Baglin, A., & CSI 2264 Team. 2013, *Astronomische Nachrichten*, 334, 63
- Costigan, G., Vink, J. S., Scholz, A., Ray, T., & Testi, L. 2014, *MNRAS*, 440, 3444
- Dahm, S. E. 2008, *The Young Cluster and Star Forming Region NGC 2264*, ed. B. Reipurth, 966
- Dahm, S. E. & Simon, T. 2005, *AJ*, 129, 829
- Donati, J.-F., Bouvier, J., Walter, F. M., et al. 2011a, *MNRAS*, 412, 2454
- Donati, J.-F., Gregory, S. G., Alencar, S. H. P., et al. 2011b, *MNRAS*, 417, 472
- Donati, J.-F., Skelly, M. B., Bouvier, J., et al. 2010, *MNRAS*, 409, 1347
- Edwards, S., Fischer, W., Hillenbrand, L., & Kwan, J. 2006, *ApJ*, 646, 319
- Edwards, S., Fischer, W., Kwan, J., Hillenbrand, L., & Dupree, A. K. 2003, *ApJL*, 599, L41
- Fang, M., van Boekel, R., Wang, W., et al. 2009, *A&A*, 504, 461
- Ferreira, J., Dougados, C., & Cabrit, S. 2006, *A&A*, 453, 785
- Fűrész, G., Hartmann, L. W., Szentgyorgyi, A. H., et al. 2006, *ApJ*, 648, 1090
- Flaccomio, E., Micela, G., & Sciortino, S. 2006, *A&A*, 455, 903
- Fonseca, N., Alencar, S., & et al. 2015
- Giampapa, M. S., Basri, G. S., Johns, C. M., & Imhoff, C. 1993, *ApJS*, 89, 321
- Gillen, E., Aigrain, S., McQuillan, A., et al. 2014, *A&A*, 562, A50
- Gilmore, G., Randich, S., Asplund, M., et al. 2012, *The Messenger*, 147, 25
- Gregory, S. G., Donati, J.-F., Morin, J., et al. 2012, *APJ*, 755, 97
- Gullbring, E., Hartmann, L., Briceño, C., & Calvet, N. 1998, *APJ*, 492, 323
- Hartmann, L., Hewett, R., & Calvet, N. 1994, *APJ*, 426, 669
- Herbig, G. H. 1954, *ApJ*, 119, 483
- Herbst, W. 1989, *AJ*, 98, 2268
- Herbst, W., Rhode, K. L., Hillenbrand, L. A., & Curran, G. 2000, *AJ*, 119, 261
- Horne, J. H. & Baliunas, S. L. 1986, *APJ*, 302, 757
- Ingleby, L., Calvet, N., Bergin, E., et al. 2011, *APJ*, 743, 105
- Johns, C. M. & Basri, G. 1994, in *Astronomical Society of the Pacific Conference Series*, Vol. 64, *Cool Stars, Stellar Systems, and the Sun*, ed. J.-P. Caillault, 190
- Johns, C. M. & Basri, G. 1995a, *AJ*, 109, 2800
- Johns, C. M. & Basri, G. 1995b, *ApJ*, 449, 341
- Johns-Krull, C. M., Valenti, J. A., & Koresko, C. 1999, *APJ*, 516, 900
- Johnstone, C. P., Jardine, M., Gregory, S. G., Donati, J.-F., & Hussain, G. 2014, *MNRAS*, 437, 3202
- Kulkarni, A. K. & Romanova, M. M. 2008, *MNRAS*, 386, 673
- Kulkarni, A. K. & Romanova, M. M. 2009, *MNRAS*, 398, 701
- Kurosawa, R., Harries, T. J., & Symington, N. H. 2005, *MNRAS*, 358, 671
- Kurosawa, R., Harries, T. J., & Symington, N. H. 2006, *MNRAS*, 370, 580
- Kurosawa, R. & Romanova, M. M. 2013, *MNRAS*, 431, 2673
- Kurosawa, R., Romanova, M. M., & Harries, T. J. 2008, *MNRAS*, 385, 1931
- Kurosawa, R., Romanova, M. M., & Harries, T. J. 2011, *MNRAS*, 416, 2623
- Lada, C. J., Muench, A. A., Luhman, K. L., et al. 2006, *ApJ*, 131, 1574
- Lamm, M. H., Bailer-Jones, C. A. L., Mundt, R., Herbst, W., & Scholz, A. 2004, *A&A*, 417, 557
- Lima, G. H. R. A., Alencar, S. H. P., Calvet, N., Hartmann, L., & Muzerolle, J. 2010, *A&A*, 522, A104+
- Luhman, K. L., Briceño, C., Stauffer, J. R., et al. 2003, *APJ*, 590, 348
- Manara, C. F., Testi, L., Rigliaco, E., et al. 2013, *A&A*, 551, A107
- McGinnis, P. T., Alencar, S. H. P., Guimarães, M. M., et al. 2015, *A&A*, 577, A11
- McQuillan, A., Aigrain, S., & Mazeh, T. 2013, *MNRAS*, 432, 1203
- Meyer, M. R. 2009, in *IAU Symposium*, Vol. 258, *IAU Symposium*, ed. E. E. Mamajek, D. R. Soderblom, & R. F. G. Wyse, 111–122
- Muzerolle, J., Hartmann, L., & Calvet, N. 1998, *AJ*, 116, 455
- Oliveira, J. M., Foing, B. H., van Loon, J. T., & Unruh, Y. C. 2000, *A&A*, 362, 615
- Randich, S., Gilmore, G., & Gaia-ESO Consortium. 2013, *The Messenger*, 154, 47
- Rebull, L. M. 2001, *AJ*, 121, 1676
- Rebull, L. M., Makidon, R. B., Strom, S. E., et al. 2002, *AJ*, 123, 1528
- Reipurth, B., Pedrosa, A., & Lago, M. T. V. T. 1996, *A&AS*, 120, 229
- Rucinski, S. M., Matthews, J. M., Kuschnig, R., et al. 2008, *MNRAS*, 391, 1913
- Shu, F., Najita, J., Ostriker, E., et al. 1994, *ApJ*, 429, 781
- Stassun, K. G., Mathieu, R. D., Mazeh, T., & Vrba, F. J. 1999, *AJ*, 117, 2941
- Stauffer, J., Cody, A. M., Baglin, A., et al. 2014, *AJ*, 147, 83
- Stauffer, J., Cody, A. M., McGinnis, P., et al. 2015, *AJ*, 149, 130
- Sung, H., Bessell, M. S., & Lee, S.-W. 1997, *AJ*, 114, 2644
- Sung, H., Stauffer, J. R., & Bessell, M. S. 2009, *AJ*, 138, 1116
- Teixeira, P. S., Lada, C. J., Marengo, M., & Lada, E. A. 2012, *A&A*, 540, A83
- Venuti, L., Bouvier, J., Flaccomio, E., et al. 2014, *A&A*, 570, A82
- Vogt, S. S., Hatzes, A. P., Misch, A. A., & Kürster, M. 1999, *ApJS*, 121, 547
- Walker, M. F. 1956, *APJS*, 2, 365
- White, R. J. & Basri, G. 2003, *ApJ*, 582, 1109
- Zwintz, K., Fossati, L., Ryabchikova, T., et al. 2013, *A&A*, 550, A121

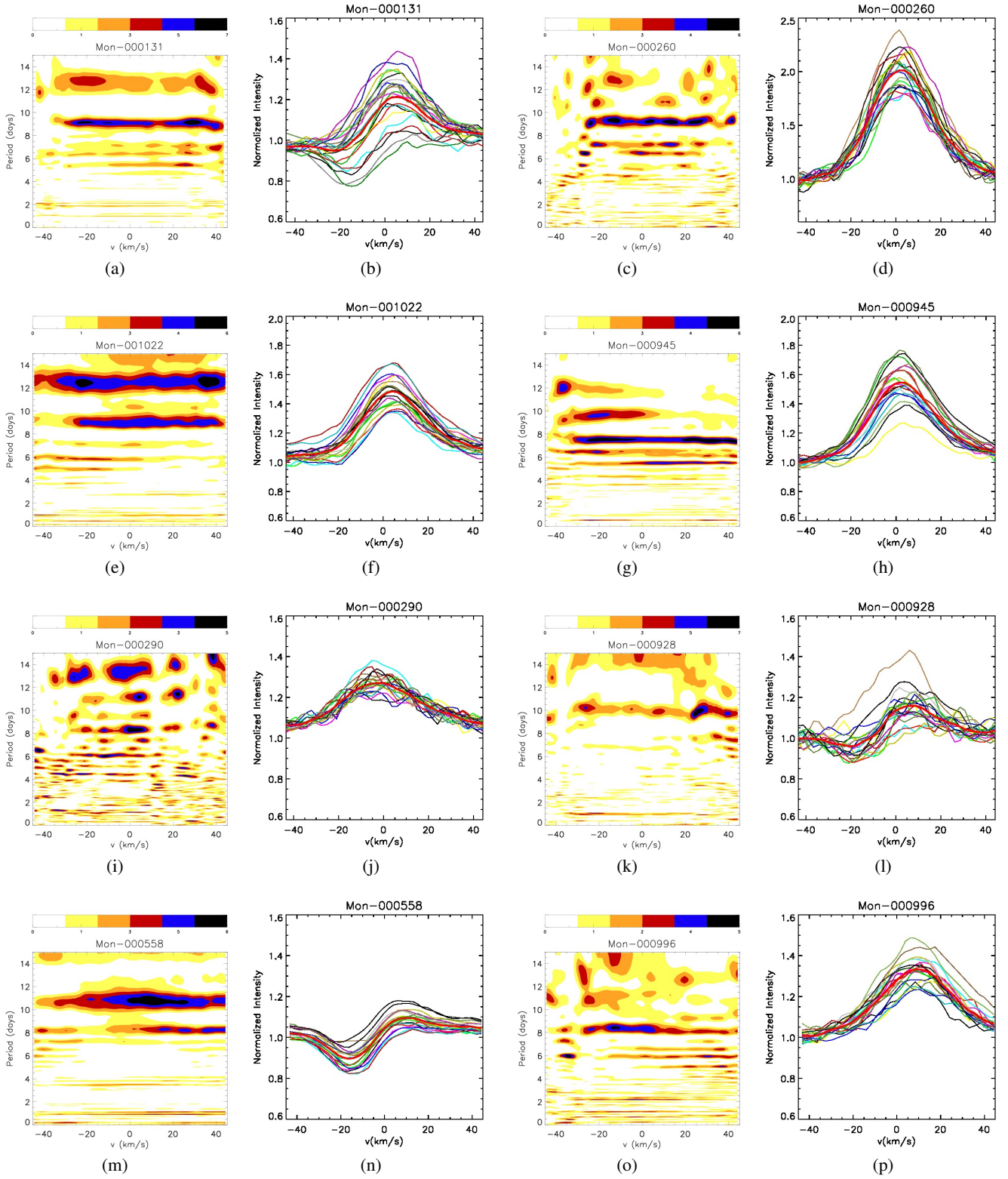


Fig. 18. Periodic stars in the HeI 6678 Å line that did not show a periodicity in the CoRoT light curves. The first and third columns show bidimensional periodograms of the HeI line. The color code represents the power of the periodogram, varying from zero (white) to the maximum power intensity (black). The second and fourth columns show the HeI 6678 Å lines used to calculate the periodograms. Different colors correspond to different nights of observation, and the thick red line is the average line profile.

Table 2. Parameters of the CTTs observed by CoRoT and/or FLAMES/VLT.

Mon ID ^a	2Mass ID ^b	SpT ^c	EW _{Hα} ^d (Å)	ErEW ^d (Å)	W10% _{Hα} ^d (kms ⁻¹)	EW _{Hα} ^e (Å)	FUR06 ^f	α _{IRAC} ^g (2008)	LC ^h (days)	P ^h (2011)	LC ^h (days)	P ^h	Q ⁱ
CSIMon-000007	06415304+0958028	K7					c	-1.47	3 (A)		3 (A)		0.75
CSIMon-000011	06411725+0954323	K7				58.3			3 (A)		3 (A)		
CSIMon-000017	06413199+1000244	K5				13.1		-2.69	1	4.78	1	4.73	-0.03
CSIMon-000021	06405944+0959454	K5				7.4	c		2	3.23	2	3.16	0.15
CSIMon-000056	06415315+0950474	K5				1.8	w	-1.36	2	5.71	2	5.86	0.14
CSIMon-000058	06420870+0941212	K4.5				94.0	c		-		1	2.14	0.22
CSIMon-000063	06411193+0959412	M2.5				19.4		-1.37	-		3		
CSIMon-000090	06410896+0933460	M3				51.0	c	-0.88	3		3		
CSIMon-000103	06405954+0935109	K6	15.6	0.9	401	6.4	c	-1.14	1	1.67	1	3.35	0.21
CSIMon-000117	06405413+0948434	M2.5				353.0		-2.34	-		3 (A)		0.72
CSIMon-000119	06412100+0933361	K6	10.5	0.9	466	10.6	c	-1.44	3		3		0.62
CSIMon-000123	06410821+0934094	M2.5:				12.0			-		3		
CSIMon-000126	06405783+0941201	M0				26.4	c	-1.09	-		3 (E)		
CSIMon-000131	06404927+0923503	K7	39.3		515	35.9	c		-		3		0.44
CSIMon-000153	06405990+0947044	M3				39.9		-1.71	1	1.90	1	1.90	0.35
CSIMon-000168	06414287+0925084	K5:M0	44.9	3.2	390	86.0	c	-1.38	3 (E)		3 (E)		
CSIMon-000177	06410620+0936229	G5	11.1	0.4	412	10.0	c	-2.03	1	3.01	1	3.01	0.22
CSIMon-000185	06413876+0932117	K4				58.6	c	-1.55	3 (A)		3 (A)		
CSIMon-000220	06412454+0937355	M3	3.3	1.5	315	8.9			1	0.76	3		0.51
CSIMon-000225	06410622+0925036	M5				34.7	w	-1.58	1	9.30	-		
CSIMon-000239	06411128+0919485		20.6		329				-		-		
CSIMon-000250	06410050+0945031	K3	18.1	1.0	457	15.0	c	-2.10	2	4.16	2	8.93	0.37
CSIMon-000260	06411099+0945556	K7	65.8	2.8	348	61.5	c	-0.93	3 (A)		-		
CSIMon-000273	06411837+0939411	M1				123.5	c	-2.28	-		3		
CSIMon-000280	06404100+0927543	K4	12.8	1.9	486	13.2	w	-1.97	3		3		
CSIMon-000290	06405867+0936132	M4	23.7	1.6	308	22.2			3		3		0.41
CSIMon-000296	06405059+0945573	K2	10.6	0.7	375	11.2	c	-2.14	3 (E)		2	3.91	0.57
CSIMon-000297	06404516+0928444	K2	24.5	0.9	520	7.2	c		2	3.16	3 (E)		
CSIMon-000314	06404459+0932261	M3	53.2	5.0	287	60.0		-2.61	3 (E)		3 (E)		0.80
CSIMon-000326	06405882+0939187	M0	21.8	1.3	247	27.9	c	-1.39	1	7.05	3		
CSIMon-000328	06412700+0930131	M1	31.9	2.5	231	25.8	w	-1.88	3		3		
CSIMon-000335	06413728+0945066	K4	15.4	0.8	340	35.0	c	-0.93	1	4.51	1	4.58	0.004
CSIMon-000340	06415593+0940468	M2.5						-2.82	-		3		
CSIMon-000341	06405426+0949203	M0.5	106.1	1.6	442	161.1	c		3 (A)		3 (A)		0.89
CSIMon-000342	06405573+0946456	M4				21.1	c	-1.79	-		3		0.68
CSIMon-000346	06410908+0930090	K7				27.0	c		-		3		
CSIMon-000346	06410908+0930090	K7				27.0	c		-		3		
CSIMon-000357	06410574+0931012	K5				8.0	c		-		3		0.15
CSIMon-000358	06410673+0947275	M3				6.2		-1.59	3 (E)		2	5.86	0.32
CSIMon-000370	06405679+0937490	K5	73.4	1.1	325	113.2	c	-1.17	3		UNC	11.82	0.21
CSIMon-000378	06405292+0944544	K5.5				8.5	w	-1.16	-		1	11.03	0.78
CSIMon-000379	06410497+0950460	K2	7.7	0.6	510	36.5	c	-1.91	3 (E)		2	3.68	
CSIMon-000397	06411078+0946411	M3.5				3.9		-2.96	3		3		0.50
CSIMon-000406	06405968+0928438	K3				46.1		-0.87	-		3 (A)		0.51
CSIMon-000412	06404711+0932401	M1				30.7	c	-1.37	-		3 (A)		
CSIMon-000423	06411485+0925550	M2.5	123.6	7.6	295	89.8		-0.57	-		3		
CSIMon-000424	06411521+0937576	M1				11.5		-1.08	-		3		
CSIMon-000425	06411668+0929522	K5				6.3	c	-0.66	-		3		
CSIMon-000426	06411945+0930286	K5				21.0			-		3		0.50
CSIMon-000433	06410111+0934522	M1				7.0	c	-2.24	-		3 (E)		0.80
CSIMon-000441	06405809+0936533	M2	21.7	2.3	342	34.0		-1.41	2	4.06	3 (E)		0.78
CSIMon-000448	06410360+0930290	M4	22.8	2.8	214	20.4		-1.12	3		3		0.63
CSIMon-000456	06405154+0943242	K4				13.1	c		-		2	5.03	
CSIMon-000457	06410673+0934459	G6:	32.1	1.5	524	49.4	c	-0.01	3		-		0.78
CSIMon-000462	06404218+0933374					7.3	c		3		3		0.90
CSIMon-000469	06404114+0933578	K7:				236.5		-0.99	-		3 (A)		
CSIMon-000474	06410682+0927322					104.7	c		-		3 (A)		0.99
CSIMon-000491	06405616+0936309	K3				67.2	c	-0.58	-		3		0.15
CSIMon-000498	06404750+0949289	K3	19.1	0.5	423	12.8	c	-1.41	2	4.23	2	4.28	
CSIMon-000510	06410429+0924521	M0	67.7	1.6	379	101.8	c	-0.97	3 (A)		3 (A)		0.48
CSIMon-000525	06405118+0944461	G0				3.5	c		3		1	1.98	
CSIMon-000553	06410303+0937357	M1				34.1			3		-		0.43
CSIMon-000558	06413974+0940279	K4	49.1	0.6	586	52.5			3 (A)		3		0.87
CSIMon-000566	06405275+0943004	M3.5				19.4			3		3		
CSIMon-000567	06405639+0935533	K3				84.1		-1.14	-		3 (A)		0.70
CSIMon-000577	06414382+0940500	K1				5.9	c	-1.49	-		3		2.74
CSIMon-000590	06405891+0928528	M1				17.8	w	-1.89	-		3		
CSIMon-000598	06405932+0946165	M1				22.7	w	-1.64	-		3		
CSIMon-000603	06405295+0926257	M5	130.4	7.9	377	130.8			-		-		
CSIMon-000613	06410577+0948174	K6.5				30.1	c	-1.65	-		3		
CSIMon-000619	06411475+0934134	K8.5				94.3	c	-1.04	-		3 (E)		0.65
CSIMon-000632	06404936+0952539	M0.5	66.3	4.6	293	78.5			-		-		
CSIMon-000636	06404884+0943256	M0				15.5	c	-0.68	-		3		

Table 2. Continued.

Mon ID ^a	2Mass ID ^b	SpT ^c	EW _{Hα} ^d (Å)	E _{FW} ^d (Å)	W10% _{Hα} ^d (kms ⁻¹)	EW _{Hα} ^e (Å)	FUR06 ^f	α IRAC ^g (2008)	LC ^h (days)	P ^h (2011)	LC ^h (days)	P ^h	Q ⁱ
CSIMon-000637	06404921+0957387	M1				50.8		-2.67	1	11.85	3		1.55
CSIMon-000650	06410098+0932444					6.4	c		3		3		0.34
CSIMon-000654	06405949+0929517	M3	23.9	2.2	361	26.2		-1.16	2	4.66	3 (E)		
CSIMon-000660	06410051+0929159	K4	1.9	1.0	484	16.6	c	-1.72	2	5.25	2	5.10	
CSIMon-000667	06412878+0938388	K3	3.1	0.5	413		w	-0.57	3 (E)		3 (E)		
CSIMon-000681	06413111+0926582	K3.5	56.8	1.1	637	25.9	c	-1.44	3		3		
CSIMon-000697	06413455+0936325	M1				4.5	c		3		3		0.49
CSIMon-000717	06411511+0926443	M0.5				24.5		-1.47	-		3 (E)		
CSIMon-000718	06410416+0920443	M2:M2				8.8			3		3		0.13
CSIMon-000754	06405302+0952594	M0				10.4		-2.82	-		1	0.97	0.22
CSIMon-000765	06405363+0933247	K1	25.2	1.0	362	18.2	c	-2.29	3		1	2.41	0.63
CSIMon-000766	06404837+0948385	M0.5				70.1		-1.38	-		3		
CSIMon-000771	06411827+0933535	K4				28.9	c	-2.39	3		3		0.82
CSIMon-000774	06405884+0930573	K2.5				14.3	c		2	3.46	3 (E)		
CSIMon-000795	06411257+0952311	G:V:e	28.4	0.5	598	35.3	c	-1.72	3		-		
CSIMon-000804	06405571+0951138	K5.5	9.9	0.8	286	8.0	w	-0.29	1	3.23	3		0.56
CSIMon-000808	06405159+0928445	K4				50.2	c	-1.85	-		3 (A)		0.06
CSIMon-000810	06410982+0927122	K5	3.1	0.7	228	3.1	c	-2.84	1	2.93	1	2.93	0.40
CSIMon-000811	06404321+0947072	K6	23.3	1.0	436	27.1	c		3 (E)		2	7.88	
CSIMon-000823	06405014+0957039	M3				5.9			-		3		
CSIMon-000824	06410183+0938411	K4	-0.5	0.6	493	1.5	c	-2.41	2	7.05	-		
CSIMon-000846	06411286+0926148		90.6	0.9	512	85.6	c		3		-		
CSIMon-000860	06415492+0942527	M2.5				261.0		-3.23	3 (A)		-		0.50
CSIMon-000877	06411678+0927301	K4				91.4	c	-1.84	-		3 (A)		
CSIMon-000879	06410338+0940448	M1				16.5	c	-2.69	-		UNC	11.40	
CSIMon-000893	06410457+0938308	M3	110.9	2.2	478	108.0		-0.78	3		-		0.98
CSIMon-000914	06405191+0937558	G0:G5						1.87	-		3		
CSIMon-000919	06411329+0931503	M4				79.9		-1.04	-		3 (A)		
CSIMon-000926	06410642+0928388	M1.5	63.0	2.6	258	56.1	c	-1.57	3		3		
CSIMon-000928	06412562+0934429	M0	13.0	1.4	360	15.9		-1.11	2	4.96	3		
CSIMon-000931	06411808+0938253	M3				32.5		-2.89	1	0.98	3		
CSIMon-000936	06410715+0927294	K5				42.8	w	-0.95	-		3		1.05
CSIMon-000937	06405255+0952059	K7	8.5	1.0	371	6.9		-2.40	3		3		
CSIMon-000945	06404989+0936494	K4	56.9	1.4	383	66.3		-1.43	3 (A)		3 (A)		0.61
CSIMon-000951	06411792+0929011	M2.5	65.7	4.5	206	231.4	w		3		3		0.54
CSIMon-000964	06410711+0912383	K6	13.9	1.2	233		w	-1.25	1	3.34	1	3.32	0.03
CSIMon-000965	06404600+0917582	M2	14.4	1.6	305		c	-2.51	1	9.38	1	9.68	0.88
CSIMon-000996	06404131+0951023	K7	52.8	1.3	506	24.5		-1.19	3 (A)		3 (A)		0.55
CSIMon-001003	06402564+0959597	M4				157.0		-0.98	1	3.46	3		1.06
CSIMon-001017	06402373+0955238	M3				80.6	c	-1.22	1	4.66	3		0.63
CSIMon-001022	06403911+0950586	K4	33.0	1.1	584	46.5	c	-1.55	3 (A)		3 (A)		0.42
CSIMon-001031	06404005+0935029	K4				7.0	c	-0.30	-		1	4.51	
CSIMon-001033	06404102+0947577	K7	6.3	0.9	434	7.5	w	-1.97	1	14.15	-		0.55
CSIMon-001037	06403086+0934405	K1				22.2	c	-1.29	3 (E)		3 (E)		0.52
CSIMon-001053	06404113+0952565	K6				32.4	w	-1.03	-		3		0.71
CSIMon-001054	06403652+0950456	M2	29.7	1.5	295	21.1	w	-1.29	3 (E)		2	4.08	0.23
CSIMon-001055	06404041+0950504	K7				58.3		-2.42	1	3.76	1	3.76	0.78
CSIMon-001061	06402416+0934124	M0				20.1	c	-0.79	-		3		-0.06
CSIMon-001064	06403518+0951567	M1				16.4		-0.68	-		1	2.70	0.39
CSIMon-001094	06403164+0948233	K5				54.6	c	-1.96	-		UNC	4.25	0.36
CSIMon-001099	06404136+0954138	G1	8.5	0.5	406	12.2	c		1	3.31	1	3.38	0.58
CSIMon-001100	06403934+0934455	K6				57.2	c	-0.42	-		3		0.41
CSIMon-001114	06393339+0952017	M1.5					c		1	2.56	1	2.56	0.44
CSIMon-001128	06401780+0925478	M2.5	137.9		514	34.4			-		-		
CSIMon-001131	06393441+0954512	M2					c		3 (E)		2	5.18	0.51
CSIMon-001132	06402587+0950576	M2.5				166.0		-0.99	-		UNC	2.93	0.48
CSIMon-001140	06394147+0946196	K4					c		2	3.87	2	3.90	0.75
CSIMon-001144	06402309+0927423	K5	52.3	3.4	536	49.5	c	-1.73	3 (E)		3 (E)		
CSIMon-001149	06403059+0950147	M3				33.9	c		-		3		
CSIMon-001149	06403059+0950147	M3				33.9	c		-		3		0.22
CSIMon-001156	06403357+0933363	M2.5:				19.9		-3.21	-		3		0.80
CSIMon-001167	06403787+0934540	M3				23.4	c	-1.87	3 (E)		2	8.78	0.64
CSIMon-001174	06401370+0956305	M2				130.2	c	0.01	3 (A)		3 (A)		0.57
CSIMon-001181	06401801+0950220	M2				12.1			-		3		0.59
CSIMon-001199	06404184+0951445	K5	10.1	0.8	487	22.9		-1.53	2	3.75	2	3.61	0.56
CSIMon-001217	06403665+0952032	K4				87.0	c		-		3 (A)		0.62
CSIMon-001221	06402342+0954555	M4.5				32.1			-		3		0.22
CSIMon-001234	06401113+0938059	K6				52.9	c	-1.35	3		3		0.71
CSIMon-001249	06402027+0956063	M3				33.5	c	-0.67	-		3		
CSIMon-001275	06402877+0931002	K4	27.8	1.9	640	1.8	w	-0.56	3		3		0.30
CSIMon-001287	06401110+0921270	M3	126.0		315	163.1			-		-		
CSIMon-001294	06400552+0922260	K2:K4				31.2	c	-1.65	-		3		0.33
CSIMon-001296	06390374+0940234	K7					c		3 (E)		2	9.75	0.40
CSIMon-001304	06401361+0924494	K0					c	-2.81	1	1.11	1	1.08	

Table 2. Continued.

Mon ID ^a	2Mass ID ^b	SpT ^c	EW _{Hα} ^d (Å)	E _{FW} ^d (Å)	W10% _{Hα} ^d (kms ⁻¹)	EW _{Hα} ^e (Å)	FUR06 ^f	α_{IRAC} ^g (2008)	LC ^h (days)	P ^h (2011)	LC ^h (days)	P ^h	Q ⁱ
CSIMon-001308	06395924+0927245	M0					c	-1.87	2	6.45	2		6.68
CSIMon-001573	06401258+1005404	M0					c	-1.37	1	8.78	3 (A)		
CSIMon-001580	06410285+1007119	M1					c		1	7.51	-		
CSIMon-005009	06420991+0947540	M2.5							-		3		
CSIMon-005664	06405448+0909318								1	1.19	3		
CSIMon-005745	06420434+0909408	M2.5							-		3		
CSIMon-005836	06412909+0918155								-		3		
CSIMon-006079	06392911+0942386	M1							B		B		
CSIMon-006324	06394874+0917351								-		3		
CSIMon-006325	06401447+0913372	M0.5						-2.88	-		3		
CSIMon-006465	06392516+0932381	K3.5							B		B		
CSIMon-006491	06392550+0931394	K5							-		3		
CSIMon-006930	06390409+0916139	M0							3		3		
CSIMon-006986	06390996+1005127	K7:M1							2	6.16	-		
CSIMon-006991	06392200+1006233	M0.5							3		3		
CSIMon-007004	06392595+1005075								3		3		
CSIMon-014132	06390355+0916159	M3.5							-		2		9.10

Notes. Only a portion of this table is shown here. A full version is available in the online journal. This table is ordered according to the Mon ID.

^(a) “CSIMon” is an internal identification of the CSI 2264 campaign. Elsewhere in the text “CSI” was omitted for brevity. ^(b) 2MASS identification. ^(c) Spectral type obtained by Venuti et al. (2014); Dahm & Simon (2005); Rebull et al. (2002); Walker (1956). ^(d) H α parameters obtained in this work using FLAMES spectra. We used the convention that positive H α equivalent width indicates H α in emission, and negative values indicate H α in absorption. The uncertainties were obtained assuming a Poisson distribution. ^(e) H α equivalent width obtained by Dahm & Simon (2005). ^(f) Classification as CTTS (c) and WTTS (w) by Fűrész et al. (2006). ^(g) α_{IRAC} is the slope of the spectral energy distribution between 3.6 μ m and 8 μ m obtained by Teixeira et al. (2012). ^(h) CoRoT light curve morphology and photometric period obtained in this work: “1”= spot-like, “2”= AA Tau-like, “3”= non-periodic light curves. Accretion bursts and aperiodic extinction light curves are identified by (A) and (E), respectively. “UNC” = unclassified light curve and “B”= Binary. ⁽ⁱ⁾ Parameter defined by Cody et al. (2014) to distinguish periodic from aperiodic light curves. According to Cody et al. (2014), when Q>0.6 the star is not periodic photometrically.

Table 3. Parameters of the WTTSs observed by CoRoT and/or FLAMES/VLT.

Mon ID ^a	2Mass ID ^b	SpT ^c	EW _{Hα} ^d (Å)	Er _{EW} ^d (Å)	W10% _{Hα} ^d (kms ⁻¹)	EW _{Hα} ^e (Å)	FUR06 ^f	α_{IRAC} ^g
Mon-000008	06414859+0954115	K5						
Mon-000009	06420914+0948048	F5						
Mon-000014	06420664+0941317	K7:M0						
Mon-000015	06420911+0959027	K7:M0						
Mon-000018	06411322+0955086	K3:K4				3.0		-2.73
Mon-000020	06420924+0944034	K7					w	
Mon-000022	06410457+1000426	M4						
Mon-000024	06415684+0947451	M1						
Mon-000026	06410518+1000189	M4				6.5		
Mon-000029	06410328+0957549	K7				1.5		-2.85
Mon-000033	06410726+0958311	K5				1.4	w	-2.78
Mon-000035	06414775+0952023	F0						
Mon-000038	06411088+1000409	F2:F5						
Mon-000045	06415305+1000023	M3.5						-2.72
Mon-000050	06410153+1000365	K4				1.1		-2.88
Mon-000051	06411380+0955439	G0				-2.6		
Mon-000055	06413491+1001472	M2						-2.80
Mon-000057	06410393+0958094	M3				4.1	w	-2.74
Mon-000060	06411532+0954509	M3				4.0		-2.92
Mon-000066	06410357+1000353	M1				6.9		-2.66
Mon-000071	06410025+0958496	K1.5				-1.2		
Mon-000075	06411159+1002235	K4						-2.84
Mon-000086	06404645+0959463	M0						-3.04
Mon-000087	06410659+0935451	G5						
Mon-000088	06413404+0921132	M2:M2						
Mon-000093	06411705+0932523	M2.5				2.1		
Mon-000096	06405863+0945546	M0						
Mon-000102	06404323+0931149	M3				5.0	w	
Mon-000105	06405041+0948506	K4				0.4		
Mon-000108	06411484+0932358	M3				2.2		-2.85
Mon-000122	06414711+0938047	K6				1.4		-2.84
Mon-000130	06410521+0953157		0.9	0.7	249	1.5		
Mon-000135	06405999+0928500	K7				1.7		-2.59
Mon-000139	06405367+0958000	M1				3.2		-3.16
Mon-000145	06412346+0945586	K7				4.0		-2.46
Mon-000146	06404572+0958288	K5						
Mon-000149	06411330+0951544	M1				2.0		-2.69
Mon-000158	06404484+0946384	K0.5						-3.80
Mon-000159	06405146+0937144	M1				3.4		-4.65
Mon-000160	06405983+0951489	M2	3.4	1.2	165	4.9		-2.96
Mon-000164	06410450+0930134	M				8.6		
Mon-000169	06414806+0942433	G5						
Mon-000172	06411031+0921495	M2.5				2.7		
Mon-000176	06405220+0952311	M2				3.5		-2.85
Mon-000188	06410172+0955514	M3.5				3.6		-2.82
Mon-000198	06411963+0931443	K5				1.5		-2.63
Mon-000200	06410801+0930403	K4				0.5		-3.22
Mon-000206	06405938+0957356	K7						-2.48
Mon-000207	06405904+0949062	M2:M2				10.3		
Mon-000216	06410370+0928200	M1				9.3		-2.18
Mon-000217	06410696+0940544	M3.5				2.8		
Mon-000223	06405542+0937237	K6				1.8	w	-2.73
Mon-000226	06410536+0933134	K5				2.7	w	-2.78
Mon-000227	06405395+0950580	M3.5						-3.32
Mon-000236	06410253+0934557	K0	0.8	0.6	212	0.6		-2.98
Mon-000237	06410968+0924547	M1				1.7		
Mon-000241	06412303+0927266	G8	-2.3	0.5				
Mon-000247	06410728+0949566	M4.5				4.3		
Mon-000253	06411288+0946007	M3.5						-2.93
Mon-000255	06414273+0942566	M0				0.9	w	-2.82
Mon-000256	06414422+0925024	M2	5.5	2.0	236			-2.02
Mon-000263	06410258+0935131	K5				1.3		-2.82
Mon-000279	06412119+0932146	M2.5				5.8		-1.59
Mon-000281	06405607+0942540	M4				8.0		
Mon-000292	06414741+0942003	M1				2.6		-2.88
Mon-000294	06410436+0927306	M3						
Mon-000298	06410568+0954187	M1				3.8		-2.75
Mon-000306	06411249+0946203	>M4				12.5		-2.70
Mon-000307	06411792+0933370	M0				2.9		-2.99
Mon-000311	06415578+0939580	M2.5						-2.74
Mon-000319	06405146+0931468	M2						
Mon-000330	06413160+0948328	K2	1.2	0.6	145	5.2		-2.84
Mon-000339	06413433+0925533	M3				4.5		-2.74

Table 3. Continued.

Mon ID ^a	2Mass ID ^b	SpT ^c	EW _{Hα} ^d (Å)	E _{FEW} ^d (Å)	W10% _{Hα} ^d (kms ⁻¹)	EW _{Hα} ^e (Å)	FUR06 ^f	α_{IRAC}^g
Mon-000344	06410951+0935254	M2				3.9		
Mon-000345	06404506+0951276	M2				2.1		
Mon-000348	06405008+0952275	M4				6.2		-2.59
Mon-000351	06412280+0929389	K5						-3.04
Mon-000365	06404492+0949091	M2:M2				2.6		
Mon-000368	06405839+0927250	>M4				6.7		-2.70
Mon-000372	06412054+0945355	K4	0.5	0.6	110			-2.76
Mon-000377	06414886+0943134	K5	-1.2	0.7				
Mon-000383	06405577+0940181	M2.5				4.6		-2.66
Mon-000389	06404875+0932425	K4				1.5		
Mon-000394	06410776+0941149	M0				2.9	w	-2.87
Mon-000395	06411013+0931285	M3.5				3.6		
Mon-000396	06411251+0935088	M4:M5						
Mon-000397	06411078+0946411	M3.5				3.9		-2.96
Mon-000407	06412203+0951126	K7				2.8		-2.71
Mon-000413	06414644+0943068	K6				2.1		
Mon-000415	06404385+0948305	M1				4.8		-2.31
Mon-000420	06405419+0955519	M0				2.0		-1.91
Mon-000427	06404244+0932206	K4				0.5		-2.01
Mon-000430	06405677+0930150	M0.5				5.0		-2.85
Mon-000434	06410406+0935211	M2.5				4.3		-1.25
Mon-000438	06410342+0930049	M2:				4.0		-2.63
Mon-000440	06413905+0929381	M0						
Mon-000443	06412756+0931558	K4						-2.73
Mon-000444	06414457+0942124	M2				3.7		-2.77
Mon-000445	06420256+0936525	K6						
Mon-000450	06415804+0943062	K6					w	-2.95
Mon-000451	06415147+0944096	M1						-2.71
Mon-000461	06415496+0930065	M2						-2.77
Mon-000468	06410886+0946010		-3.2	0.3		-2.6		
Mon-000477	06411574+0926168	K5				1.9	w	
Mon-000486	06410403+0949087	K7				2.0		-2.70
Mon-000488	06405783+0956299	K2.5						-2.93
Mon-000497	06410220+0951519	K0	-1.3	0.3		-1.6		
Mon-000499	06410455+0925183	M4				2.7		
Mon-000515	06413623+0939204	K7	1.3	1.1	159	1.6		
Mon-000516	06404735+0948494	M1				1.8		-2.49
Mon-000518	06410168+0948221	K5	0.7	0.5	208	1.8		-2.96
Mon-000519	06410992+0930202	M2:M2						
Mon-000524	06410433+0948220	K4						-2.71
Mon-000529	06405121+0927578	M2:M2						
Mon-000535	06404587+0938443	M5				4.1		-2.50
Mon-000536	06405201+0945048	M1	2.2	0.9	270	2.8		-2.28
Mon-000545	06410581+0952478	K7				0.9		
Mon-000548	06410856+0942515	M1				1.7		-2.61
Mon-000555	06412445+0932451	M5				1.8		
Mon-000559	06412425+0931541	K6						
Mon-000560	06411571+0938182	G5	-3.3	0.3				
Mon-000563	06414184+0933022	M4						
Mon-000565	06410077+0951223	K4.5				1.6	w	
Mon-000568	06405377+0930389	F5						
Mon-000574	06405086+0955530	K7				2.3		-2.98
Mon-000583	06405321+0929541	M3				15.8		
Mon-000596	06414744+0937526	M1				5.6		-3.05
Mon-000606	06411446+0933214	K5				1.9		-2.42
Mon-000607	06411563+0926334	M3.5				5.5		-2.71
Mon-000609	06413960+0933198	M3				12.5		-3.09
Mon-000610	06404539+0937515	K7:M0						-2.29
Mon-000612	06405820+0955445	M3				5.3		-2.75
Mon-000614	06404184+0941386	M3:M3				3.1		
Mon-000617	06410948+0951500	M3				2.2	w	-2.20
Mon-000620	06412074+0930119	M2						
Mon-000622	06412179+0945309	K5				1.5		-3.03
Mon-000624	06410510+0951445	K5	1.0	0.7	190	1.7	w	-3.06
Mon-000629	06410599+0935513	G2						
Mon-000630	06405750+0949208	M3.5						
Mon-000646	06404608+0949173	K0						
Mon-000647	06410295+0947543	F5						
Mon-000656	06412054+0947300	M2				2.7		-2.92
Mon-000657	06411771+0929261	M3	3.4	1.2	145	2.4	c	-2.69
Mon-000661	06405024+0920023	M0						-2.81
Mon-000665	06410593+0927174	M3	8.7	1.6	160	2.6		-2.66
Mon-000677	06405932+0922218	M4						
Mon-000680	06411333+0928074	K5				1.9		-4.34

Table 3. Continued.

Mon ID ^a	2Mass ID ^b	SpT ^c	EW _{Hα} ^d (Å)	E _{EW} ^d (Å)	W10% _{Hα} ^d (kms ⁻¹)	EW _{Hα} ^e (Å)	FUR06 ^f	α_{IRAC}^g
Mon-000684	06414359+0939411	M4				4.2		-2.46
Mon-000688	06410509+0948479	M0	0.8	0.9	190			-2.94
Mon-000695	06413250+0938074	K6	1.1	0.6	152	1.3		-2.83
Mon-000705	06411027+0933250	M3				2.7		-2.69
Mon-000714	06412214+0921310	M3				3.8		
Mon-000719	06410443+0951260	K5						-2.79
Mon-000723	06405254+0950585	M2.5						-2.00
Mon-000724	06405267+0944210	M2	3.9	1.1	186	2.2	w	-3.26
Mon-000728	06410777+0944030	F2	-2.2	0.4				
Mon-000743	06410740+0931110	M2.5				1.7		
Mon-000745	06404827+0936386	M1				2.5		-2.77
Mon-000747	06412202+0943127	K6					w	
Mon-000749	06411413+0926405	M1				1.9		-2.54
Mon-000753	06410597+0939142	M5				7.4		-1.28
Mon-000755	06404695+0948480	K6				2.0		-2.93
Mon-000757	06405219+0956433	M1				3.1		-3.21
Mon-000758	06413731+0931577	M2.5						
Mon-000769	06405411+0929510	M2	6.2	2.2	97	3.6		
Mon-000770	06411448+0937143	M0	2.2	1.3	154	4.1		-2.96
Mon-000777	06410319+0926030	M0				3.9		
Mon-000779	06404819+0927008	M5				3.3		
Mon-000784	06410141+0934081	K5				1.8	w	-2.40
Mon-000798	06405694+0948407	F9				3.9		
Mon-000805	06414494+0944403	K7						
Mon-000809	06410349+0931184	G3				-2.5		
Mon-000819	06412918+0939359	G5	-1.8	0.3		-1.4		
Mon-000826	06405208+0952138	K8.5				2.0		-3.33
Mon-000842	06405810+0951134	M2.5						-2.53
Mon-000843	06405137+0930133	M5				3.5		-2.79
Mon-000848	06412473+0926233	G8						
Mon-000869	06405745+0929234	M2.5	3.5	2.0	116	4.0		-2.53
Mon-000872	06404610+0947501	M2				0.7		
Mon-000876	06411212+0929521	M3.5				2.8		
Mon-000878	06412297+0929307	M2.5						
Mon-000881	06410891+0941147	K5				1.0		-3.05
Mon-000886	06404504+0945418	K7				2.4	w	
Mon-000890	06405517+0950498	K5.5	1.9	0.9	191	2.8		-9.15
Mon-000894	06411542+0946396	K1				0.2		-3.01
Mon-000901	06404335+0950595	K7				1.7	w	-2.46
Mon-000907	06413589+0940419	M2.5:						-2.13
Mon-000910	06404792+0933031	M2.5						-2.83
Mon-000920	06412884+0934540	M2.5						
Mon-000927	06413899+0933168	M4						
Mon-000932	06404485+0957442	K6				1.6	w	
Mon-000933	06410554+0931405	M3				3.0		
Mon-000938	06404232+0934250	M3				5.2		
Mon-000941	06412874+0927107	M3				4.1		
Mon-000948	06412715+0935061	K2				1.1		-2.97
Mon-000954	06410734+0925549	K4				1.7	w	-2.01
Mon-000958	06405545+0909289	M1						
Mon-000967	06411362+0913534	K5						
Mon-000977	06405910+0916593	M3.5						-3.02
Mon-000985	06401515+1001578	K0					w	
Mon-000989	06400851+0944134	M1				3.5		-2.75
Mon-000990	06403768+0939397	K7				2.0		-2.61
Mon-000991	06401930+0948299	M0				2.5		-3.13
Mon-000995	06402569+0958356	K2						
Mon-001000	06401168+0945559	M2				8.0		-2.90
Mon-001005	06400522+0950565	M2.5					w	-2.00
Mon-001009	06394626+0948198	K7:M0						
Mon-001012	06403332+0958529	M0						-2.90
Mon-001015	06393931+0955596	M0					w	
Mon-001016	06402103+0936319	G6				0.3	w	
Mon-001023	06401030+0938550	K7				2.0	w	-2.84
Mon-001024	06402313+0956198	G8						
Mon-001027	06403720+0931098	M2.5				4.4	w	-2.85
Mon-001029	06395984+0933416	K7						-3.13
Mon-001047	06395562+0947318	M3					w	-2.79
Mon-001051	06400420+0943123	M2				5.7		-2.84
Mon-001056	06400630+0935565	M2						-2.60
Mon-001067	06401092+0954260	M3				14.2		-2.67
Mon-001072	06403134+0941292	K7						
Mon-001074	06400842+0959259	M3				12.8		-2.67
Mon-001075	06402547+0948259	K5				0.8	w	-2.78

Table 3. Continued.

Mon ID ^a	2Mass ID ^b	SpT ^c	EW _{Hα} ^d (Å)	E _{FW} ^d (Å)	W10% _{Hα} ^d (kms ⁻¹)	EW _{Hα} ^e (Å)	FUR06 ^f	α _{IRAC} ^g
Mon-001081	06402096+0923542	K7						
Mon-001082	06400112+0935335	M2.5					w	-2.73
Mon-001085	06403280+0951293	K6				2.7	w	-4.01
Mon-001087	06400121+0942364	M2.5:						
Mon-001089	06402989+0950104	K2	-0.6	0.5				
Mon-001090	06402774+0925191	M4	5.1	3.3	84	2.6		-2.81
Mon-001092	06403867+0936569	M3				4.3		-2.88
Mon-001101	06401095+0938407	M0.5						
Mon-001102	06401212+0949306	K5						-2.88
Mon-001105	06402886+0933055	M3				3.5		-2.73
Mon-001115	06400215+0945143	K6						-2.46
Mon-001126	06400961+0941434	G9				-1.7		
Mon-001133	06395957+0956243	K6				3.5		-2.67
Mon-001142	06403446+0935182	M2				10.9	w	-1.89
Mon-001147	06394982+0956218	K7:M0						
Mon-001152	06403948+0948399	F6						
Mon-001157	06402009+0928285	K6	5.9	2.1	218	3.2		-0.79
Mon-001158	06392625+0941108	M0				-1.1	w	
Mon-001163	06402974+0959333	K7:M0						
Mon-001170	06403636+0922445	K7						-2.76
Mon-001171	06393398+0949208	K7					w	
Mon-001172	06400637+0939335	K7:M0					w	-2.62
Mon-001189	06403902+0935599	M0				3.5		-3.16
Mon-001192	06403878+0921382	K3	-1.3	0.9				-2.97
Mon-001193	06393474+0946541	M0						
Mon-001194	06403668+0922051	K7:M0						-2.84
Mon-001195	06403489+0954071	M4				5.2		
Mon-001200	06401244+0944231	M1				3.6	w	-2.93
Mon-001201	06403662+0948229	K5	2.4	0.8	171	4.9	w	-4.19
Mon-001204	06394960+0933221	K5					w	-2.75
Mon-001205	06402881+0948240	K5						-2.07
Mon-001209	06400143+0931057	K7:M0						
Mon-001218	06402858+0935476	M0				1.2	w	-2.63
Mon-001219	06402744+0952303	M4				6.8		
Mon-001223	06400600+0949426	M2				4.3	w	-1.29
Mon-001226	06401535+0942424	K5:K7						
Mon-001229	06403697+0939097	M1				5.0		-1.92
Mon-001232	06403785+0949509	M2.5:				3.0		
Mon-001235	06403667+0947225	K5						
Mon-001236	06402221+0954288	M0				2.1	w	-2.86
Mon-001238	06395109+0936328	M1:						-2.87
Mon-001239	06393884+0951518	F2						
Mon-001242	06403749+0954578	G0						
Mon-001247	06402894+0942171	K6				1.7	w	-2.56
Mon-001248	06394672+0940539	G5						-2.78
Mon-001250	06402066+0934343	K5						-2.42
Mon-001251	06403183+0936006	M2.5						-2.46
Mon-001254	06401700+0946332	M0				0.7		-2.95
Mon-001256	06394157+0934405	G0				-3.3		
Mon-001259	06403482+0945452	M2.5				4.2		
Mon-001261	06401727+0925442	M4				4.0		-2.70
Mon-001264	06403061+0946106	K4				1.5		
Mon-001265	06401088+0940072	M3				9.7		-2.54
Mon-001271	06400267+0941488	M2.5						-2.85
Mon-001274	06404142+0948096	K5				2.4		-3.47
Mon-001277	06402651+0935219	M1				2.9		-3.06
Mon-001278	06404179+0949523	M0				4.2	w	-2.53
Mon-001279	06403123+0931071	K6	2.6	1.1	217	1.7		-2.85
Mon-001281	06392269+0917037	F2						
Mon-001282	06400268+0918198	G2:G5						
Mon-001284	06401344+0919276	G1:G2						
Mon-001286	06401187+0921100	M1				3.9		-2.81
Mon-001290	06393037+0933374	K7					w	
Mon-001291	06395232+0919094	M0:M2						-2.73
Mon-001292	06394771+0926067	F5						
Mon-001295	06401580+0921333	M1				5.8		-2.80
Mon-001298	06401404+0920285	G6						
Mon-001300	06393602+0924261	K7						
Mon-001302	06391570+0929293	K7						
Mon-001303	06400402+0927070	M0						
Mon-001307	06392294+0936168	K0						
Mon-001309	06394264+0931514	M1						
Mon-001310	06392935+0920589	F7						
Mon-001313	06403632+0918575	M1	2.2	0.9	251		w	-2.76

Table 3. Continued.

Mon ID ^a	2Mass ID ^b	SpT ^c	EW _{Hα} ^d (\AA)	E _F EW ^d (\AA)	W10% _{Hα} ^d (kms^{-1})	EW _{Hα} ^e (\AA)	FUR06 ^f	α_{IRAC} ^g
Mon-001359		M3	5.4	2.2	116	3.1		
Mon-001386	06391703+0958153	K5						
Mon-001388	06393297+0956293	G2:G5						
Mon-001397	06401095+0938407	M2:M2						
Mon-001579	06403511+1004218	K7						-2.78
Mon-001581	06413573+1004158	M3.5						
Mon-001610	06395509+0921526							
Mon-001618	06414559+0939311					2.6		
Mon-001624	06405362+0947043	M4				8.1	w	-1.99
Mon-006037	06392936+0943398							

Notes. Only a portion of this table is shown here. A full version is available in the online journal. This table is ordered according to the Mon ID. ^(a) “CSIMon” is an internal identification of the CSI 2264 campaign. ^(b) 2MASS identification. ^(c) Spectral type obtained by Venuti et al. (2014); Dahm & Simon (2005); Rebull et al. (2002); Walker (1956). ^(d) H α parameters obtained in this work using FLAMES spectra. We used the convention that positive H α equivalent width indicates H α in emission, and negative values indicate H α in absorption. The uncertainties were calculated assuming a Poisson distribution. ^(e) H α equivalent width obtained by Dahm & Simon (2005). ^(f) Classification as CTTS (c) and WTTS (w) by Fűrész et al. (2006). ^(g) α_{IRAC} is the slope of the spectral energy distribution between 3.6 μm and 8 μm obtained by Teixeira et al. (2012).

Appendix A: Correlation matrices and H α line profiles

We present in this appendix the correlation matrices and H α line profiles of all the CTTSs we observed with the FLAMES spectrograph during the CSI 2264 campaign. We organized the correlation matrices according to the three main morphologies discussed in Sect 11. Some correlations matrices are difficult to fit in a single morphological class, and in these cases, we classified the star according to the most representative feature present in the correlation matrix. In Fig. A.1, we grouped all the CTTSs that show anticorrelation in some part of the H α line profile, like the stars in Fig. 21. A few stars that were not included in this first group present correlation matrices with anticorrelation only in the narrow nebular emission region, near zero velocity. This is due to difficulties in removing the nebular contribution, and the anticorrelation is not related to an emission or absorption region of the star-disk system. In Figs. A.2, A.3 and A.4, we organized the stars that show correlation in almost all of the profile, like the matrix in Fig. 22c. Finally, in Figs. A.5 and A.6, we present the stars that show no sign of correlation between the red and the blue wings in most of the profile, like the matrix in Fig. 22a.

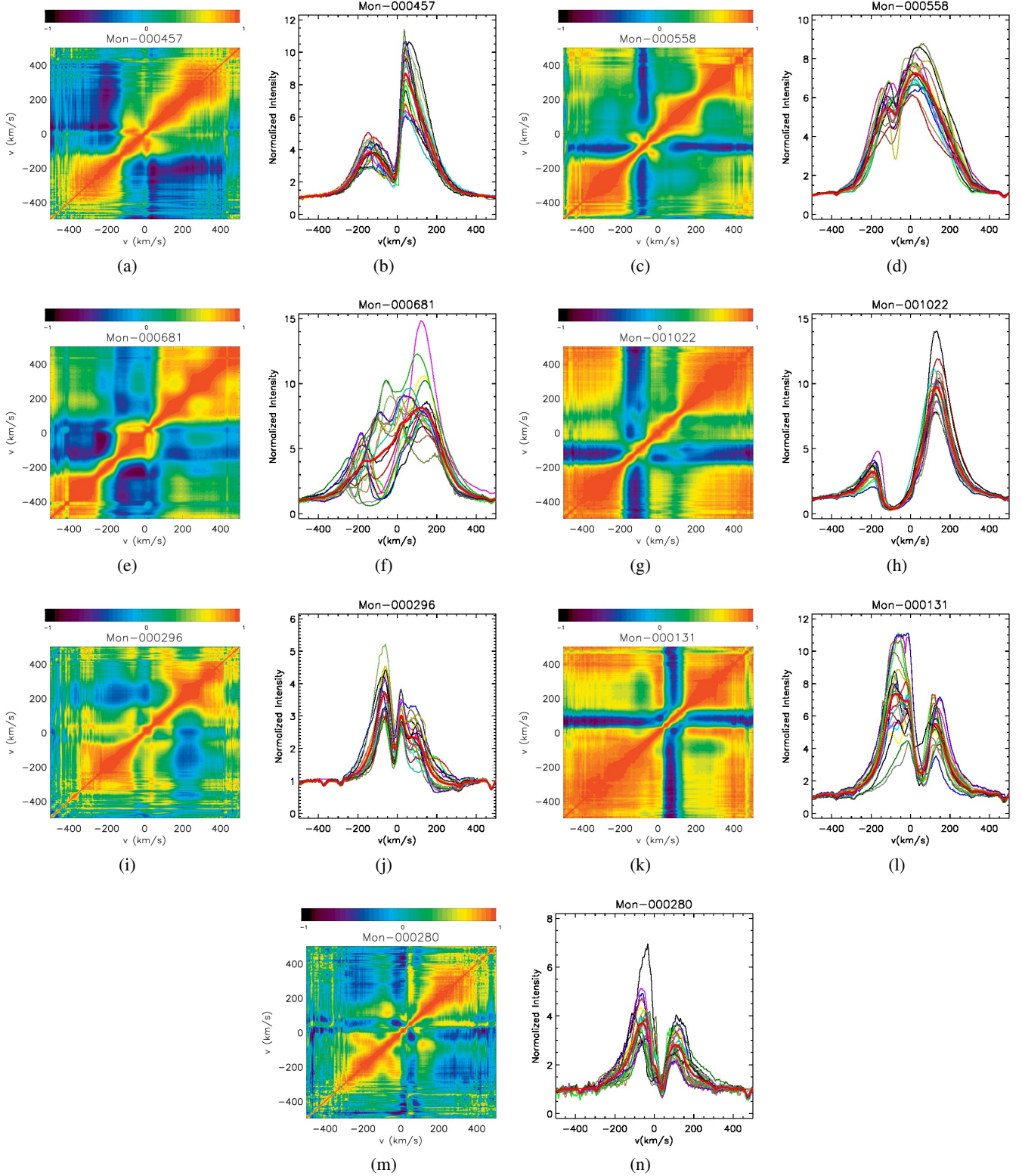


Fig. A.1. Correlation matrices (left) of the $H\alpha$ line of selected CTTSs and the corresponding line profiles (right). In the left panels, the color range corresponds to the value of the linear correlation coefficient, $r(i, j)$, between different velocity bins (i and j), of the $H\alpha$ line profiles, as described in Sect. 11. Perfect anticorrelation corresponds to -1 (black), no correlation to 0 (light blue), and a perfect correlation to 1 (orange). When $i = j$, $r(i, j) = 1$, and for all values of i and j , $r(i, j) = r(j, i)$, implying that the matrix is symmetrical relative to the diagonal. In the right panels, different colors correspond to spectra observed in different nights, and the thick red line is the average line profile. The stars in this group present anticorrelation of some part of the line profile. The anticorrelation seen in these stars is associated with blue- or redshifted absorption or emission that varies in antiphase with the rest of the profile. For example, when in panel a (Mon-000457) the red wing emission increases in intensity, the blue wing emission decreases.

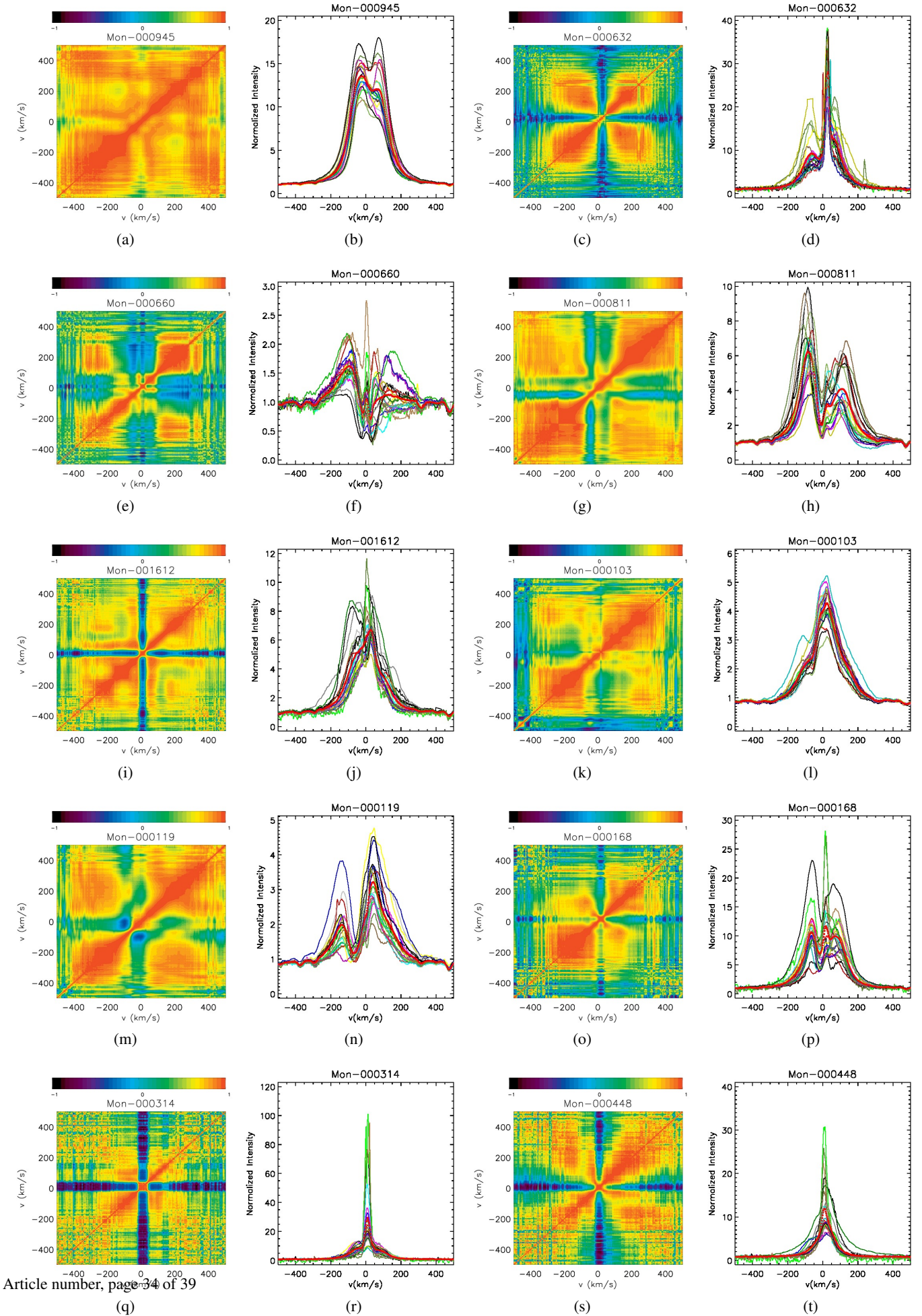


Fig. A.2. Same as Fig. A.1, but for stars that present strongly correlated line profiles, as indicated by the positive correlation in almost the entire line profile. The narrow anticorrelation region in the matrices of Mon-000632, Mon-001612, Mon-000119, Mon-000314, and Mon-000448 is due to the nebular contribution that was not entirely removed.

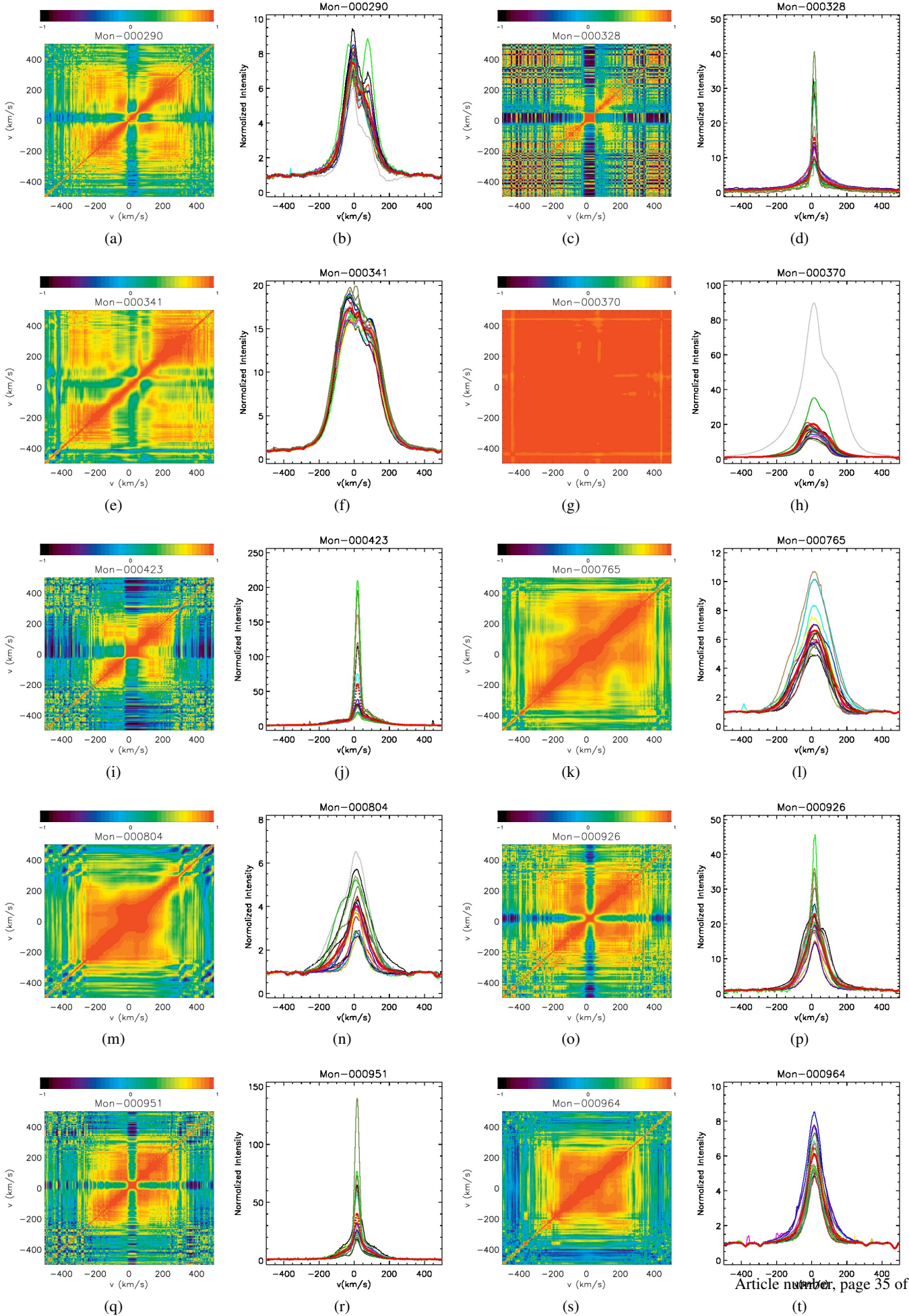


Fig. A.3. Same as Fig. A.2

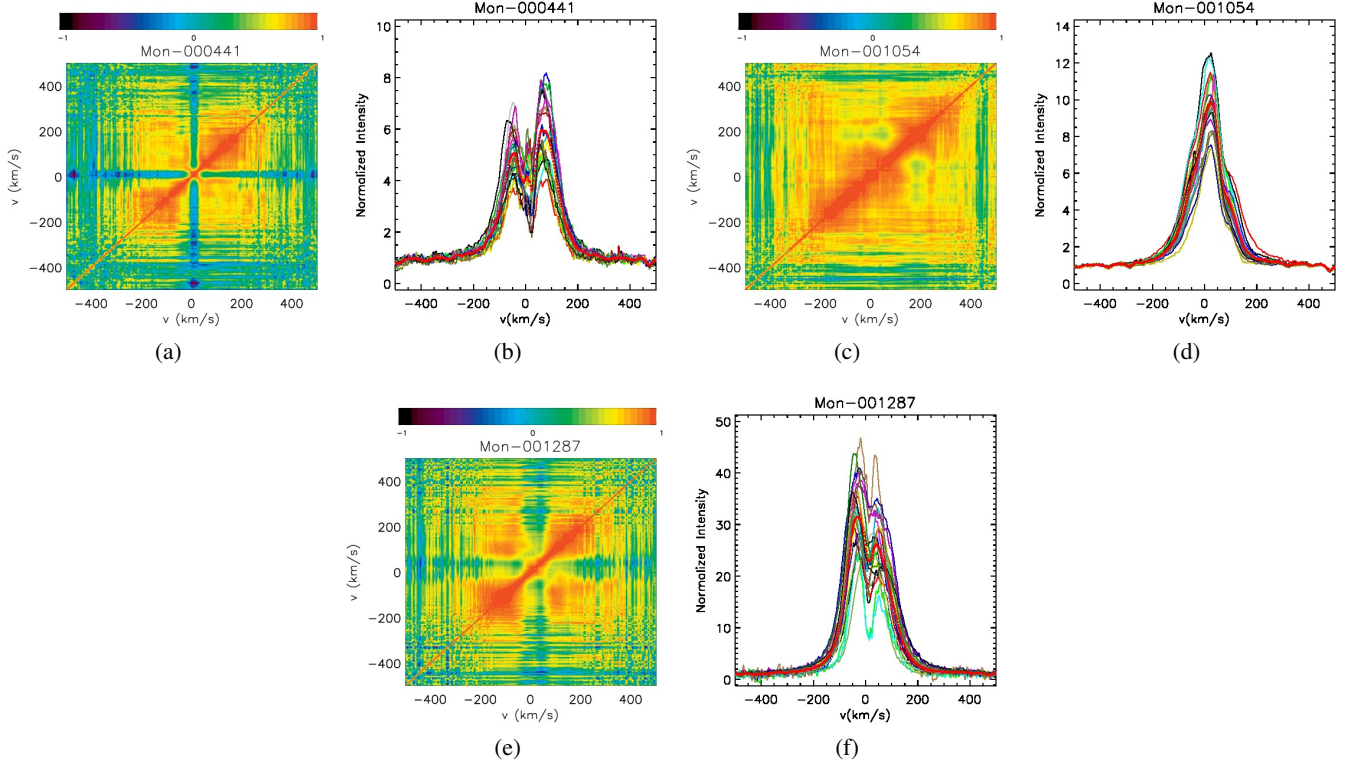


Fig. A.4. Same as Fig. A.2

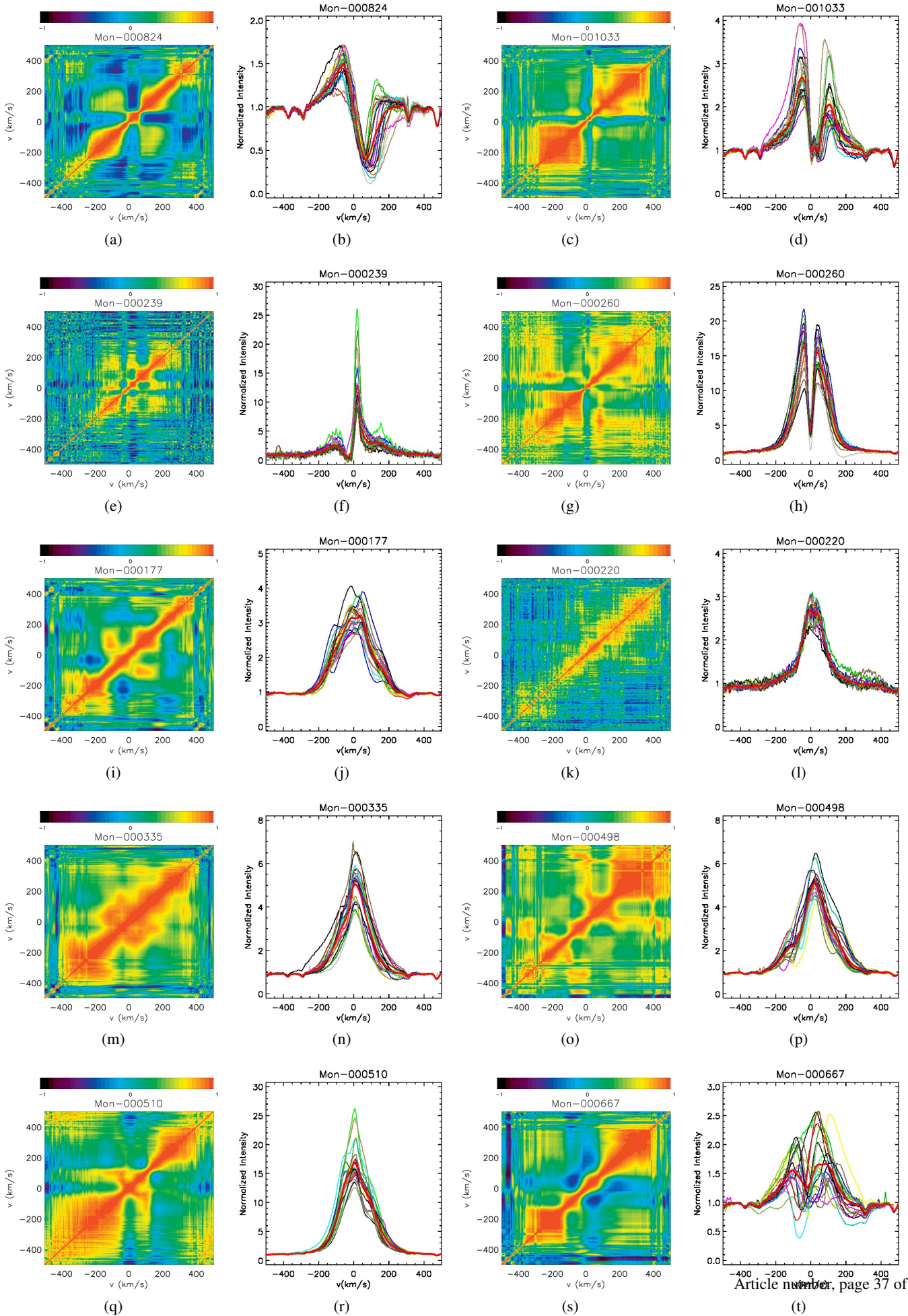


Fig. A.5. Same as Fig. A.1, but for stars that show no sign of correlation between the red and blue wings of the $H\alpha$ line profile. The narrow anticorrelation in the matrices of Mon-000824, Mon-000177, and Mon-000667 is due to the nebular contribution that was not entirely removed.

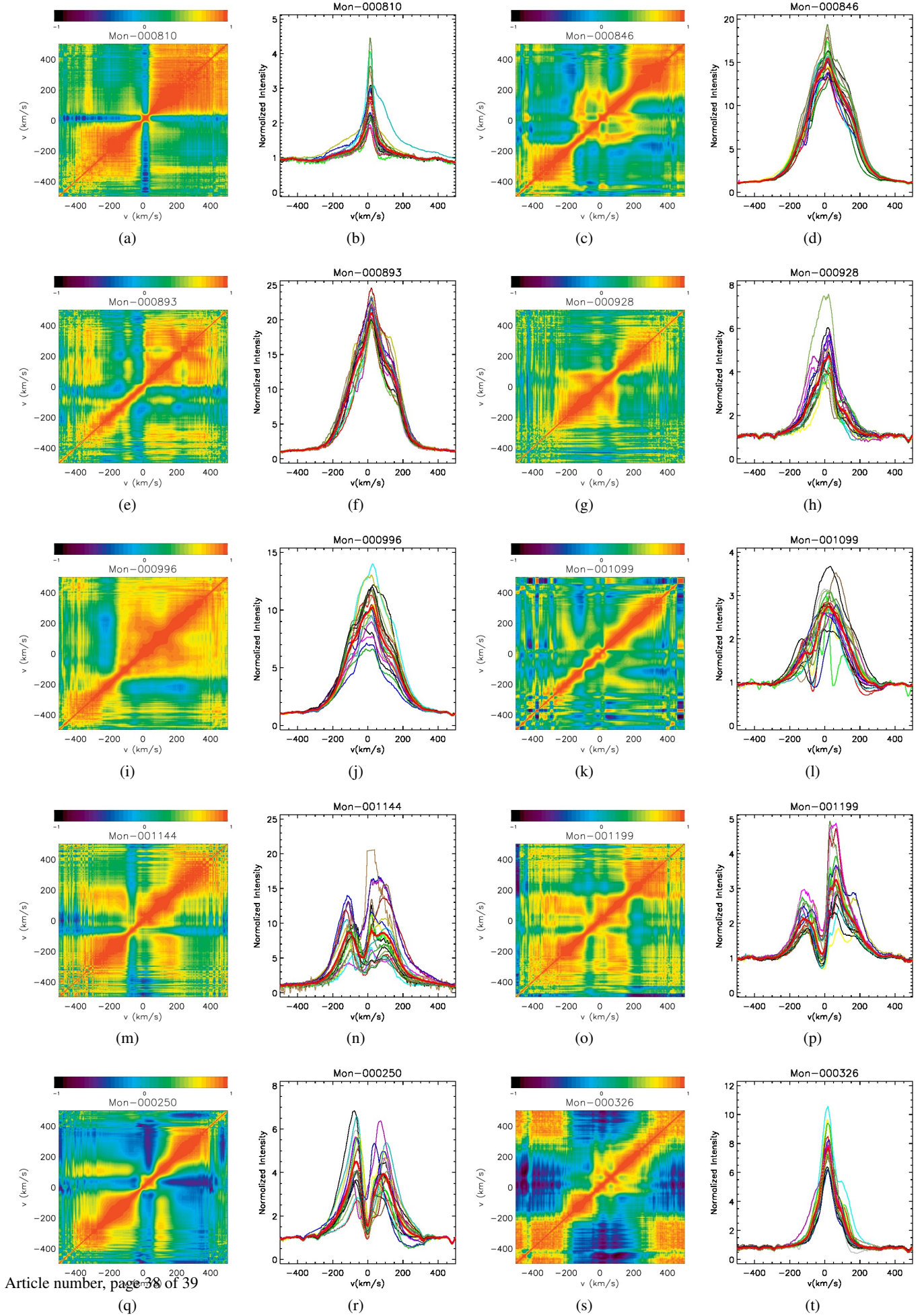


Fig. A.6. Same as Fig. A.5. The anticorrelation in the matrix of Mon-000250 is due to the nebular contribution that was not entirely removed.

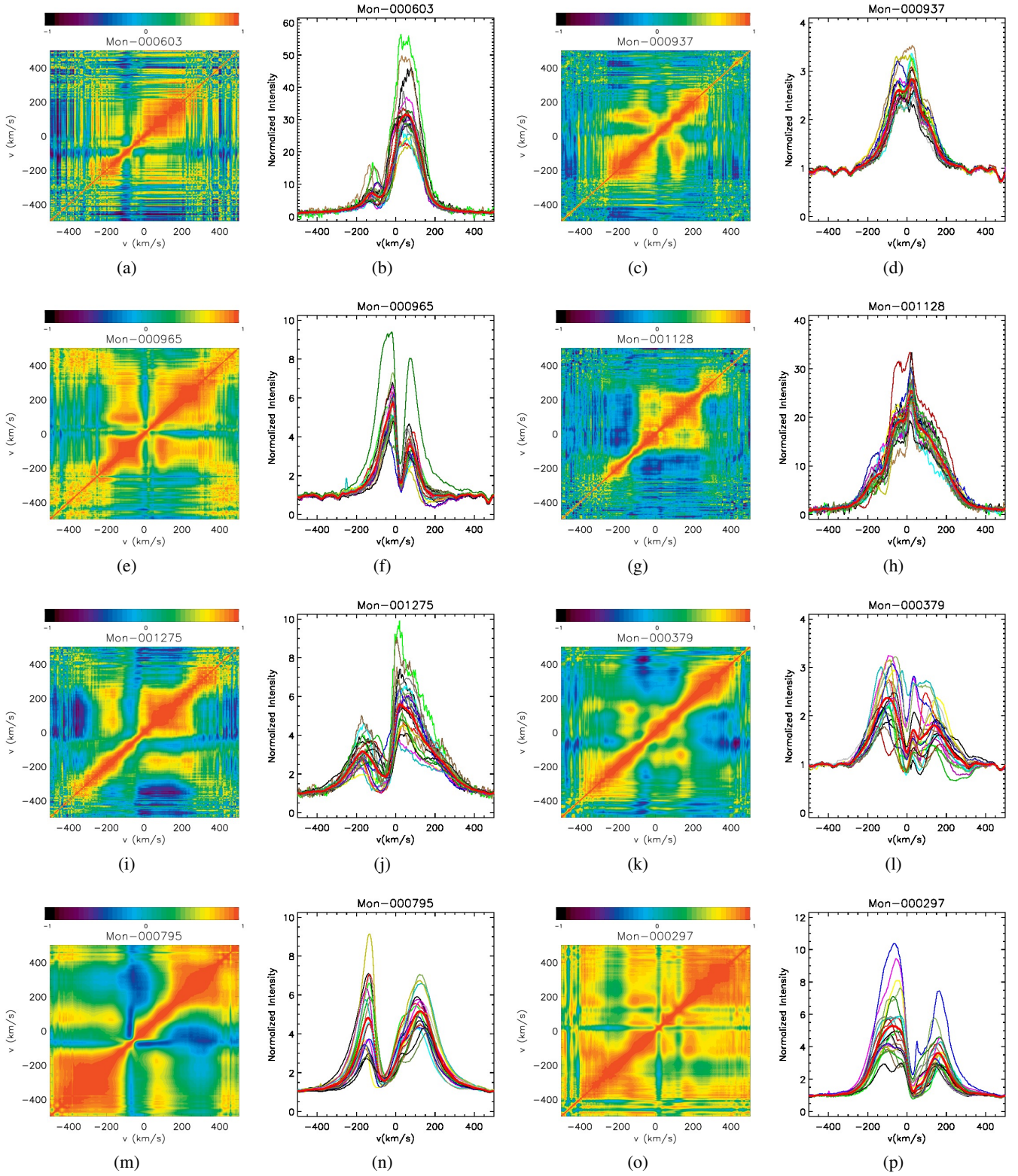


Fig. A.7. Same as Fig. A.5. The anticorrelation in the matrix of Mon-000795 is due to the nebular contribution that was not entirely removed.